INL/EXT-21-62416

Engineering-Scale Drying of Aluminum-Clad Spent Nuclear Fuel

June 2021

Experiment Report

J. Perry, R. Demuth, N. Cooper, and T. Knight
University of South Carolina

N. Parisi and G. Stafford
Holtec Government Services

A. W. Abboud and R. E. Smith, Editors
Idaho National Laboratory

INL is a U.S. Department of Energy National Laboratory operated by Batelle Energy Alliance, LLC

INL/EXT-21-62416

Engineering-Scale Drying of Aluminum-Clad Spent Nuclear Fuel

Experiment Report

J. Perry, R. Demuth, N. Cooper, and T. Knight
University of South Carolina
N. Parisi and G. Stafford
Holtec Government Services
A. W. Abboud and R. E. Smith, Editors
Idaho National Laboratory

June 2021

Idaho National Laboratory
ASNF Extended Dry Storage Project
Idaho Falls, Idaho 83415

http://www.inl.gov

Prepared for the
U.S. Department of Energy
Office of Environmental Management
Under DOE Idaho Operations Office
Contract DE-AC07-05ID14517

SUMMARY

Engineering-scale tests were performed to evaluate the relative effectiveness of forced gas and vacuum-drying processes on aluminum-clad spent nuclear fuel (ASNF) in preparation for extended dry storage. Drying models were developed to improve confidence in the likely range of conditions at the start of dry storage and to understand the factors most significant to each process. Testing was performed at the Holtec International Forced Helium Dehydration training facility in Camden, New Jersey, by students from the University of South Carolina in collaboration with Idaho National Laboratory.

A full-size Type 1a basket, with a full-diameter vessel configuration (based on the Department of Energy standardized canister design), was used in combination with a 10-assembly surrogate ASNF arrangement to provide a proxy for geometry. A resistance heater incorporated in one assembly simulated the influence of 100 W decay heat. This instrumented chamber allowed testing of the removal of bulk water, physisorbed water, and chemisorbed water over a range of operating parameters with either drying process.

Thick oxide films were grown on aluminum test plates to mimic the ASNF surface chemistry. These one-use test plates were housed within select assemblies during drying. Post-test analysis of these plates gave a measure of the moisture removed during each test, which was compared to a control.

Instrumentation provided detailed thermal, humidity, and gas or pressure data relevant to each test. Model simulations generally compared favorably to instrument data for the tests. While both processes were able to remove bulk water, removal of chemisorbed water was shown to depend heavily on local temperature. To the disadvantage of vacuum drying, operations approaching or exceeding 220°C achieved consistently more dehydroxylation.

Page intentionally left blank

ACKNOWLEDGMENTS

The authors wish to express their appreciation for the recommendations and assistance from Mike Connolly, Josh Jarrell, and Tim Yoder of Idaho National Laboratory; John Griffiths and Myron Kaczmarsky of the Holtec Government Services subsidiary of Holtec International; Jamil Khan, Tanvir Farouk, Yi Wang, Liam Peck, and Coleman Terrapin of the University of South Carolina; and Bob Sindelar and Anna d'Entremont of Savannah River National Laboratory, in the design and execution of this experiment. They also would like to acknowledge that funding for this work has been provided under the Department of Energy Idaho Operations Office, Contract DE-AC07-05ID14517 with Battelle Energy Alliance, LLC.

Page intentionally left blank

CONTENTS

FIGURES

TABLES

ACRONYMS

ASNF	aluminum-clad spent nuclear fuel
ATR	Advanced Test Reactor
CAD	computer-aided design
DOE	Department of Energy
FHD	forced helium dehydration
FLIR	forward looking infrared
IFSF	Irradiated Fuel Storage Facility
INL	Idaho National Laboratory
OES	optical emission spectroscopy
TGA	thermogravimetric analysis
RTD	resistance temperature detector
SEM	scanning electron microscopy
SRNL	Savannah River National Laboratory
UofSC	University of South Carolina

Page intentionally left blank

Engineering-Scale Drying of Aluminum-Clad Spent Nuclear Fuel

1. INTRODUCTION

As part of the Aluminum-Clad Spent Nuclear Fuel (ASNF) Extended Dry Storage Project, this engineering-scale drying experiment provides data from the drying of simulated materials at the scale of a single Type 1a basket in a one-third height Department of Energy (DOE) Standard Canister vessel.[1] The effort illustrates the benefits and limitations of drying processes within specific operating parameters in support of (sealed and vented) dry storage performance models. In conjunction with efforts to sample and analyze non-fuel material from stored ASNF and to assess radiolytic behaviors of oxyhydroxide corrosion on aluminum, this work substantiates the adequacy of preparation for the extended dry storage environment for ASNF.

To capitalize on previous investments while accounting for operation at engineering scale, forced helium dehydration (FHD) and initial vacuum-drying tests were planned and performed in collaboration with Holtec at their FHD training facility in Camden, New Jersey. The University of South Carolina (UofSC) designed and conducted the experiment and developed the drying process models. Holtec advised the project regarding industry practices and process parameters. Idaho National Laboratory (INL) provided the corrosion surrogate and coordinated the overall project.[2]

The use of the same vessel, basket, and geometry surrogate fuel load for all tests enables the comparison of FHD and vacuum-drying processes. Single-use corrosion surrogate plates provide a measure of process efficacy through the analysis of post-test residual moisture by comparison to a control. Process models, validated by test data, have also been developed to inform decision-making and to calibrate the range of residual moisture input parameters to the storage performance models.[3,4]

This report outlines the equipment used, summarizes the surrogate corrosion-development process, and presents the basis for the drying process models developed along with select simulations and corresponding test data. Drying test results and analyses are presented, along with observations regarding relative performance.

2. BACKGROUND

As ASNF is transferred from the reactor pool or underwater storage facility, some water remains with the fuel: bulk water (droplets and puddles unable to drain from horizontal surfaces or retained between plates due to surface tension and capillary effects), physisorbed water (molecular water adherent to solid surfaces), and chemisorbed water (waters of hydration integral to the morphology of the oxide surface layer). The bulk and physisorbed waters are present from simple water immersion whereas the chemisorbed water is from hydrated oxides formed on the ASNF cladding surface during the fuel exposure to water during reactor irradiation and post-discharge storage, or its “service history.” A drying process is used to limit the amount of this residual moisture introduced to the dry storage configuration. In practice, drying ASNF is expected to eliminate bulk water, but the removal of chemisorbed water would be incomplete.

2.1 Interrelated ASNF Extended Dry Storage Research

In addition to the concurrent efforts to model both sealed and unsealed dry storage conditions, several other tasks have been undertaken to support extended dry storage of ASNF under the direction of DOE Office of Environmental Management, Technology Development program. These activities are part of a broader action plan developed to address technical issues separately identified by both the DOE Spent Nuclear Fuel Working Group and the United States Nuclear Waste Technical Review Board.[5,6,7] Corrosion chemistry was examined for three of the aluminum alloys commonly associated with ASNF: AA 1100, AA 5052, and AA 6061-T6. This research considered oxide-film chemistry, vapor corrosion, and implications for drying ASNF at higher temperatures (250°C).[8,9]

Savannah River National Laboratory (SRNL) provided the template for (aqueous) growth of corrosion surrogate for test materials.[10,11,12] While corrosion behavior was observed to vary somewhat with alloy content, the morphology of the oxide layer (and associated chemisorbed moisture) is assumed to be of greater significance to the drying performance than the particulars of these aluminum alloys. Given the strong influence of environment on the resultant oxide morphology, a single alloy, AA 6061-T6, was selected to use for the surrogate test material for the drying experiment. Also, a recent Laboratory Directed Research and Development project sponsored by SRNL involving UofSC contributes complementary thermogravimetric analysis (TGA) scale drying test data.[13]

This study examined specimens collected from ASNF immediately following pool removal, as well as after a period of dry storage, to benchmark actual ASNF corrosion following irradiation and storage.[14,15,16,17] Analytical techniques employed for these ASNF specimens informed the strategy for examination of corrosion surrogate used in the drying experiments.

Also, work to assess the radiolytic gas generation associated with surface corrosion on aluminum (ASNF surrogate) supports the dry storage modeling effort and demonstrates dryness criteria suitable for sealed dry storage.[18,19,20] Radiolysis work found that drying coupons at 220°C for four hours leads to the production of little hydrogen compared to non-dried (control) coupons (in the absence of liquid water).[21] An instrumented lid has been developed to work with the DOE Standard Canister design to support an ASNF sealed dry storage demonstration. Lessons learned were shared from the demonstration canister and basket fabrication effort to inform production of the vessel configuration for drying.[22,23]

2.2 Principles of Drying

All drying processes rely on heat- and mass-transfer principles to motivate the migration of bulk and physisorbed water (via evaporation or boiling) and chemisorbed water (via decomposition) into the vapor phase for removal from the system. For a steady thermal flux, drying occurs at a constant rate across the surface of the bulk water. Constant-rate drying occurs until the surface area of the water-gas interface begins to contract. As this interface contracts, the drying rate progressively decreases; this is known as falling-rate drying.[24] Moisture removal becomes progressively slower as even the physisorbed water evaporates. Depending on the temperature and corrosion morphology, decomposition may allow the release of some of the chemisorbed water until further moisture removal becomes negligible (i.e., the drying rate approaches zero). The removal of moisture through the semiporous adherent corrosion layer is hindered (relative to oxyhydroxide powders of similar morphology) by the relative absence of mass transfer at the metal-oxide interface due to the nonporous nature of metal.

2.3 Design of Experiment and Adaptations

The INL/EXT-19-56017 report describes details of the ASNF engineering-scale drying experiment design.[25] These experiments employ mock ASNF assemblies in a Type 1a basket configuration to compare the performance of the FHD and vacuum-drying processes. One assembly has been fitted with a custom-designed resistance-heating element to simulate decay heat. Ten mock assemblies comprise a single full-size basket load within the one-third height drying vessel of full radial dimensions based on DOE Standard Canister specifications for Advanced Test Reactor (ATR) fuel loading. This configuration was modified to include the addition of a siphon tube to enable recirculation of hot gas for forced helium drying.

Mock ASNF assemblies (sometimes referred to as geometry surrogate fuel elements) were developed to simulate the approximate surface area, spacing between plates, and capacity for entrained water typical of ATR fuel. As illustrated in the series of photos in Figure 1, these assemblies are designed to allow convenient installation and removal of 12-inch plates (corrosion surrogate test plates having dimensions 12 inches by 3.15 inches by 0.05 inch) and to provide secure handling during loading and unloading operations between tests. The mock assembly structure exposes both sides of the surrogate plate except for a narrow region along each covered by the spacer. The bolted configuration also accommodates resistance heater components for simulation of decay heat.

In the Figure 1 unloading progression, only the full-length exterior plates are visible in the three assemblies in the image at the far left. However, the shorter (12-inch long) chemistry surrogate plates can be seen disassembled alongside the full-length exterior plates and both types of spacers in the center-left image. The thin full-length strip spacers maintain uniform gaps between the plates. The plate-width spacers, in conjunction with the chemistry surrogate plates, geometrically replace a single full-length plate within an assembly.

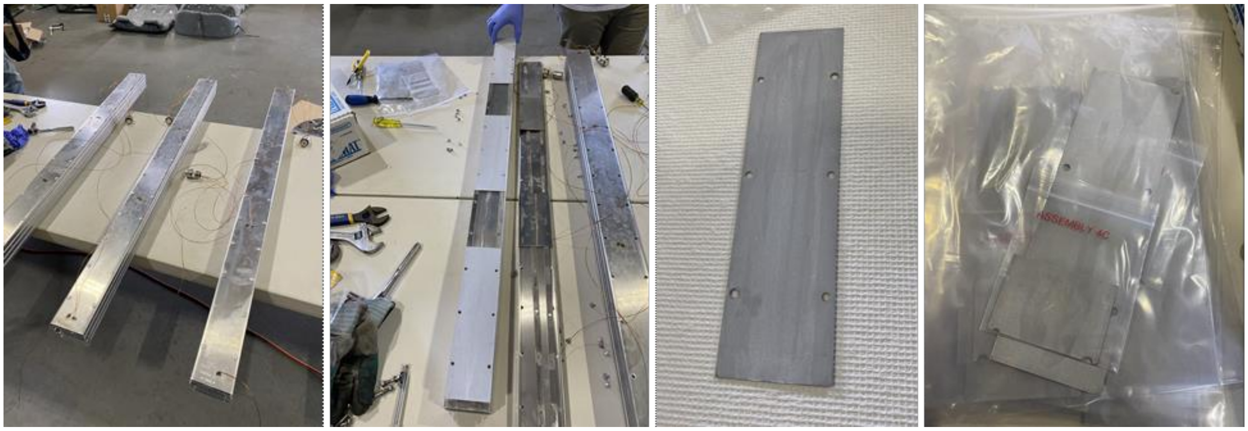

Figure 1. Post-test photo series showing mock ASNF disassembly handling and packaging of corrosion surrogate test plates before analysis.

Numerous ports and flanges were added to the drying vessel to accommodate feedthroughs for instrumentation and power for the experiment and data collection. Four viewports provide the option of thermal imaging in addition to receiving measurements from the many thermocouples available inside the chamber. Several thermocouples were initially wired incorrectly; some of those were abandoned in place because they were inaccessible without the risk of damage to the experiment due to the tight fit between the basket sleeve and vessel. Nonetheless, the original design for nearly four dozen thermocouples allowed enough redundancy for adequate thermocouple data.

In addition to real-time experimental temperature and moisture data to corroborate process modeling, post-test analysis of corrosion surrogate test plates provides objective evidence of efficacy with respect to residual chemisorbed water, an additional metric for comparison between FHD and vacuum drying.

3. Engineering-Scale Drying Equipment

Engineering-scale FHD and vacuum-drying tests were conducted using a custom-fabricated drying chamber that is shown in a series of photos in Figure 2. With an internal height of 64 inches and external diameter of 18 inches, the vessel was able to accommodate a 51-inch-tall Type 1a basket. The 12–13-inch gap from the top of the basket to the canister ceiling was not a concern in affecting drying because this amount of free space was typical at the top of standard DOE canisters. For this setup, the available space at the top allowed clearance for an assembly heater element, instrumentation, and gas-exchange connections through the 12 vacuum ports surrounding the chamber. Thermal imaging was permitted with four, 2.75-inch Conflat ports connected to 10-inch-diameter viewports that were spaced axially along the chamber with two on each side of the vent and siphon tube. The lid, vacuum ports, and viewports were all spaced out to ensure proper clearance for all bolted connections.[26,27]

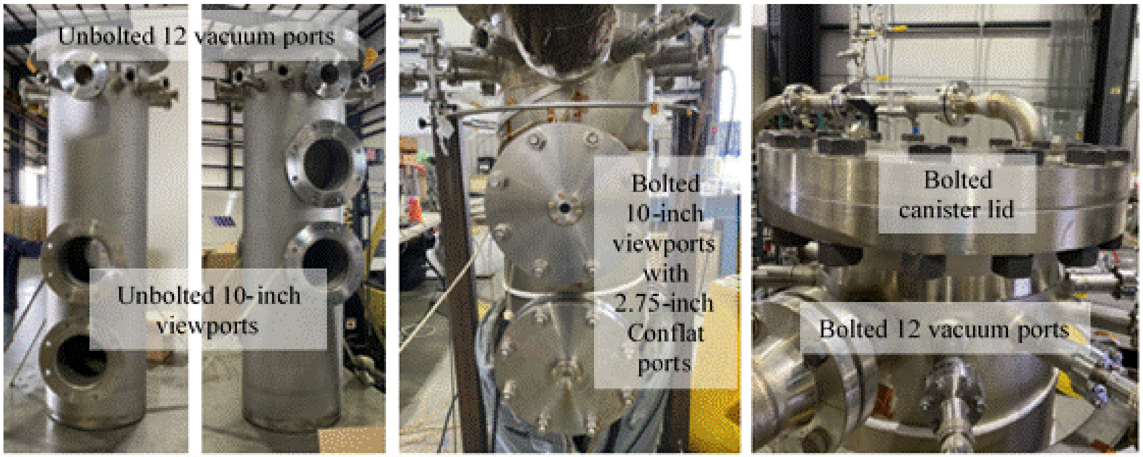

Figure 2. Drying chamber used to conduct FHD and vacuum-drying tests for the mock ASNF assemblies.

The traditional fuel storage basket has one or more 0.5-inch-diameter holes through the basket plates to allow for cross flow. These were not specified in the existing conceptual Type 1a basket design and were not used in the experiment design. The idea of baffling or alternating height of the different plates to better redistribute flow at the top of the chamber was also dropped because the plenum space in the chamber will be larger to accommodate necessary instrumentation and wiring for the experiments. The Type 1a basket housing the 10 mock ASNF assemblies was fabricated with a modified design to provide a false bottom when seated in the drying chamber. The 2.5-inch-tall void space beneath the main body of the basket, created by the false bottom, promoted an even distribution of the hot helium gas through a series of 1/4-inch holes within the baseplate. Traditionally in commercial fuel drying, a 3/4-inch outer-diameter siphon tube runs from the top of the canister, terminating 0.1 inch from the basket floor, through which hot gas is blown during FHD. However, the false bottom called for the siphon tube to be welded to the basket's base plate to ensure that 100% of the process flow entering the vessel through the siphon tube will be evenly distributed up through the basket to the vent. The fabricated Type 1a basket is shown in Figure 3. A braided hose crossed over the top end of the basket and connected the upper end of the siphon tube to the siphon port in the drying chamber wall (see Figure 4).

Figure 3. Type 1a basket and siphon tube without and with the basket's shell (left and center left), basket baseplate welded to its shell creating the false bottom (center right), and basket seated inside the drying chamber (right).

Figure 4. Type 1a basket housing the 10 mock ASNF assemblies positioned inside the drying chamber with the pipe connector extending over the basket to connect the siphon tube to its port.

Drying the 10 mock ASNF assemblies described in Section 2.3 required a capability to insert and remove the four assemblies containing corrosion surrogate plates before and after each experiment. The 12 vacuum ports (two of which were siphon and vent ports) extended out from the drying vessel to ensure the feedthroughs used for instrumentation did not protrude into the chamber cavity. Because two of the vacuum ports were used for the siphon and vent connection, and two more vacuum ports were used for relative humidity and pressure sensors, only eight thermocouple feedthroughs were available for the 35 thermocouples inside the vessel. Thermocouple feedthroughs rated for the expected chamber temperatures and pressures during FHD and vacuum drying were selected and incorporated into the chamber design, and each feedthrough accommodated wiring for five thermocouples. Initially, a crane was required to safely insert and remove three out of the four assemblies simultaneously. This prevented damage to the thermocouples and the wiring, as the thermocouple wires were interconnected between different feedthroughs. Later, ceramic thermocouple plugs were adopted to allow each of the four assemblies to be handled individually.

Decay heat was simulated through one assembly by looping nichrome wire between two custom boron nitride sheets in the middle of the assembly, as shown in Figure 5. The nichrome wire was able to achieve heat loads up to 100 W by connecting to a power feedthrough wired to a power supply. Heat was also applied during the drying experiments using five temperature-controlled heating tapes that were wrapped circumferentially and axially around the drying vessel. Capable of achieving canister surface temperatures as high as 300°C, the heating tapes in Figure 6 ensured a constant vessel-wall temperature during drying tests. Custom-fitted insulation was placed over the heating tapes and around the entirety of the chamber to limit heat loss. During forced gas drying, additional insulation was wrapped around the chamber-inlet piping and some of the outlet piping to limit the heat losses between the FHD system outlet and the inlet to the drying chamber. Insulation used during drying tests is displayed in a series of photos in Figure 7. The original design called for four heating tapes, but a large thermal gradient was observed between each strand of tape from the thermocouples of each heating tape controller. After adding a fifth heating tape and allowing the strands to be closer together, the five thermocouples for the five heating tape controllers were within 1°C of each other when testing at 260°C (maximum heating condition) under ambient internal vessel conditions, indicating a complete uniform chamber wall temperature was achieved. Although no assessment was made on the temperature of the lid and canister bottom during drying tests, there was a temperature drop of 20–30°C observed below the heating tape at the bottom of the cannister as well as above the heating tape at the top of the canister.

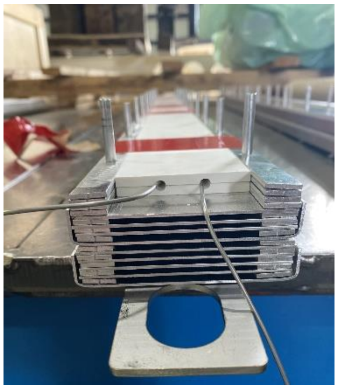

Figure 5. Mock ASNF assembly (Assembly 4) fitted with custom boron nitride plates and nichrome wire to simulate decay heat during drying tests.

Figure 6. Temperature-controlled heating tapes tightly wrapped around drying chamber wall.

Figure 7. Drying chamber covered only with chamber body insulation (left), drying chamber fully covered with custom insulation (middle), and FHD piping from the FHD skid to the inlet of drying chamber wrapped in insulation (right).

FHD and vacuum-drying tests were conducted through the use of Holtec's patented FHD and vacuum-drying systems. Holtec's FHD skid consists of an air-cooled condenser, moisture separator filter, blower, and preheater. It promotes the evaporation and removal of water by circulating hot helium gas through the vessel. The vacuum skid uses a condensate trap that is connected to a booster and vacuum-pump combo permitting moisture removal inside the chamber by means of evacuation. The booster pump (or roots blower) is consistently used in spent-fuel vacuum drying to increase the pumping speed at lower pressures. Typically, the booster pump is engaged around pressures of 10–20 Torr during commercial drying. Both drying systems were connected to the vessel using a valve manifold. This manifold also provided a capability of switching between the two skids with minimal configuration changes.

FHD Drying

Along with using Holtec's drying systems, the experimental drying tests were conducted following an adaptation of Holtec's drying procedures. Holtec's procedure is to blow or inject gas through the siphon tube rather than evacuate through the siphon and vent ports as is typical with vacuum drying. Therefore, FHD was operated with hot helium entering the chamber through the siphon tube, where it is directed to the false-bottom space. The helium gas then flows up through the fuel assembly cells and after collecting moisture, exits the vessel through the vent port.

The FHD process normally operates in two phases. During Phase 1 drying, bulk water that resides in the canister first evaporates and then boils as the local temperature rises. As the gas stream is circulated through the canister, it eventually becomes saturated with water vapor. The heat from the helium gas is transferred to the water molecules in the canister, accelerating the transition from liquid to vapor state. The vapor mixes with the circulating gas steam, and finally exits with the gas discharged from the canister.

The canister exhaust enters the FHD skid and immediately passes through an air-cooled condenser, which quickly lowers the gas temperature to about 100–120°F. The excess water vapor in the gas stream condenses back to liquid, allowing the downstream moisture separator filter to strip liquid water from the stream. All the liquid moisture will be removed from the canister as long as the temperature in the canister is higher than the temperature at the air-cooled condenser outlet. However, the temperature at the condenser outlet limits the minimum moisture level that can be achieved during Phase 1. During normal spent fuel drying operations, Phase 2 operations are performed where the gas temperature is lowered further using a demoisturizing system enabling more moisture to be stripped from the circulating gas. Engaging Phase 2 operations too early can cause the vapor to freeze, creating blockages in the FHD system and preventing gas circulation. Hence the two-phase drying approach.

The moisture in the canister exhaust is approaching or at saturation during Phase 1 drying, while liquid water in the canister is steadily removed (constant-rate drying). During Phase 1 drying, the air-cooled condenser steadily removes liquid water from the exhaust but leaves some moisture in the helium stream circulating through the system. Progressing to Phase 2 drying, the temperature of the gas stream exiting the demoisturizing system is progressively reduced to further limit the low levels of remaining moisture. The chiller is used, initiating Phase 2, when the air-cooled condenser is removing diminishing amounts of liquid water from the canister exhaust. Under these conditions, only a limited amount of moisture remains in the system, preventing the tubes of the Phase 2 heat exchanger from clogging up from ice blockages. During Phase 2 drying, the heater and air-cooled condenser remain energized. The flow of preheated helium to the canister is sustained to maintain the thermal inertia inside until backfill concludes the preparation for sealed storage.

Phase 2 was not used during these FHD tests for several reasons. There was no intention of backfilling or sealing the canister after drying: all test samples were to be handled in air after the test conclusion, so Phase 2 removal of moisture from the helium would have been inefficient. Operating temperatures and durations at temperature were integral to the experiment design, with the objective of assessing process efficacy within specific constraints identified for ASNF. Furthermore, the drying endpoint, regardless of process, had been defined by an absence of liquid water for dry storage in existing facilities and was thereby adopted for an equitable process-to-process comparison. For FHD tests, the process endpoint was confirmed when water no longer collected in the FHD skid. Visual observations of canister internals and surrogate ASNF following each test provided the final confirmation of the absence of liquid water.

Vacuum Drying

Experimental vacuum-drying tests were conducted following the typical vacuum-drying process used for commercial spent nuclear fuel: the canister pressure was reduced over a series of predetermined hold points, culminating in a final pressure below 3 Torr. At each hold point, the canister was isolated from the vacuum skid to monitor the pressure rise inside the canister. The typical vacuum-drying process is concluded once the final pressure hold remains below 3 Torr for 30 minutes (conditions not sustained in the presence of excess liquid water).

Vacuum Drying at IFSF Drying Process Conditions

An additional vacuum-drying process was conducted using the Irradiated Fuel Storage Facility (IFSF) heated-container drying process. This operation is used at IFSF prior to the placement of ASNF in non-sealed (vented) dry storage. After loading drip-dried ASNF, the IFSF sets an insert placed inside the canister to 140°C. IFSF choose this insert temperature set point to ensure the ASNF does not exceed 100°C. Due to design limitations, the chamber wall heating tapes were set to 140°C to stand in for the insert used in the IFSF vacuum-drying process. Otherwise, these vacuum tests tried to match IFSF operating practices. The insert is preheated for 30 minutes at atmospheric pressures. Following the preheat, IFSF begins the drying operation by initiating an air purge at the same time the vacuum pump is turned on. This process allows the canister pressure to be maintained in the 10–90 Torr range, with a recommended drying pressure of 50 Torr. The IFSF operates the purging-air supply at 2.5 scfm at a minimum supply pressure of 80 psig to sufficiently dilute the vapor generated from the heated insert. A cycle of pressurization rates begins after the 50 Torr drying pressure is achieved. This cycle consists of the canister being isolated from the air supply and vacuum pump every 15–30 minutes to record a pressurization rate for 3–10 minutes. After a minimum of 3 hours of drying following preheating, the test is concluded if the change in two consecutive slopes calculated from the three most recent pressurization rate measurements are negative (indicating a decline in residual water evaporation rate) or if two consecutive pressurization rate measurements are <1 Torr/hr.[28]

4. CULTIVATION OF SURROGATE CORROSION FILMS

For simplicity, surrogate test material for drying was limited to aluminum alloy 6061-T6 plates: 12 inches by 3.15 inches by 0.050 inch, with bolt holes to enable their incorporation into the mock ASNF assembly design. These provide an analog to ATR fuel, with corrosion morphology that can be reasonably extrapolated for application to other aluminum alloys relevant to the ASNF inventory. This test material requires significant preparation lead time: delivery from the vendor requires about 6 weeks from order placement. INL staff resurfaces each plate and takes measurements before immersion. Plates remain in water for a nominal 6 weeks to grow a thick layer of hydrated oxide, and plates are measured and examined before shipment to Holtec and UofSC for testing.

Small-scale studies at INL (using 1 inch by 2 inch, AA 6061-T6 coupons) confirmed the stability of the oxide morphology after brief air-drying to allow for post-immersion mass measurement. Coupons remained stable regardless of storage environment in open air, in a (dry) sealed specimen bag, or in a specimen bag sealed with a small amount of liquid water added. While corrosion growth does continue with extended immersion time, small to moderate variations in immersion duration are unlikely to influence test results as an indication of drying efficacy relative to control, and no measurable decomposition occurs at room temperature over a period of up to 6 weeks.

The surrogate corrosion-growth protocol was developed in cooperation with SRNL. The procedure for handling the 12-inch test plates required applying a 600-grit finish (using a hand-held orbital sander to approach 21.7 µinch surface roughness for the small coupons). Plates were resurfaced and degreased with a rinse sequence of acetone, alcohol, and nano-pure water. Each plate was then air dried, measured, and weighed before immersion in low conductivity (~2 µS/cm) nano-pure water. Plates were sanded in small sets or individually so that they could be immersed promptly thereafter (within an hour of sanding). Oxide layers, typically 3–10 µm thick and predominantly bayerite, form over the immersion period. The immersion vessels only fluctuated with ambient indoor laboratory temperature (nominally 20°C), with nano-pure water added as needed (approximately weekly) to maintain immersion volume and keep all the plates fully submerged throughout.

Surrogate corrosion is an integral part of the strategy for assessment of drying processes and process viability. SRNL Laboratory Directed Research and Development results showed cracking and spalling of the bayerite layer with drying, particularly at higher temperatures.[29] Observed spallation results in loss of material, confounding tracking gross behavior by mass change, but (based on experience upon brushing to remove loose particles) it does not appear to significantly alter surface analyses.

Corroded surrogate plates have been produced and delivered in batches. Given the suspension mechanism used, the full capacity of the immersion vessels provided 45 plates per batch. One of the vessels is shown along with a batch of plates as suspended in Figure 8. Spacing between plates is maintained during immersion and in transport with nylon rods secured through a couple of the bolt holes to create a stack with uniform gaps. Three vessels are available to support overlapping immersion schedules, as indicated in Table 1. Scanning electron microscopy (SEM) images of surfaces and cross sections were taken on batch samples retained at INL to verify consistent batch-to-batch surface film growth before shipment.

Figure 8. A batch of surrogate test plates immersed in water for corrosion growth (left) and side view of plates as spaced on nylon rods (right).

The design concept was to use 12 plates within the ASNF assemblies (in the Type 1a basket load) for each test run. However, after a few successful FHD tests, the consensus was that the full range of performance could be observed from more limited use of the corroded plates. Testing proceeded using seven of the corroded plates per test to conserve test material, allowing for a larger test matrix to resolve vacuum-drying procedural issues and provide additional data for model development and validation. The five omitted corroded plates were replaced with uncorroded aluminum plates having the same 12-inch geometry to maintain the aluminum surface area of the assemblies. Regardless of the number of plates implemented for each drying test, one corroded plate from each batch was sectioned and examined at INL prior to shipment of the batch, and three corroded plates from each batch of 45 plates were untested and served as control plates for thermogravimetric analysis.

Corroded surrogate plates used for drying tests were labeled based on assembly identification. As illustrated in Figure 9, each of the 10 assemblies was labeled depending on its placement inside the basket. Assemblies 1, 4, 7, and 10 housed three corroded plates each for drying tests using 12 corroded plates. These were spaced axially near the exterior of the assembly to provide a wide range of drying conditions for the plates. Each corroded plate was further classified as A, B, or C to signify the plate’s axial location, with A being the bottom of the assembly and C, the top. Only assembly slots 1A, 1B, 1C, 4B, 4C, 7A, and 10A were filled with a corroded plate for drying tests using only seven corroded plates. These slots were thoughtfully chosen as they provided the full range of conditions experienced by the original 12 corroded plates**.**

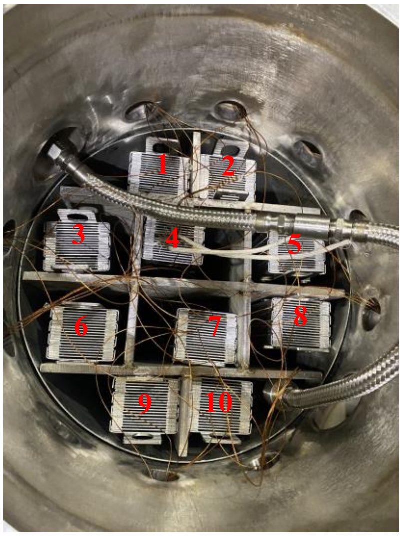

Figure 9. Assembly locations identified within the drying load.

Table 1. Schedule of immersion batches for surrogate corrosion test plates.

Identity	Total # Plates	Date of Immersion	Date of Removal	Duration of Immersion (in days)	# to Holtec	# to UofSC	# Retained at INL
Batch 1	45	3/12/2020	6/23/2020	103	42	2	1
Batch 2	45	6/30/2020	8/10/2020	41	42	2	1
Batch 3	45	7/21/2020	9/14/2020	55	42	2	1
Batch 4	45	8/13/2020	10/7/2020	55	42	2	1
Batch 5–Part 1	15	8/20/2020	11/9/2020	81	14	0	1
Batch 5–Part 2	30	8/20/2020	—	>220	—	—	—
Batch 6	21	11/18/2020	—	>130	—	—	—

The original intent was to supply consistently corroded plates at 2-week intervals. The evolving Covid-19 pandemic, and some minor adaptations to accommodate thermocouple installation and overall thermal-performance issues, resulted in multiple disruptions to the planned schedule. However, by using the reduced number of corroded plates per test, a consistent supply of initial test materials was maintained to support the engineering-scale test operation.

5. METHODS

This work uses two primary techniques to evaluate the effect of drying on the corrosion surrogates' surface oxide layer: TGA and SEM. TGA is used to benchmark the nominal potential (for each batch) of corrosion surrogate to lose mass during drying, based on undried control samples, and then evaluates the relative success of each experimental sample against the control average for its batch of origin. SEM imaging qualitatively corroborates the crystal microstructure of (areas presumed representative of) the surface corrosion before and after drying and TGA.

5.1 Thermogravimetric Analysis

TGA is an analytical technique used to monitor the weight change that occurs as a sample is heated at a constant rate. The mass change could occur due to phase change or chemical reaction: in this experiment, primarily decomposition, evaporation, or oxidation. For this TGA evaluation, Netzsch's STA 409 CD (Figure 10) with the small furnace attachment was used in conjunction with a Type B thermocouple. The focus of this evaluation is decomposition via dehydroxylation, and the TGA measured the mass loss occurring in oxidized aluminum control samples for comparison to the same measured value of post-dried samples (prepared from test materials processed via engineering-scale FHD or vacuum drying). This provides a quantitative comparison between the two drying processes as well as among variations in duration or other process parameters.

Figure 10. Netsch's STA 409 CD.

Due to the nature of the TGA tests, measuring such small masses in a closed system, the buoyancy effect can be significant. The buoyant forces of the chamber's internal atmosphere change in relation to the temperature. As the temperature of the furnace increases, the density of the gases inside the chamber decreases, causing the buoyant forces to decrease. These buoyant forces cause fluctuations to the TGA measurements throughout the heating and cooling periods, independent of observed mass changes, convoluting interpretation of results. The buoyancy effect can be controlled by regulating the atmosphere of the chamber. The STA 409 CD uses a gas-flow controller to pump argon gas into the chamber at a consistent rate, making the buoyancy effect consistent throughout each test. The reproducibility of the buoyancy effect enabled the use of a blank run to create a correction file to account for the mass change in the flowing gas. In this evaluation, the buoyancy effect was minimal because the final mass loss value was measured after the gas has cooled down inside the chamber. However, once generated, the correction file was employed to facilitate direct interpretation of the TGA curves.

5.2 Scanning Electron Microscopy

SEM determined the surface structure of the samples before and after various drying methods. The microscope used for all images was the Tescan Vega3 SEM in UofSC's Electron Microscopy Center. Because the purpose was to image the oxide layer of the sample, charging was constantly encountered. Any nonconductive material, such as an oxide, may be subject to the buildup of electrons during SEM examination. This occurs when the material absorbs electrons without backscattering or allowing them to pass through to the sample holder. Charging results in bright white spots, streaks, and various other artifacts that affect image quality. There are various methods to reduce charging that include reducing the voltage, magnification, or beam intensity, but those all have a direct effect on the quality of the image. The easiest way to reduce charging without decreasing image quality is by adding a piece of copper tape to connect the surface of the sample to the sample holder. This grounds the sample and allows a greater flow of electrons off the surface of the sample. In many cases, the copper tape was not sufficient to prevent charging at high magnifications, so gold sputter-coating was implemented. Gold sputter-coating involves dispersing Au atoms across the surface of the sample, making it semiconductive and resistant to charging.

5.3 Sample Preparation

Samples arrived at UofSC in plastic bags directly from Holtec (Figure 11), where the samples were dried either by FHD or vacuum drying. The samples were then cut to sizes that would fit in the TGA crucible, typically around 14 mm by 15 mm (Figure 12). The samples were cut using a Leco VC-50 diamond wafering saw (Figure 13). This saw was selected due to its dry-cutting capabilities, meaning that no water or oil on the saw would affect the corrosion layer of the sample. However, accumulated cutting dust gives a slight discolored appearance along the cuts in Figure 12. The samples were cut at a very low speed so as to avoid heating the sample. The edges of the samples were then cleaned with a pair of tweezers to remove loose material left by the cutting process. Once cut, the dimensions of the sample were immediately measured using a digital caliper. The four sides of the sample were measured (near the corners), and the oxide surface area (neglecting oxide thickness) was calculated as twice the product of the average length and average width of the sample (420 mm^2 for the nominal 14 mm by 15 mm dimensions).

The TGA crucible was weighed with and without the sample, both before and after the TGA run, using a digital scale. The sample was placed in the crucible and weighed to prevent any loose powder from affecting the net mass loss at the end of the process. The TGA crucible containing the sample was placed inside the TGA chamber, where TGA operation began. To minimize sample exposure to ambient moisture, the sample bags remained sealed until immediately before sizing for analysis.

SEM sample preparation began with the same sizing method described above. The edges were cleaned with tweezers to remove loose material that could damage the SEM. Once cut, the samples were placed on a sample holder using a carbon-black sticker. The sample was then grounded with a piece of copper tape, as shown in Figure 14, and gold sputter-coated using a Denton sputter coater. The number of gold coats used was dependent on the thickness of the oxide layer for the sample and the amount of charging that occurred during the imaging process. The Denton sputter coater used requires multiple runs to achieve a consistent coat. Each run applies an approximately 5-nm-thick coat, but due to the rough surface of the samples, the coating was less than that. An approximately 25-nm coat was applied to samples in most cases in order to mitigate the effects of charging.

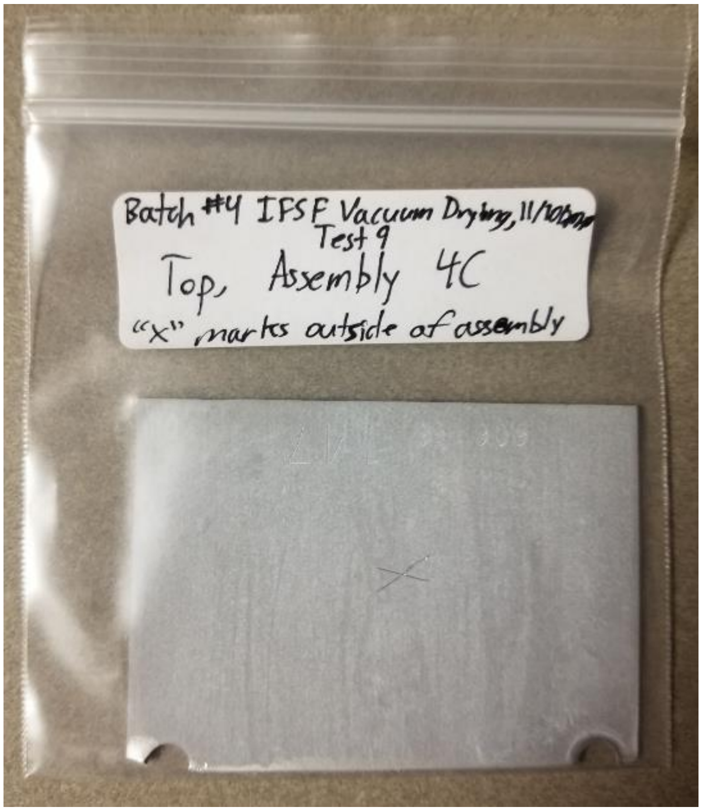

Figure 11. Sample storage.

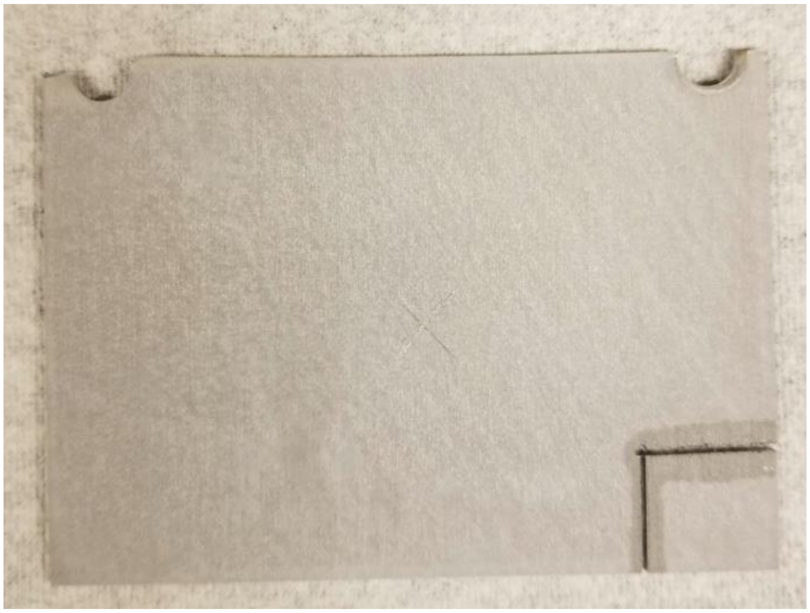

Figure 12. Sample cut approximately 14 mm × 15 mm.

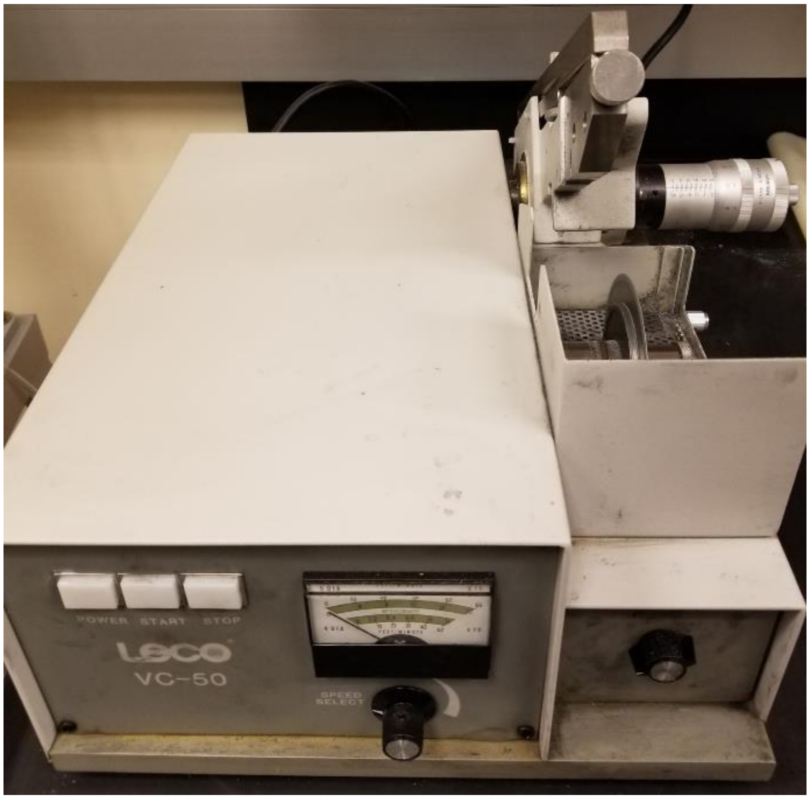

Figure 13. Leco VC-50 diamond wafering saw.

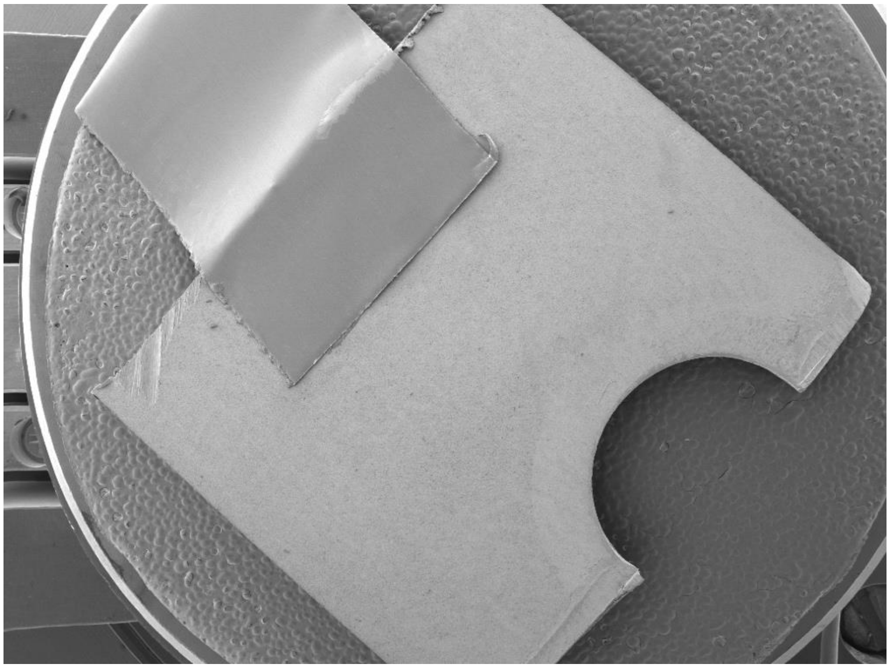

Figure 14. Prepared SEM sample on sample holder with copper tape.

5.4 TGA Operation

After the sample was prepared and loaded into the TGA chamber (Figure 15), the chamber was sealed using a vacuum pump and brought to low vacuum using a turbomolecular pump. The chamber was then backfilled with high-purity argon gas, which continuously flowed through the chamber for the duration of the test. A file was then created for the sample with standard TGA parameters. The standard parameters used in tests were heating the sample to 600°C at a rate of 5°C per minute, holding at 600°C for 6 hours, cooling the sample to 20°C at a rate of 20°C per minute, then holding at 20°C for 2 hours. Note that the final 2-hour hold was necessary to allow the TGA to record measurements throughout the cooling process. In later tests, a correction file was used to account for the buoyancy effect in the TGA graphs. The correction file was created by doing a test with an empty crucible under the standard parameters. This correction file would then be loaded and used to create a data file for the sample, which would subtract the buoyancy effect of the gas from the resulting data. The use of the correction file does not affect the final value for mass loss but does result in a more readable graph of the TGA. After the experiment, the crucible was unloaded from the TGA chamber. While the TGA curve does provide a final mass loss, the sample was weighed separately to ensure more consistent results. The final mass loss in the TGA curve was consistent with the change in weights measured with the digital scale; however, occasional gas-flow fluctuations would affect the reading of the mass loss value on the TGA curve. The difference between the initial and final weights of the crucible and sample, as measured with the digital scale, was recorded as the mass loss for that sample.

Figure 15. Prepared sample in TGA crucible on TGA thermocouple.

5.5 SEM Procedure

SEM operation began with loading the prepared sample into the SEM chamber and vacuuming the chamber to a high vacuum. The SEM operates under high vacuum to prevent chamber atmosphere from affecting the electrons as they are emitted from the filament. Once under high vacuum, the microscope parameters were set—specifically, the beam intensity, working distance, and high voltage. A beam intensity of 10 (manufacturer's recommendation) was used for all images, as well as a high voltage of 20 kV and a working distance between 5–10 mm. Once parameters are set, HV is turned on starting the flow of electrons. The rest of the process includes navigating the surface of the sample, zooming in to the desired magnification, and focusing the image appropriately. Once the sample is focused, the image can be captured using the microscope's acquire function.

6. DRYING PROCESS OPERATIONS

Engineering-scale drying experiments at Holtec consisted of 10 FHD tests and 12 vacuum-drying tests performed to evaluate their effectiveness in removing bulk and chemisorbed water. Test parameters for the FHD and vacuum drying are summarized in Table 2 and Table 3, respectively. The "Length of Test" in the table is measured from the activation of a specific component (blower and/or heater for FHD and vacuum for vacuum drying) until the end of the test. For FHD, the test duration begins with the initiation of the blower and/or FHD heater module. The FHD test duration concludes after the targeted duration at temperature is met. FHD tests were conducted with varying drying times at a target temperature of 220°C for the chemically treated plates. FHD test 1 was the only test that did not achieve the targeted temperature as discussed later in this section. Test 1 was concluded after the total test time exceeded 8 hours. Vacuum-drying tests were conducted with varying durations of isolation holds and varying chamber wall temperatures. Isolation holds consisted of isolating (valving off) the chamber from the vacuum pump at different vacuum levels to monitor the pressure rise. Each hold had pressure criteria that needed to be met before continuing to the next vacuum hold. The isolation holds and criteria used in the experimental vacuum-drying tests are shown in Table 4. The evaluation of vacuum tests considered not only the removal of liquid water and water vapor but also whether the formation of ice was avoided. Among the 12 vacuum experiments, eight followed an isolation-hold process consistent with Holtec's vacuum-drying process, and four followed the IFSF drying process to further evaluate the efficacy of drying through vacuum.

Table 2. FHD test summary.

FHD Drying Test Number	Type of Test	Length of Test (minutes)	Number and Locations of Treated Plates	Maximum Inlet and Outlet Gas Temperature (°C)	Power Set Point for Assembly Heater (W)	Heating Tapes Set Points During FHD (°C)
1	8 hours at 220°C, 105 mL water per assembly	496.5 minutes (from blower & heating on)	12 (1A, 1B, 1C, 4A, 4B, 4C, 7A, 7B, 7C, 10A, 10B, 10C)	Inlet = 188.8°C	Not in use	Not in use
				Outlet = 122.8°C		
2	8 hours at 220°C, 105 mL water per assembly	774 minutes (from blower & heating on)	12 (1A, 1B, 1C, 4A, 4B, 4C, 7A, 7B, 7C, 10A, 10B, 10C)	Inlet = 238.1°C	100 W	Inlet pipe = 315.5°C (600°F) Max. achieved temp = 528°F
				Outlet = 219.4°C		Vessel wall = 260°C (500°F)
3	12 hours at 220°C, 105 mL water per assembly	1100 minutes (from blower & heating on)	12 (1A, 1B, 1C, 4A, 4B, 4C, 7A, 7B, 7C, 10A, 10B, 10C)	Inlet = 239.1°C	100 W	Inlet pipe = 315.5°C (600°F) Max. achieved temp = 532°F
				Outlet = 222.7°C		Vessel wall = 260°C (500°F)
4	8 hours at 220°C, 52.5 mL water per assembly	837.4 minutes (from heating on)	7 (1A, 1B, 1C, 4B, 4C, 7A, 10A)	Inlet = 237.5°C	100 W	Inlet pipe = 315.5°C (600°F) Max. achieved temp = 535°F
		873.4 minutes (from blower on)		Outlet = 222.7°C		Vessel wall = 260°C (500°F)
5	12 hours at 220°C, 105 mL water per assembly	1096.1 minutes (from heating on)	7 (1A, 1B, 1C, 4B, 4C, 7A, 10A)	Inlet = 238.8°C	100 W	Inlet pipe = 315.5°C (600°F) Max. achieved temp = 537°F
		1140.2 minutes (from blower on)		Outlet = 222°C		Vessel wall = 260°C (500°F)
6	6 hours at 220°C, 105 mL water per assembly	652.4 minutes (from heating on)	7 (1A, 1B, 1C, 4B, 4C, 7A, 10A)	Inlet = 235.7°C	100 W	Inlet pipe = 315.5°C (600°F) Max. achieved temp = 538°F
		701.9 minutes (from heating on)		Outlet = 228.7°C		Vessel wall = 260°C (500°F)
7	8 hours at 220°C, 105 mL water per assembly	625.7 minutes (from blower on)	7 (1A, 1B, 1C, 4B, 4C, 7A, 10A)	Inlet = 238.3°C	100 W	Inlet pipe = 315.5°C (600°F) Max. achieved temp = 535°F
		665.3 minutes (from heating on)		Outlet = 226.9°C		Vessel wall = 260°C (500°F)
8	12 hours at 220°C, 105 mL water per assembly	854.56 minutes (from heating on)	7 (1A, 1B, 1C, 4B, 4C, 7A, 10A)	Inlet = 239.2°C	100 W	Inlet pipe = 315.5°C (600°F) Max. achieved temp = 535°F

		945.5 minutes (from blower on)		Outlet = 227.8°C		Vessel wall = 260°C (500°F)
9	8 hours at 220°C, 105 mL water per assembly, lower heating tape setpoint	652.6 minutes (from heating on)	7 (1A, 1B, 1C, 4B, 4C, 7A, 10A)	Inlet = 241.0°C	100 W	Inlet pipe = 315.5°C (600°F) Max. achieved temp = 525°F
		689.5 minutes (from blower on)		Outlet = 206.7°C		Vessel wall = 75°C (167°F)
10	8 hours at 220°C, 105 mL water per assembly, lower inlet gas 220°C, lower heating tape setpoint	669.36 minutes (from heating on)	12 (1A, 1B, 1C, 4A, 4B, 4C, 7A, 7B, 7C, 10A, 10B, 10C)	Inlet = 221.2°C, but maintained an inlet gas temperature of 220°C for test	100 W	Inlet pipe = 220°C (428°F) Max. achieved temp = 428°F
		707.7 minutes (from blower on)		Outlet = 185.0°C		Vessel wall = 75°C (167°F)

Table 3. Vacuum-drying test summary.

Vacuum Drying Test Number	Type of Test	Length of Test (minutes)	Number and Locations of Treated Plates	Spacer Disc or Bulk Water Tray Element Used?	Power Set Point for Assembly Heater (W)	Heating Tapes Set Points During Vacuum Drying (°C)
1	5-minute holds, 150°C vessel heat tape setpoint, 105 mL water per assembly	253.16 minutes (from vacuum on)	7 (1A, 1B, 1C, 4B, 4C, 7A, 10A)	Spacer disc, 28 mL of water added	100 W	Vessel wall = 150°C (302°F)
2	5-minute holds, preheated to 30–35°C, 150°C vessel heat tape setpoint, 105 mL water per assembly	438.46 minutes (from preheating)	7 (1A, 1B, 1C, 4B, 4C, 7A, 10A)	Spacer disc, 28 mL of water added	100 W	Vessel wall = 150°C (302°F)
		262.86 minutes (from vacuum on)				
3	15-minute holds w/ normal 30 minute <2 Torr hold, preheated to 30–35°C, 150°C vessel heat tape setpoint, 105 mL water per assembly	631.1 minutes (from preheating)	7 (1A, 1B, 1C, 4B, 4C, 7A, 10A)	Spacer disc, 28 mL of water added	100 W	Vessel wall = 150°C (302°F)
		435.56 minutes (from vacuum on)				
4	15-minute holds w/ normal	492.46 minutes (from preheating)	7		100 W	Vessel wall = 150°C (302°F)

	30 minute <2 Torr hold, preheated to 30–35°C, 150°C vessel heat tape setpoint, 105 mL water per assembly, with vessel valves	312.8 minutes (from vacuum on)	(1A, 1B, 1C, 4B, 4C, 7A, 10A)	Spacer disc, 28 mL of water added		
5	15-minute holds w/ normal 30 minute <2 Torr hold, preheated to 30–35°C, 220°C vessel heat tape setpoint, 105 mL water per assembly, with vessel valves	508.93 minutes (from preheating)	7 (1A, 1B, 1C, 4B, 4C, 7A, 10A)	Bulk water tray (version 1), 91 mL of water added, 0.822-inch water depth	100 W	Vessel wall = 220°C (428°F)
		311.7 minutes (from vacuum on)				
6	15-minute holds w/ normal 30 minute <2 Torr hold, preheated to 30–35°C, 100°C vessel heat tape setpoint, 105 mL water per assembly, with vessel valves	681.36 minutes (from preheating)	7 (1A, 1B, 1C, 4B, 4C, 7A, 10A)	Bulk water tray (version 2), 216 mL of water added, 0.822-inch water depth	100 W	Vessel wall = 100°C (212°F)
		493.3 minutes (from vacuum on)				
7	IFSF vacuum, 5 minute holds every 15 minutes, drying pressure between 10–90 Torr, IFSF 140°C preheat, 140°C vessel heat tape setpoint, 105 mL water per assembly, with vessel valves	433.16 minutes (from preheating)	7 (1A, 1B, 1C, 4B, 4C, 7A, 10A)	Bulk water tray (version 2), 216 mL of water added, 0.822-inch water depth	100 W	Vessel wall = 140°C (284°F)
		305.63 minutes (from vacuum/gas on)				
8	15-minute holds w/ normal	519.6 minutes (from preheating)	7	No	100 W	Vessel wall = 100°C (212°F)

	30 minute <2 Torr hold, preheated to 30–35°C, 100°C vessel heat tape setpoint, 105 mL water per assembly, with vessel valves, no water tray	316.26 minutes (from vacuum on)	(1A, 1B, 1C, 4B, 4C, 7A, 10A)			
9	IFSF vacuum, 5 minute holds every 15 minutes, drying pressure between 10–90 Torr, IFSF 140°C preheat, 140°C vessel heat tape setpoint, 105 mL water per assembly, with vessel valves	444.6 minutes (from preheating)	7 (1A, 1B, 1C, 4B, 4C, 7A, 10A)	Bulk water tray (version 2), 216 mL of water added, 0.822-inch water depth	100 W	Vessel wall = 140°C (284°F)
		321.73 minutes (from vacuum/gas on)				
10	IFSF vacuum, 5 minute holds every 15 minutes, drying pressure between 10–90 Torr, IFSF 140°C preheat, 140°C vessel heat tape setpoint, 105 mL water per assembly, with vessel valves, maintain 2.5 scfm inlet air flow rate	427.53 minutes (from preheating)	7 (1A, 1B, 1C, 4B, 4C, 7A, 10A)	Bulk water tray (version 2), 216 mL of water added, 0.822-inch water depth	100 W	Vessel wall = 140°C (284°F)
		300.6 minutes (from vacuum/gas on)				
11	IFSF vacuum, 5 minute holds	532.46 minutes (from preheating)	7	Bulk water tray (version 2),	100 W	Vessel wall = 140°C (284°F)

	every 15 minutes, drying pressure between 10–90 Torr, IFSF 140°C preheat, 140°C vessel heat tape setpoint, 105 mL water per assembly, with vessel valves, maintain 2.5 scfm inlet air flow rate, reduced drying pressure to 25 torr from 50 torr	403.06 minutes (from vacuum/gas on)	(1A, 1B, 1C, 4B, 4C, 7A, 10A)	216 mL of water added, 0.822-inch water depth		
12	15-minute holds w/ normal 30 minute <2 Torr hold, Preheated to 30–35°C, 220°C vessel heat tape setpoint, 105 mL water per assembly, with vessel valves, no water tray	479.63 minutes (from preheating) 271.8 minutes (from vacuum on)	7 (1A, 1B, 1C, 4B, 4C, 7A, 10A)	No	100 W	Vessel wall = 220°C (428°F)

Table 4. Isolation holds conducted during experimental vacuum-drying tests and their criteria to proceed to next vacuum step.

Vacuum Step, Hold Pressure	Isolation Hold Time for Tests Operated with 5 Minute Holds	Isolation Hold Time for Tests Operated with 15 Minute Holds	Criteria to Proceed to Next Step
<50 torr	5 minutes	15 minutes	<100 torr
<25 torr	5 minutes	15 minutes	<50 torr
<15 torr	5 minutes	15 minutes	<25 torr
<10 torr	5 minutes	15 minutes	<15 torr
<5 torr	5 minutes	15 minutes	<10 torr
<3 torr	5 minutes	15 minutes	<5 torr
<2 torr	30 minutes	30 minutes	<2.6 torr

For all drying tests, the initial bulk water content of the 10 mock ASNF assemblies was 105 mL dripped over the top of each assembly (via syringe), allowing the water to drip down the entire length of the assembly. This amount was predetermined to best simulate a “drip-dry” condition that is typical for ASNF prior to drying. In most vacuum tests, bulk water was further emulated through a simulated spacer disc and bulk water tray that are shown in a series of photos in Figure 16. Spacer discs are flat plates often found in light-water reactor storage canisters that are used to hold basket slots in place. They are used here as a proxy for spacer or alignment hardware that may be needed to accommodate three Type 1a baskets stacked vertically in a full-size, fully loaded DOE Standard Canister. The simulated spacer disc held 28 mL of water, replicating the flat or angular surfaces inside a canister. Two versions of the bulk water tray were utilized to mimic a water depth of 0.822 inches that could be present if all water from three fully loaded Type 1a baskets dripped to the bottom of a canister. Version 1 required 91 mL of water to achieve the 0.822-inch water depth, and Version 2 required 216 mL of water. The first iteration of the bulk water tray was abandoned due to the tray's thick wall having a high thermal inertia that could alter drying results. These trays were positioned in the middle viewport of the siphon port side of the chamber in view of a forward looking infrared (FLIR) camera, FLIR A325sc, that captured thermal images every 4 seconds through FLIR's ResearchIR software. Temperature reflections toward the camera were limited by adding Kapton tape to the trays.

Figure 16. Simulated spacer disc holding 28 mL of water (left), first iteration of bulk water tray simulating a water depth of 0.822 inch (middle), second iteration of bulk water tray simulating a water depth of 0.822 inch (right).

Temperature was monitored inside the chamber with Type K, Kapton insulated thermocouples that were spot-welded axially along four assemblies (Assemblies 1, 4, 7, and 10), two basket slots (basket corners of Assemblies 8 and 3 highlighted in Figure 17), and the siphon tube (orientation shown in Figure 17). As illustrated in a series of photos in Figure 17, thermocouple placement in the four assemblies provided axial interior and exterior assembly temperatures (plates indicated in red) and the ability to approximate temperatures of the corroded plates (plate indicated in blue). Assembly and basket thermocouples were identified based on their respective assembly (interior and exterior) or basket slot number and their axial location with A being the bottom and D being the top. Thermocouples were also attached to both sides (siphon port/inlet and vent port/outlet) of the chamber's exterior wall, as shown in Figure 18, and were identified axially in the same alphabetic manner. After completion of some of the initial tests, several thermocouples inside the basket were relocated to measure the water inside the simulated water trays, as some thermocouples were accidentally detached from their weld when inserting or removing assemblies and could not be reattached to their original locations. Accidental snagging of the thermocouples was alleviated when the previously mentioned ceramic thermocouple plugs were implemented. After FHD Test 6, all thermocouples were rewired from the data acquisition system to their respective thermocouple feedthroughs as a double reverse polarity in all wires was discovered causing an error in the readings. This does mean six out of the 10 FHD tests had inaccurate thermocouple readings. However, after resolving the thermocouple issue, two tests were operated (FHD Test 7 and 8) with the exact same heating conditions as the first 6 FHD tests. Thermal results showed the two tests varied from 0.04°C to 2°C across all thermocouples. Assuming nearly constant ambient temperatures throughout the testing regime, it was determined that the temperatures during the first 6 FHD tests were within 2°C of FHD Test 7 and 8. Although rare, some thermocouples lost signal during drying tests and were rectified once the experiment concluded.

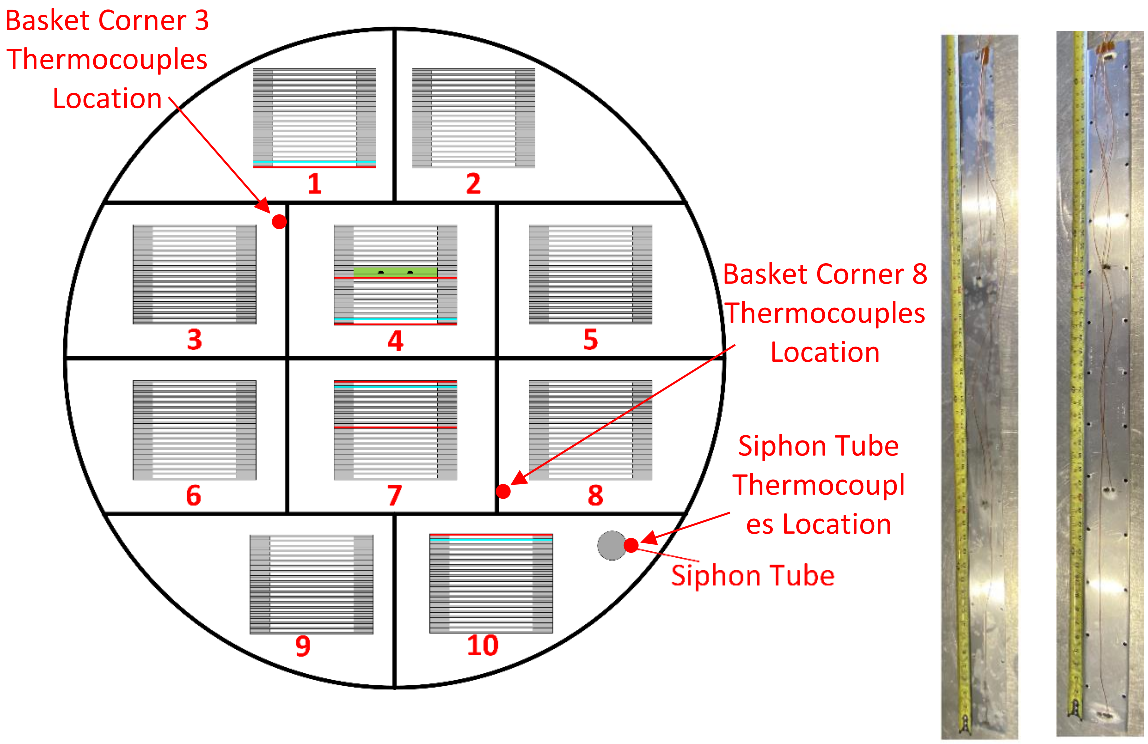

Figure 17. Diagram indicating locations of interior and exterior plates with thermocouples highlighted in red and corroded plates in blue (left), examples of interior and exterior plates with four evenly spaced thermocouples on each plate (right).

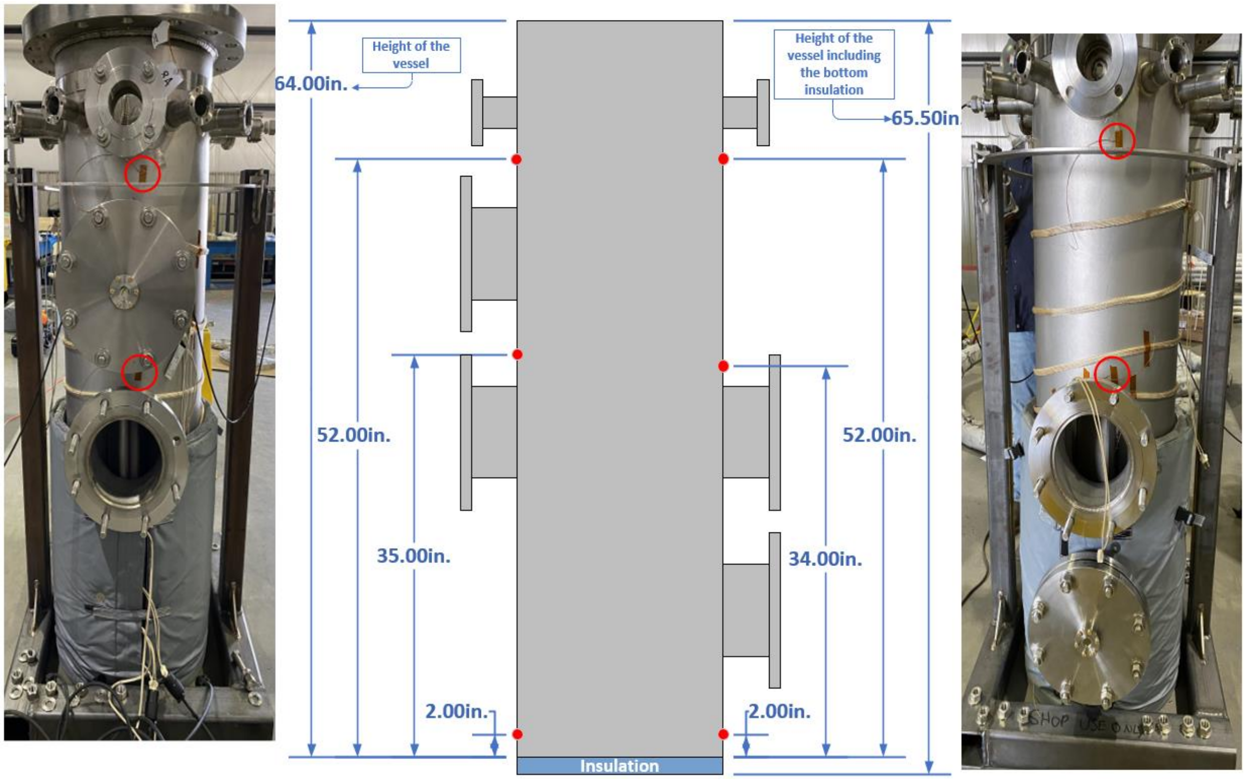

Figure 18. Diagram indicating locations of thermocouples attached to the exterior chamber wall with the vent-port side on the left and the siphon port side on the right.

Pressure and gas temperature near the siphon and vent ports (inlet and outlet for FHD) were measured using Holtec's pressure and resistance temperature detector (RTD) manifold displayed in Figure 19. Each side consisted of two Ashcroft high-pressure sensors and two Watlow RTDs for redundancy. All four pressure sensors and two RTDs (one on each side) were wired to Omega displays. The remaining two RTDs were integrated into the data acquisition system, but electrical noise from the output current of the data acquisition system resulted in the RTDs reading 2–3°C higher than the Omega displays at room temperature and 4–5°C higher at gas temperatures of 240°C. Measurements from the Omega displays were written down every 15–30 minutes while the inlet gas temperature was increasing and every hour after the maximum inlet gas temperature had been reached. Along with the gas temperatures, the flow rates during FHD tests were tracked by hand and paired with the data acquisition host time at the time of recording. This was to ensure all collected data are matched to one central timestamp. The flow meter used during FHD tests is shown in Figure 20. Original expectations underestimated the flow rate that would occur during FHD tests, requiring the flow meter to be recalibrated for higher flows. This was discovered during FHD Test 1, where the maximum inlet gas temperature achieved was 90°F at a mass flow rate of 3–5 lb/hr. Following FHD Test 1, nondrying tests were conducted to determine the optimal operating conditions (canister pressure and blower speed) to achieve a maximum constant inlet gas temperature of at least 238°C to ensure the fuel reaches temperatures of 220°C. The flow meter was not operational until FHD Test 4. However, an average flow rate of 105 lb/hr was consistent for all remaining FHD tests, indicating that the first 3 FHD tests operated at that flow rate as well.

Figure 19. Pressure and RTD manifolds located on the inlet and outlet (siphon and vent) of the drying chamber.

Figure 20. Flow meter utilized during FHD tests with an analog read out.

Two MKS-628 pressure sensors were employed to monitor the chamber pressure, in addition to the inlet and outlet pressures measured by the manifold described above, at low (0–100 Torr) and high (0–5000 Torr) pressures. Both pressure sensors were integrated at the same vacuum port and were capable of being valved off from the chamber, as seen in Figure 21. However, only the low pressure sensor was valved off for FHD tests as the high-pressure sensor was used in all drying tests. Delays in receiving the MKS sensors due to Covid-19 resulted in the sensors not being integrated into the system until FHD Test 4. Prior to implementing the MKS pressure sensors, chamber pressure during FHD experiments was approximated based on the average between the inlet and outlet pressure.

Figure 21. MKS-628 high and low pressure sensor attached to 2.75-inch Conflat manual valves attached to the drying chamber.

Humidity inside the chamber was monitored using a relative humidity probe, Vaisala HMT 334, that was capable of high-temperature applications. Figure 22 shows the probe outside of the port (left) as well as installed in the vacuum port adjacent to the MKS pressure sensors (right). The humidity probe was integrated into the data acquisition system to track the relative humidity and temperature at the probe. Measurements from the relative humidity probe for FHD tests were only accurate for the first several hours due to the extreme temperature conditions experienced midway through the tests. However, Holtec's dew point sensor at the FHD skid was used as another method of monitoring the moisture content inside the vessel.

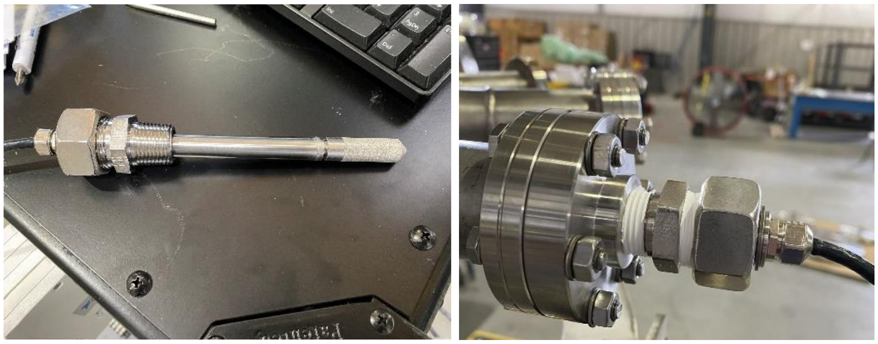

Figure 22. Vaisala HMT 334 relative humidity probe (left), relative humidity probe attached to vacuum port using a National Pipe Thread to Conflat adapter.

In addition, gas stream moisture content inside the chamber was monitored using a direct-current-driven plasma discharge and optical emission spectroscopy (OES) system calibrated for gas mixtures of helium and water vapor which can be seen in Figure 23. However, using the OES to determine when all bulk water had been removed during FHD experiments was abandoned after noticing the high sensitivity in the OES resulted in little to no decrease in the water content throughout each test. The method of drying for FHD tests did not involve Phase 2 drying, meaning that very low levels of moisture recirculated in the system. Therefore, the OES continually picked up the trace amounts of vapor that remained. Eventually, the OES was primarily used to determine if any air was present in the system prior to the start of drying experiments.

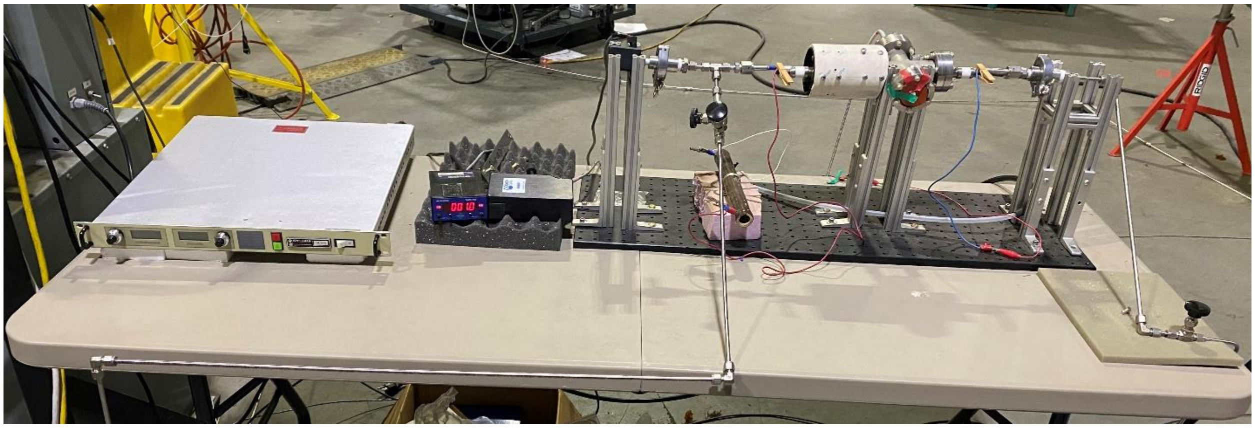

Figure 23. OES system and direct current power supply used to generate plasma discharge.

Data collection during drying experiments was performed by a custom-built National Instrument PXI System pictured in Figure 24. The PXI chassis housed hardware cards that supported the integration of various temperature, pressure, and humidity sensors into LabView for real-time data acquisition. Specific model numbers of the PXI chassis, cards, and equipment are listed in Appendix A. At the conclusion of each experiment, LabView generated test data files. A Python script was then used to transfer the data into Excel for analysis.

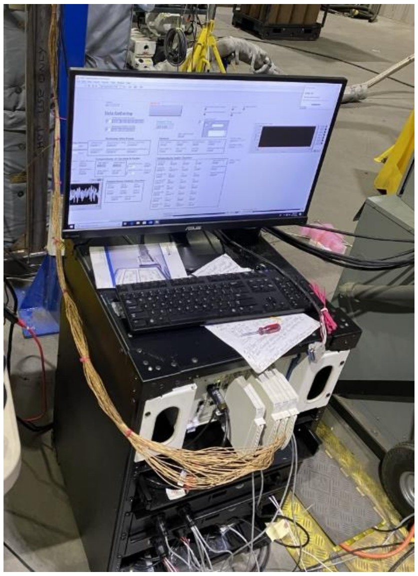

Figure 24. National Instruments PXI System used to integrate all National Instruments compatible instrumentation into LabView through the PXI Chassis.

All three types of drying tests (FHD, non-IFSF vacuum drying, and IFSF vacuum drying) began with a full system pressure test (FHD and non-IFSF vacuum tests used helium, IFSF tests used air) for 10 minutes at approximately 30 psig to check for any leaks in the system. Minor leaks observed prior to FHD tests were attributed to the seals on the blower with the leaks disappearing, in most cases, once the blower warmed up. Other negligible leaks were noted but were not a concern in affecting the overall drying performance. During vacuum tests, the FHD skid was sealed off from the drying vessel so that the FHD skid leaks were not a factor.

For FHD tests, the system was then purged with helium gas, first with the FHD blower off and then with it turned on, until the OES observed little to no air in the system. After the air was purged, drying was initiated (heated helium gas began to enter the cannister) with all heating elements being turned on. FHD tests were conducted at 70 psig with occasional venting and addition of helium to maintain such pressure. Though dew point and OES measurements were taken, FHD tests were concluded after any of the external plate thermocouples (thermocouples used to determine corroded plates temperatures) had achieved the test's target temperature for that test's target drying time.

For non-IFSF vacuum-drying experiments, pressure tests were followed by purging the system with helium gas. In contrast to the FHD tests, IFSF and normal vacuum-drying tests included an additional step of preheating the assemblies to a predetermined temperature at the start of drying operations. For normal vacuum-drying tests, this was achieved by setting the heating tapes on the chamber wall to 50°C until all assemblies were >25°C and then reducing the heating tapes to 25°C to allow all the assemblies to reach a steady-state. Heating tapes were reduced to ensure the assemblies near the chamber wall were within 5°C of the two assemblies located toward the center of the basket at the start of drying operations. Although the temperature setpoint was reduced, the thermal mass of the chamber wall continued to gradually heat the assemblies. Once all assemblies were between 30 and 35°C, the heating tapes were increased to their desired test temperature (100°C, 150°C, or 220°C), the assembly heater element was turned on, and evacuation commenced. The heater simulating decay heat (in Assembly 4) was left off during the preheat, because preheating required approximately three hours to complete. Running the heater during this preheat period would have resulted in Assembly 4 starting the drying operation at higher temperature than would typically be expected for ASNF. Non-IFSF vacuum-drying tests were operated with isolation holds at 100, 50, 25, 15, 10, 5, 3, and <2 Torr to monitor the pressure rise inside the chamber to see if the test could proceed as noted previously. Prior to Vacuum-Drying Test 4, isolation holds were initiated at the vacuum skid, leaving extra piping (6–12ft) open to the vessel. However, vent and siphon isolation valves seen in Figure 25 were added directly off the chamber after freezing was discovered in the lines resulting in inaccurate pressure rebounds during holds. Drying was deemed complete if the pressure did not rebound above 3 Torr and increase by more than 1 Torr during the 30 minute <2 Torr hold.

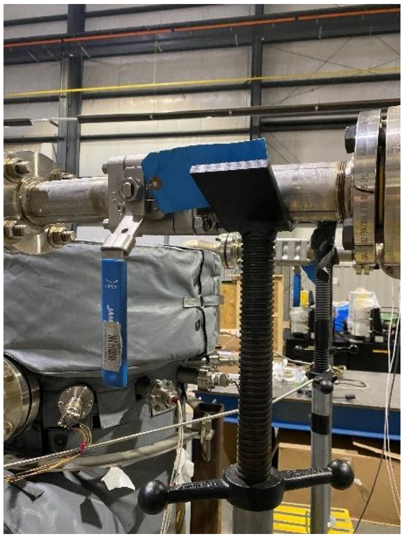

Figure 25. Vent and siphon isolation valves used in normal and IFSF vacuum-drying tests.

The preheating phase for IFSF vacuum-drying tests consisted of heating the chamber wall to 140°C and holding it for 30 minutes. At the end of the preheat period, IFSF drying operation discussed in Section 3 was initiated. For this setup, IFSF vacuum-drying tests were conducted following INL's IFSF standard drying procedure with compressed air flowing (nominally 2.5 scfm at 80 psig) through the siphon while the vacuum pump pulls from the vent to maintain a chamber pressure between 10 and 90 Torr (nominally operating at 50 Torr). After achieving the drying pressure, a cycle of vessel isolations and pressure rate measurements were conducted every 15–30 minutes for a duration of 3–10 minutes (most tests were isolations every 15 minutes for 5 minutes). Experimental IFSF drying tests utilized the same IFSF drying criteria that was outlined in Section 3.

Following the conclusion of all three drying test types, the system was vented (or backfilled with helium) to atmospheric pressure, sealed, and left to cool until it was safe to remove the corroded plates from the assemblies. Though some iterations were made over time to each drying setup, the final version of the drying schematics are shown in Appendix B.

6.1 FHD Process Performance

Pressure fluctuations were observed in all FHD tests due to the frequent purging and venting of helium to maintain a chamber-inlet (siphon) pressure of 70 psig. Although the magnitudes of these fluctuations varied from test to test, as shown in Figure 26, for pressure inside the chamber, each test experienced a pressure differential of 12.5 psig across the canister (chamber) and a mass flow rate ranging from 100 to 110 lb/hr.

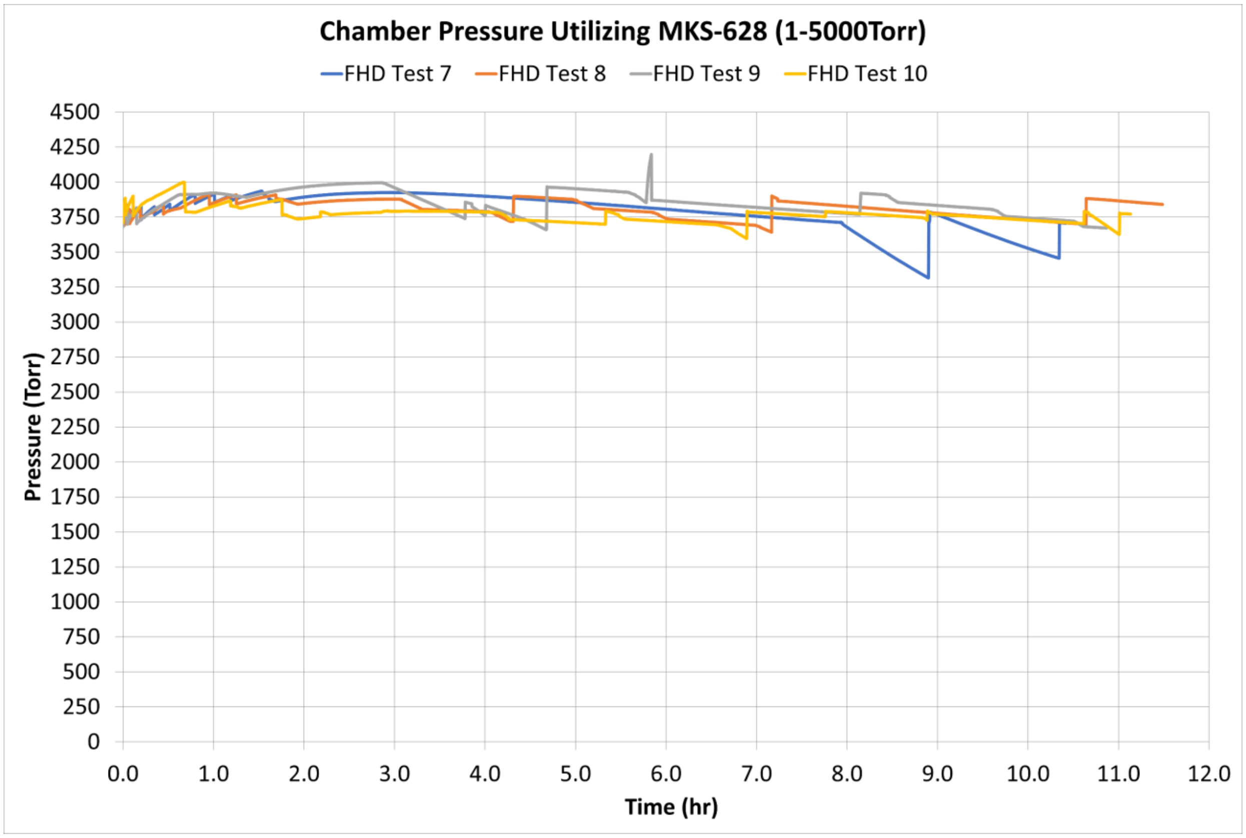

Figure 26. Chamber pressure for FHD Tests 7–10 illustrating the fluctuations due to maintaining an inlet pressure of 70 psig. Pressure is measured using an MKS-628 pressure sensor with a range of 1–5,000 Torr.

The chamber's inlet gas temperature was maintained at approximately 239°C. This consistency was achieved by setting the FHD heaters to 260°C and using heating tape wrapped near the chamber inlet. Only FHD Test 10 operated at a lower inlet temperature of 220°C (FHD heaters at 246.67°C) to ensure the corroded plates did not exceed 220°C during drying. Although FHD Test 10 operated at a lower temperature, Figure 27 demonstrates that the chamber's inlet gas temperature for all tests reached steady-state approximately 2 hours after energizing the FHD heaters. (Individual data sets have minor discontinuities; the average is shown here for clarity.)

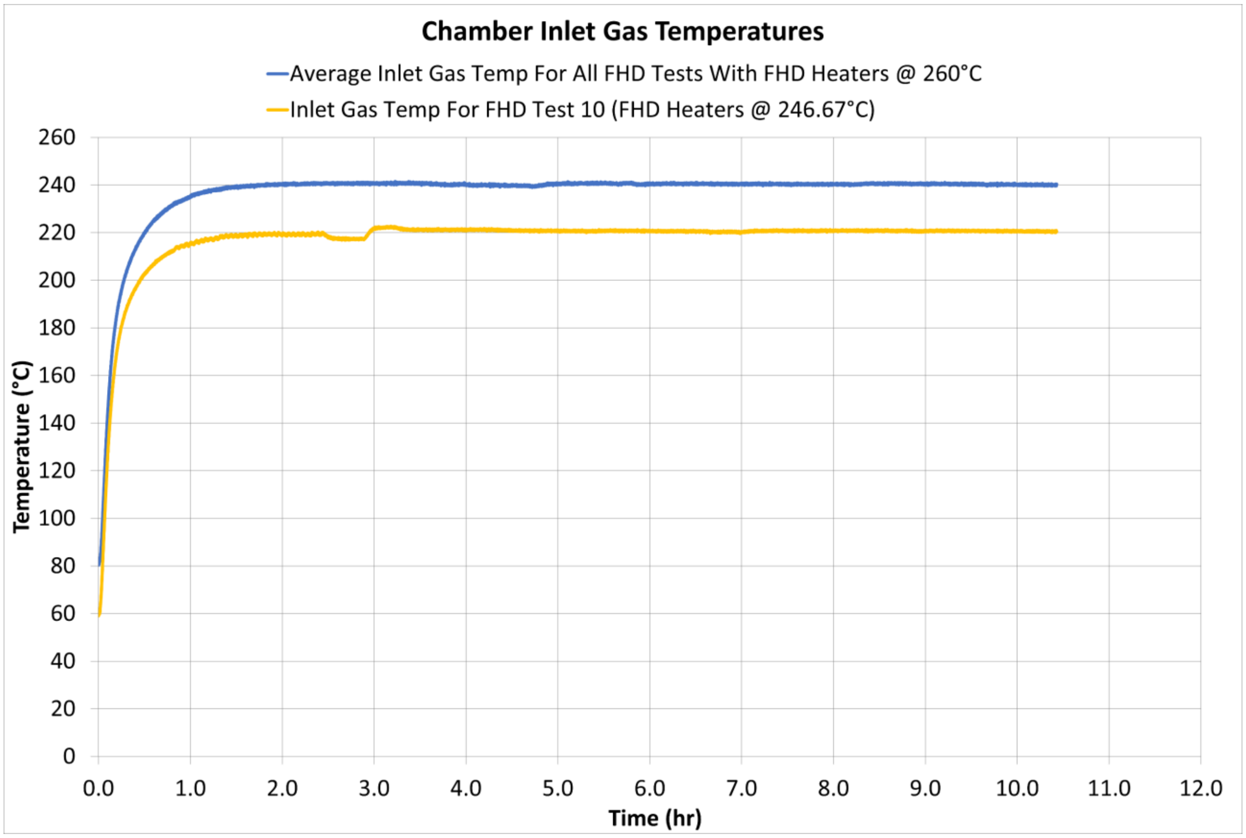

Figure 27. Comparison between FHD Test 10 chamber-inlet gas temperature and the average inlet gas temperature for all FHD tests operating with FHD heaters at 260°C.

Thermal performance based on drying time was evaluated through two plots, shown in Figure 28, containing the average temperature of each assembly (Assemblies 1,4, 7, and 10) for an 8 hour and 12 hour test (FHD Test 7 and 8) with similar maximum gas and chamber wall temperature conditions. The drop in temperature for Assembly 4 during FHD Test 7 was due to the nichrome wire briefly losing power. Overall, drying time had a minimal impact as the heating rate for all assemblies for both tests had reached steady-state, a temperature increase of less than 0.1°C in 30 minutes, 7 hours from the start of drying. There was also little difference in peak temperature as the 12 hour test only showed temperatures up to 2°C higher than the 8 hour test. The little deviation in maximum temperature (specifically the assembly simulating decay heat) illustrates the effectiveness of the FHD operation in controlling the fuel temperature through forced convective heat transfer. This forced convection from the circulating heated helium provided sufficient energy to heat the ASNF assemblies to between 225°C and 235°C. Although Assembly 4 was supplied with 100 W decay heat, thermal equilibrium was still achieved through concurrent fuel cooling promoted by the turbulent helium.

The image on the left in Figure 29 shows the axial temperature profile of Assembly 1 observed during FHD Test 7. As expected, at the start of the drying test, the heating rate for the bottom of the assembly was much larger than the top as a result of the heated gas entering through the siphon tube and traveling up through the vent port. However, the temperature of the top of the assembly surpasses the temperature of the bottom of the assembly near the 3-hour mark. This atypical bottom-to-top heating profile was seen in the four measured assemblies for all tests that operated the chamber wall heating tapes at 260°C. Although uniformity was confirmed under ambient atmospheric conditions for a wall temperature of 260°C, this atypical heating profile was probably due to the spacing of the heating tapes and the forced convection occurring during FHD. Therefore, FHD Test 9 was conducted with the heating tapes set to 75°C to demonstrate the effect of varying wall temperature. As shown in the image on the right in Figure 29, FHD Test 9 successfully demonstrated that a more uniform axial temperature profile is achieved when heating is controlled by the recirculating heated gas rather than the heated chamber wall. While the lower wall temperature precluded achievement of the 220°C target temperature at the assemblies, the concurrent increase in the inlet gas temperature to Holtec's current operating maximum of 260°C would readily meet that target.

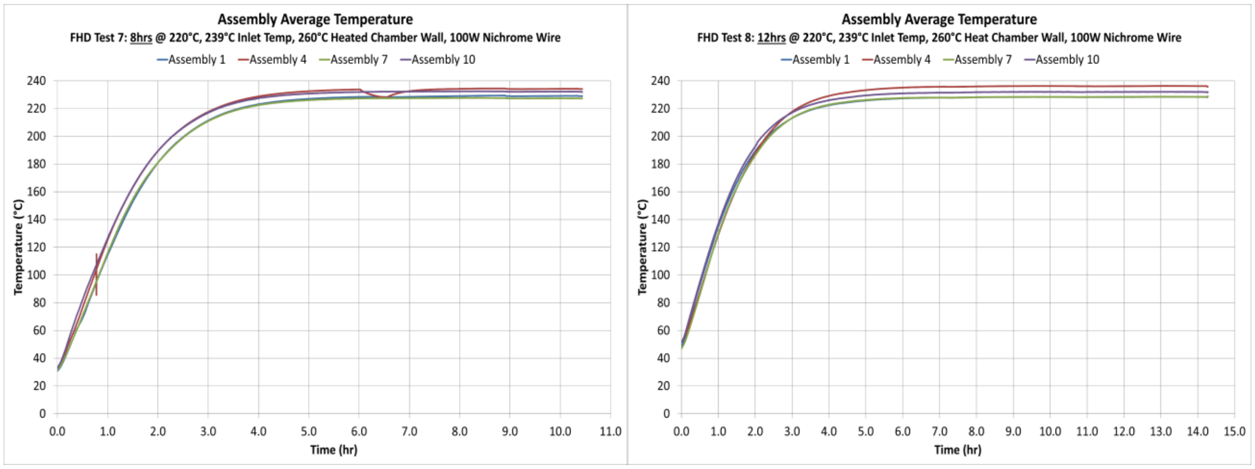

Figure 28. Average temperature of select assemblies for FHD Test 7 (left), average temperature for select assembly for FHD Test 8 (right).

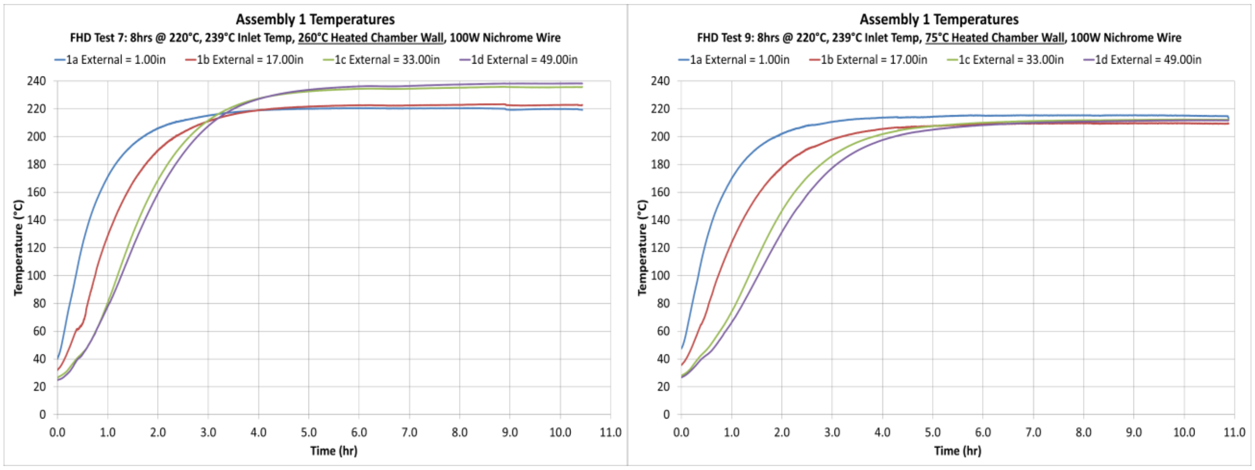

Figure 29. Axial temperature profile of Assembly 1 for FHD Test 7 (left); axial temperature profile of Assembly 1 for FHD Test 9 (right).

Bottom-to-top temperature lag plots of Assemblies 1, 4, 7, and 10 in Figure 30 were generated for FHD Test 7 (239°C inlet, 260°C heat tapes), Test 9 (239°C inlet, 75°C heat tapes), and Test 10 (220°C inlet, 75°C heat tapes) by subtracting the temperature at the top of the assembly from the bottom. As expected, these plots highlight again the asymmetric heat profile generated when the heat tapes were set to 260°C, as negative values in the figures indicate how much hotter the top of the assembly was compared to its bottom. Among the three tests, FHD Test 7 was the only test where all assemblies had a negative temperature lag at the end of the test, indicating that the hottest location of all assemblies was at the top at the conclusion of the drying operation. While there was little deviation in the time that each test achieved their peak temperature lag, when decreasing the heating tapes to 75°C, there was noticeable change in the peak temperature lag for Assemblies 1 and 4, increasing up to a 15°C temperature lag. The peak temperature lag decreased for all assemblies by 5–10°C when both the inlet gas and heating tapes temperatures were reduced. This was expected, as the bottom of the assemblies decreased in overall temperature due to the decrease in inlet gas temperature. Among all the assembly temperature lags, the Assembly 7 external plate was the least affected by the thermal changes with its peak temperature lag deviating by only 5°C. Although bottom-to-top temperature lag plots provide little feedback on the effectiveness of FHD operation, these figures give insight into the overall thermal condition of the assemblies, which is useful for the development and validation of drying models.

Relative humidity data collected during the FHD tests indicated that the majority of bulk water is removed within the first 3 hours of drying. However, when comparing humidity data in Figure 31 for FHD Test 7, 9, and 10, drying time varied based on the thermal conditions. FHD Test 7 took approximately 159 minutes to achieve a humidity of <1%. Reducing the heating tapes to 75°C resulted in FHD Test 9 not achieving <1% humidity until after 271 minutes. Drying time was further increased to 379 minutes with the reduction of the inlet gas temperature for FHD Test 10. Overall, the drying rates for the three tests were similar until deviation occurred 1 hour after the start of the drying process.

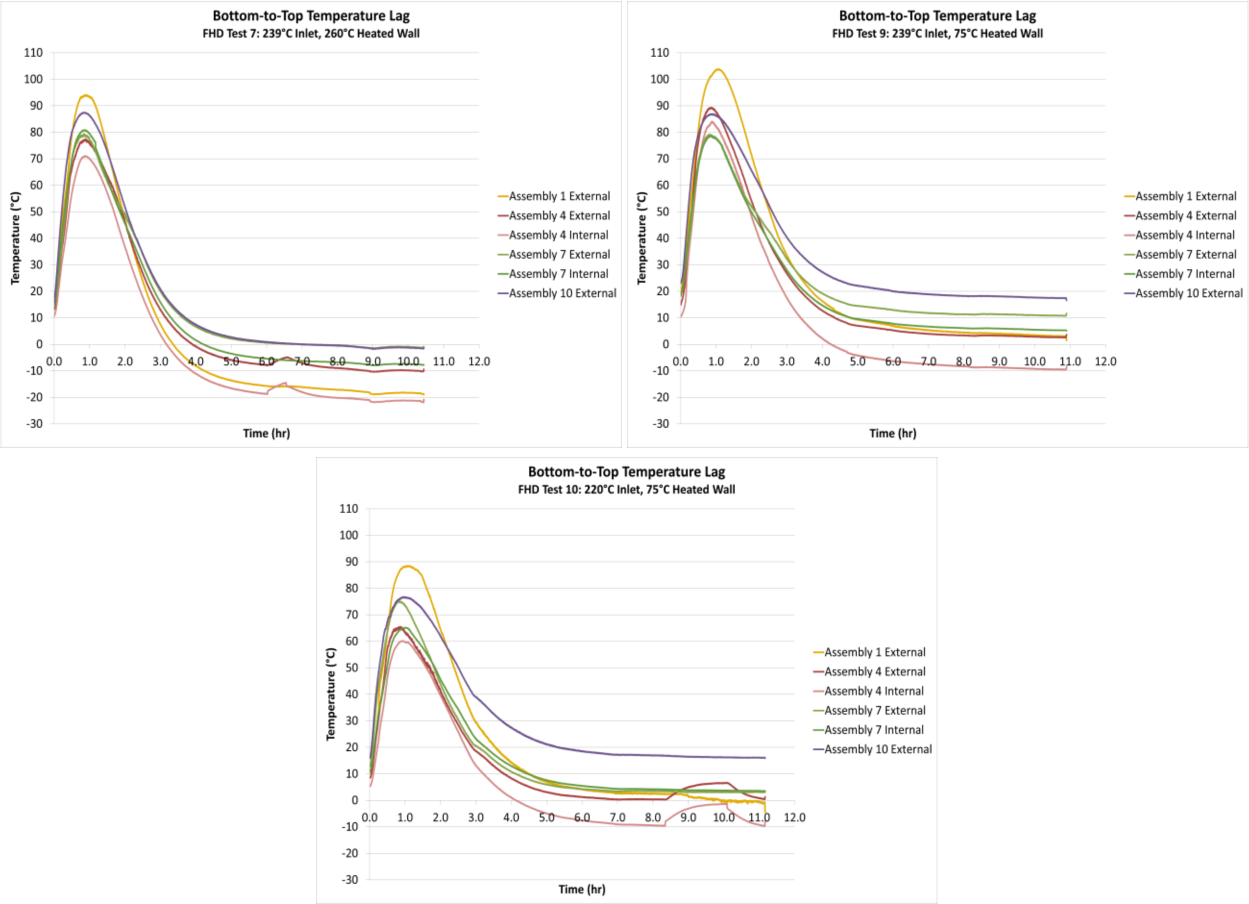

Figure 30. Bottom-to-top temperature lag of select assemblies for FHD Test 7 operating at 239°C inlet gas and 260°C wall heat tapes (top left), FHD Test 9 operating at 239°C inlet gas and 75°C wall heat tapes (top right), and FHD Test 10 operating at 220°C inlet gas and 75°C wall (bottom).

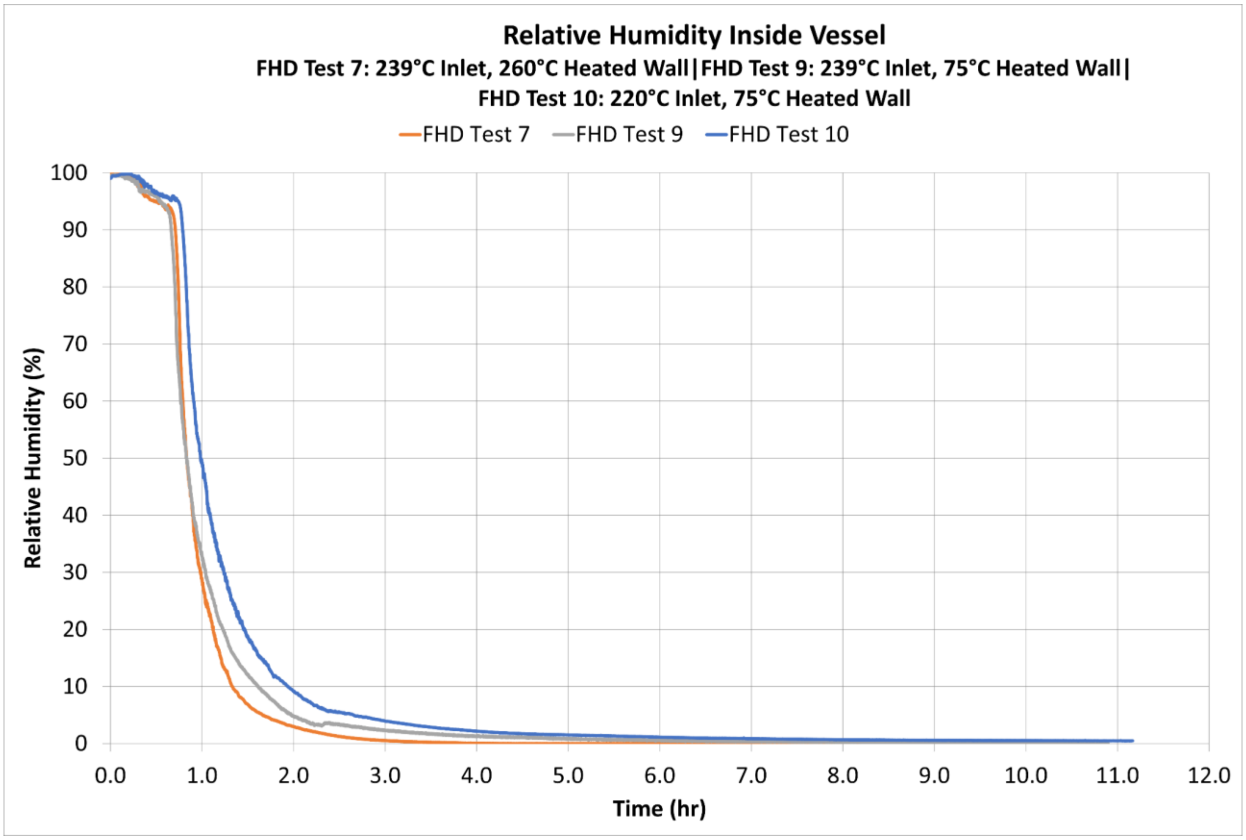

Figure 31. Comparison of relative humidity measured inside the vessel for FHD Test 7, 9, and 10.

6.2 Vacuum-Drying Process Performance

During the first two vacuum-drying tests, freezing was observed inside the simulated spacer disc when evacuating to the 3 Torr isolation hold. In attempt to prevent freezing, Vacuum-Drying Test 3 was operated with 15 minute holds rather than 5 minute holds. Although cooling is expected from evaporation during vacuum drying, extending the holds successfully prevented the formation of ice, as shown in Figure 32, where the water temperature inside the simulated spacer disc for Vacuum-Drying Test 2 did drop below 0°C, but Test 3 did not. However, freezing was identified in the siphon and vent lines during Vacuum-Drying Test 3, resulting in the test being prolonged. Vent and isolation valves were implemented following Test 3 to prevent moisture in the lines from giving false readings during isolation holds.

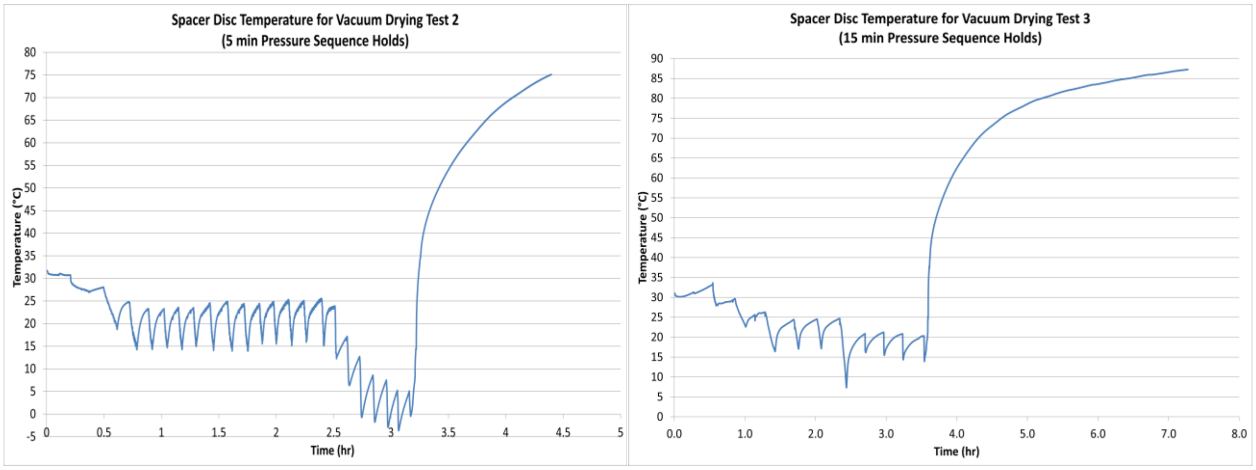

Figure 32. Spacer disc temperature for Vacuum-Drying Test 2 where 5 minute isolation holds were used (left), spacer disc temperature for Vacuum-Drying Test 3 where 15 minute isolation holds were used (right).

As illustrated in Figure 33, monitoring of all vacuum-drying tests revealed that only relatively small rebounds in the relative humidity occurred once the water temperature inside the spacer disc or bulk water tray increased. This observation indicated that the trays were the last location inside the chamber containing bulk water. Another trend observed during vacuum-drying tests is shown in Figure 34 where a significant reduction in the relative humidity was seen when the heating rate of the bottom of Assembly 10 (Thermocouple 10a) surpassed that of Thermocouple 10b (the thermocouple above 10a). This heating rate change is believed to be a result of all water being removed at that location, as the temperature at the bottom of Assembly 10 was no longer controlled by the vapor pressure of water. This concept of monitoring drying through temperature has been widely used in pharmaceutical vacuum drying as, when water is fully removed, the temperature at that location will increase even under vacuum due to either conductive or radiative heat transfer.[30] The relative humidity reduction occurred at the 6 hour mark for the example given (Vacuum Drying Test 5). For tests that utilized a water tray, this relative humidity reduction and heating rate change occurred at the 6 hour mark for the example given in Figure 34. For tests that used a water tray, this relative humidity reduction occurred before the water tray was dried. Therefore, although Figure 34 does not indicate exactly when the assemblies dried for these vacuum tests, it does give the indication that the remaining humidity in the vessel after the 6 hour mark is associated with water in the spacer disc (or bulk water tray). This theory that the assemblies were drying faster than the water trays was confirmed by conducting two vacuum-drying tests (Vacuum-Drying Test 5 and 12) with and without the bulk water tray under the same operating conditions. The test without the tray achieved the target dryness level approximately 45 minutes faster than the test with the tray. The drying time difference was ultimately a result of the evaporation process, which is dependent on the surface area of the water. For the assemblies that were simply wetted with 105 mL of water each, the surface area of the water exposed to the gas inside the vessel was large relative to the volume of water added. For the case of the tray, the surface area of the water was small relative to the volume of water inside the tray. As a result, more water was evaporating from the assemblies at any given moment compared to the water in the tray.

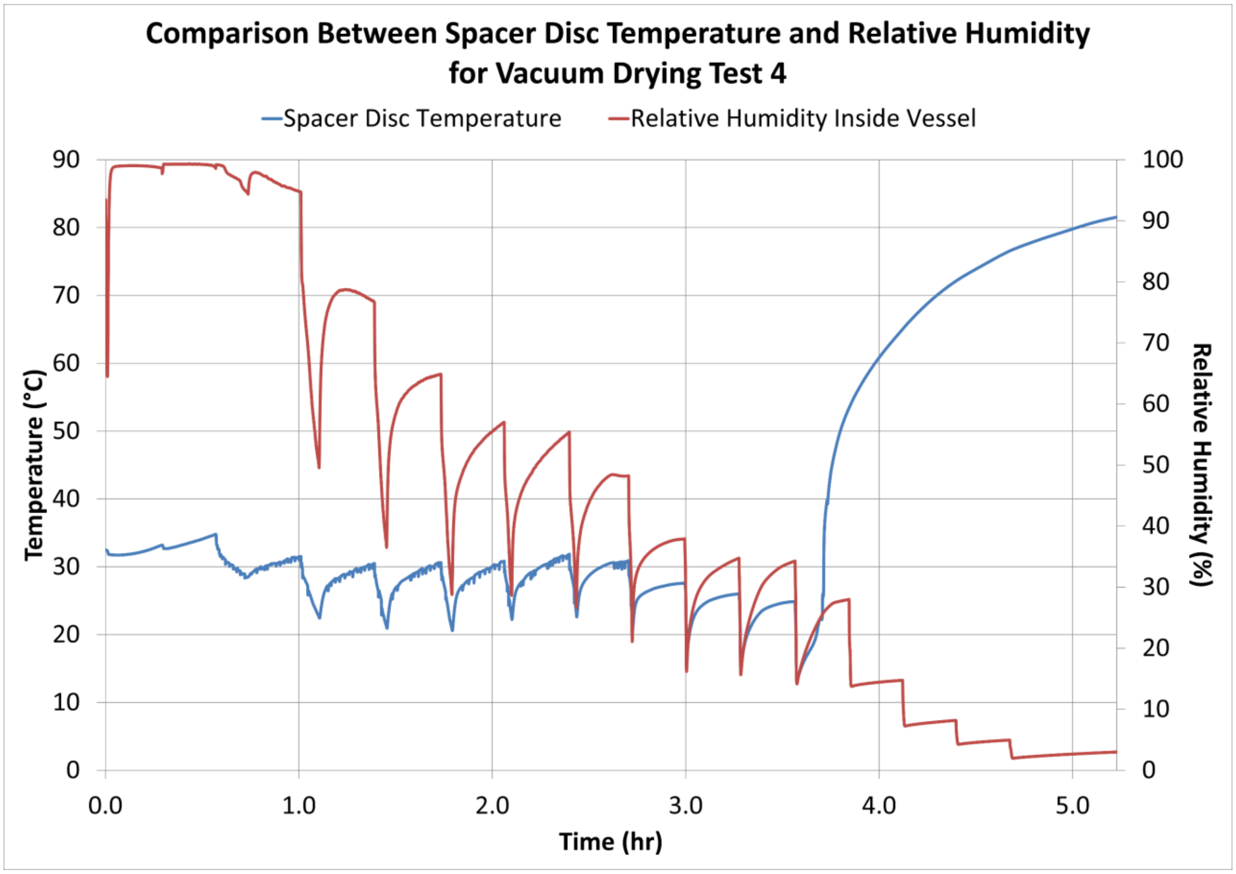

Figure 33. Simulated spacer disc temperature and relative humidity inside the vessel comparison for Vacuum-Drying Test 4.

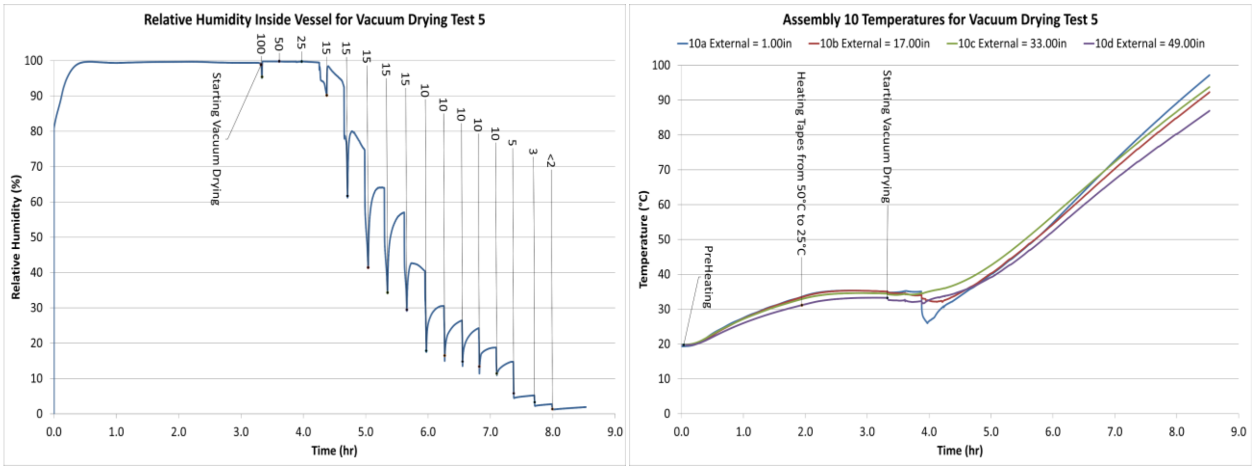

Figure 34. Relative humidity inside the vessel for Vacuum-Drying Test 5 (left), axial temperatures of Assembly 10 for Vacuum-Drying Test 5 (right), Assembly 10a's heating rate is seen to increase at the 6-hour mark.

For all normal vacuum-drying tests, the vacuum booster pump had to be energized when evacuating to 15 Torr, as the rate of evacuation began to slow down substantially due to the rate of evaporation increasing inside the chamber. Figure 35 provides an example from Vacuum-Drying Test 4 of the pump down speed decreasing prior to the 25 Torr hold. For this example, the booster pump was initiated immediately following the 25 Torr hold. In commercial drying, the booster pump is typically energized at 20 Torr.

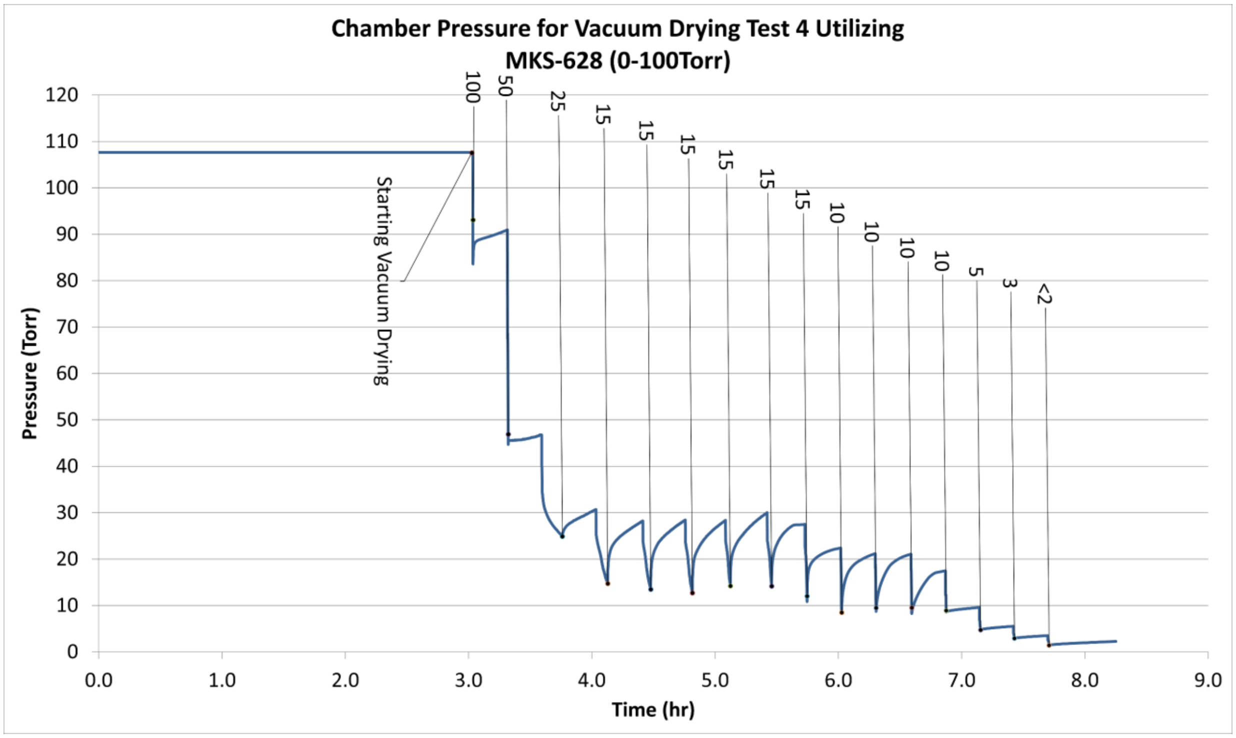

Figure 35. Chamber pressure for Vacuum-Drying Test 4 measured by MKS-628 pressure sensor with a range of 0–100 Torr.

Deviations in drying time were mostly seen through deviations in the temperature setpoint for the chamber wall’s heating tapes as the tapes were the main source of heat (excluding nichrome wire) in vacuum-drying tests. This can be seen in Figure 36, where Vacuum-Drying Test 8 and 12 were conducted with the same water content (105 mL per assembly, no water tray) but Test 8 operated the heat tapes at 100°C and Test 12 operated them at 220°C. The 120°C temperature difference on the wall resulted in Test 12 drying in 270 minutes, which was almost 50 minutes faster than Test 8. Assembly temperature plots for Vacuum-Drying Test 8 and 12 are shown in Figure 37 to illustrate the temperature profiles at the same thermocouple locations throughout the two tests; test-to-test temperature differences range from 5–30°C at the same location. Assembly 1 and 10 were most affected due to their proximity to the chamber wall. One limitation to the vacuum-drying tests was the relatively low thermal conditions. This was experienced in Vacuum-Drying Test 6 (100°C heating tapes) where the drying test lasted over 8 hours until it was ended early (at 10 Torr) after seeing minimal signs of moisture being removed from the bulk water tray.

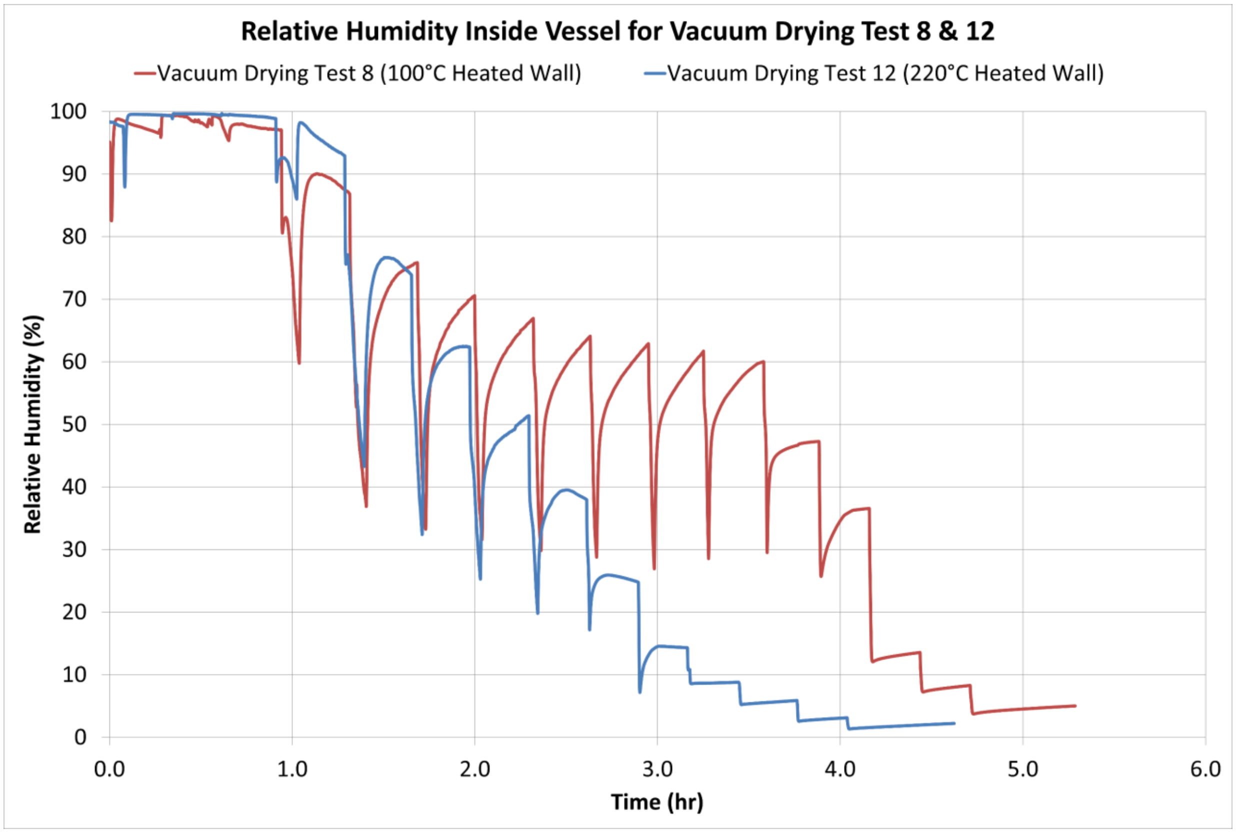

Figure 36. Comparison of relative humidity for Vacuum-Drying Test 8 (100°C wall heat tapes) and Vacuum-Drying Test 12 (220°C wall heat tapes).

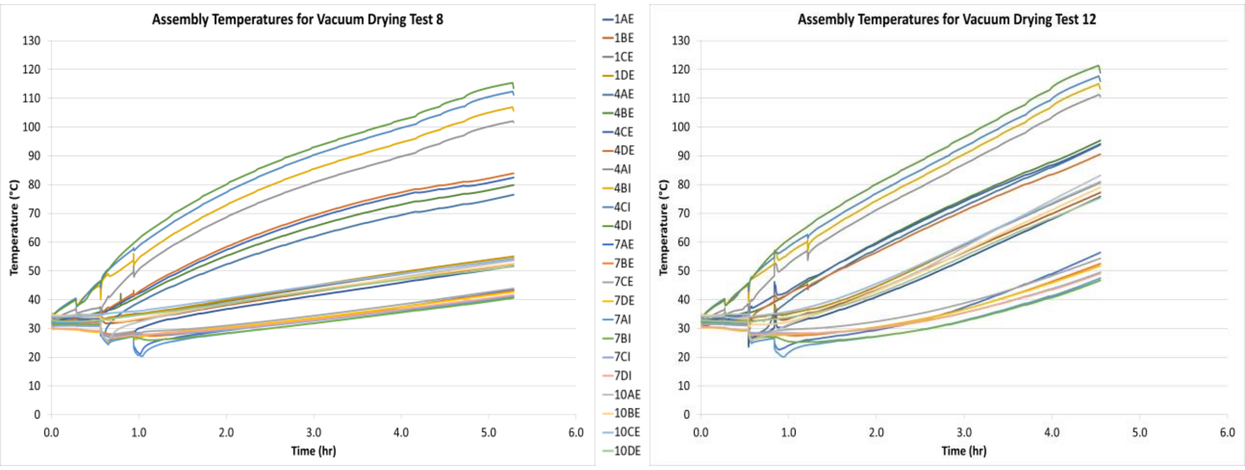

Figure 37. Comparison of assembly temperatures for Vacuum-Drying Test 8 (left) and Vacuum-Drying Test 12 (right), legend in the middle correlates to the assembly number, thermocouple axial location, and whether it is located on an external or internal plate.

The reduction in pressure under vacuum impedes heat transfer by limiting the transfer of kinetic energy within the system (fewer gas particles means fewer gas particle collisions). As shown in Figure 37, the vacuum operation is unable to control assembly temperatures during drying without backfilling the vessel with helium (occasionally done in industry to reduce fuel temperature during operations) or otherwise providing a circulating medium for convection at the surface of the assemblies. Assembly 4's higher temperature readings compared to the other assemblies were a result of the conduction applied from the 100 W simulated decay heat. All other assemblies relied solely on the convection heat transferred from the heated chamber wall. Therefore, because heat energy is required for vaporization of the bulk water, Assembly 4 is believed to have dried faster than the other nine assemblies inside the vessel. Although there is no experimental data to show each assembly's drying rate, modeling results in Section 8.2.2 do support the claim of Assembly 4's bulk water achieving complete vaporization before all other assemblies.

IFSF vacuum-drying tests were successful in fully removing the bulk water (105 mL) added to each assembly as there were no physical observations of moisture on any of the assemblies following each test. However, residual bulk water photographed in Figure 38 was found after every IFSF drying test inside the bulk water tray and in the form of condensation on the viewports. The water temperature at three different heights inside the bulk water tray displayed in Figure 39 showed that saturation pressure during IFSF Test 2 (Vacuum-Drying Test 9) was much less than the 50 Torr system pressure. Therefore, the only mechanism for liquid water removal was evaporation. As a result, only the assemblies themselves were dried, as evaporation depends on the surface area and the differential between the saturation pressure of the water and the vapor pressure in the gas stream.

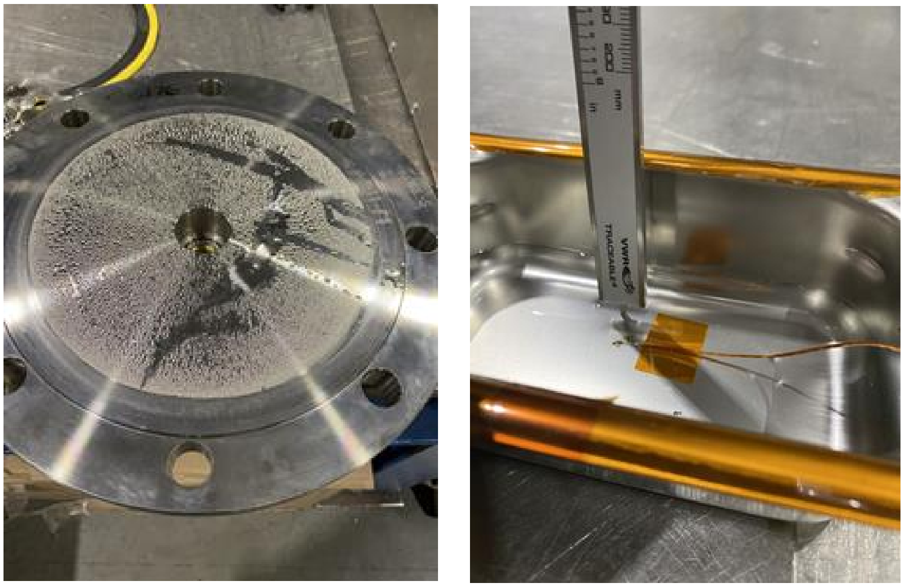

Figure 38. Bulk water found on viewport (left) and bulk water tray (right) after IFSF Vacuum-Drying Test 1–3.

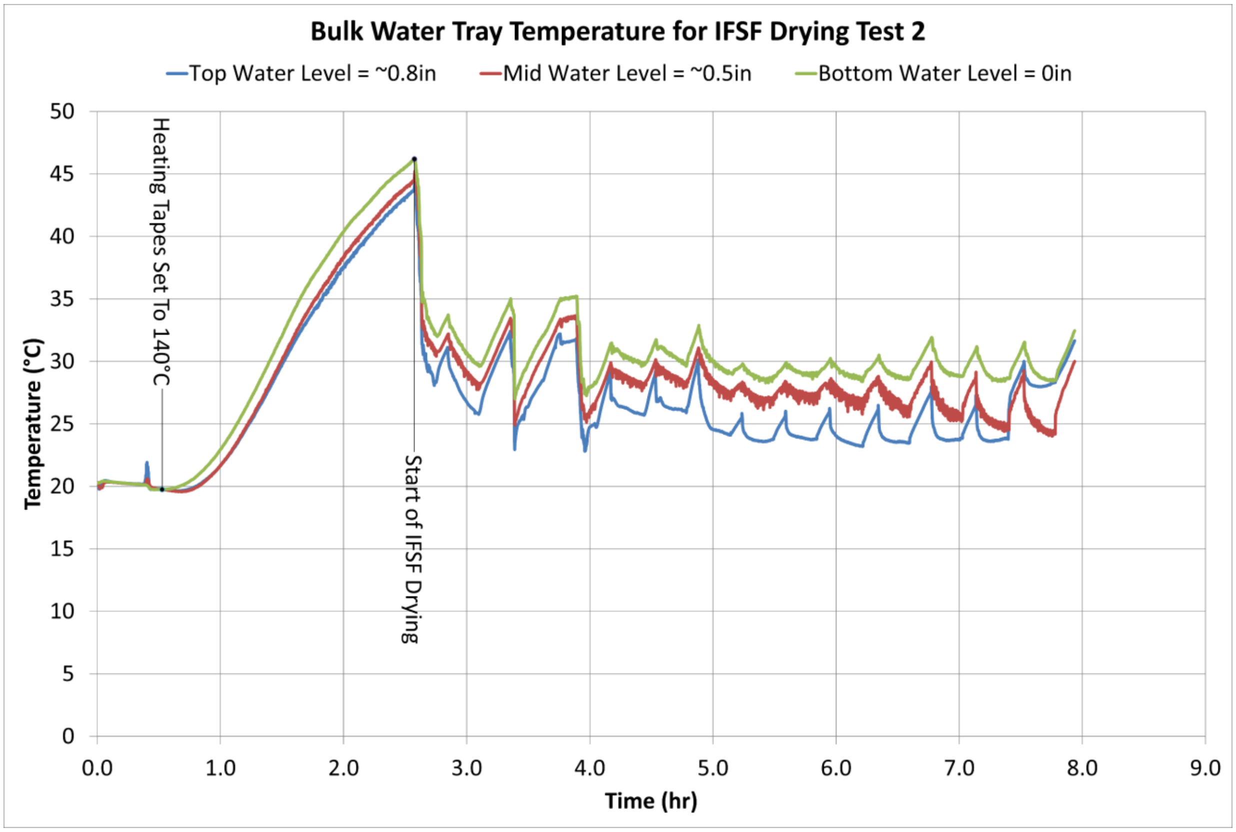

Figure 39. Water temperature at three different heights inside the bulk water tray for IFSF Drying Test 2.

In an attempt to promote more boiling inside the bulk water tray, IFSF Test 4 was operated at a reduced drying pressure of 25 Torr. However, a cycle of rapid pressure reductions to approximately 15 Torr shown in Figure 40 was implemented halfway through the drying test to force boiling to occur after observing that the rate of evaporation was greater than the rate at which the water would take in heat from the tray wall. In other words, the water inside the tray was not getting hot enough to reach the saturation temperature required (38°C) to promote boiling at the vessel operating pressure of 50 Torr. IFSF drying tests that were operated at the 50 Torr and 2.5 scfm flow rate showed very little boiling and only removed approximately 0.5 inches (~85 mL of residual water) out of the 0.822 inches of bulk water. However, IFSF Test 4 demonstrated a substantial amount of boiling; only 3 mL of water was observed inside the bulk water tray following the drying test. All IFSF drying tests had similar relative humidity plots like IFSF Test 3's plot shown in Figure 41 with significant rebounds occurring during the final holds. These rebounds give indications of moisture still residing in the vessel even though one of the two IFSF drying criteria had been met. Although no IFSF tests were conducted without the bulk water tray, Figure 42 shows a similar trend previously found in the normal vacuum-drying tests where a significant relative humidity reduction occurs when Thermocouple 10a (at the bottom of Assembly 10) surpasses Thermocouple 10d (near the top of Assembly 10) in temperature. On this basis, the bulk water was inferred to have been completely removed within 3 hours after drying was initiated.

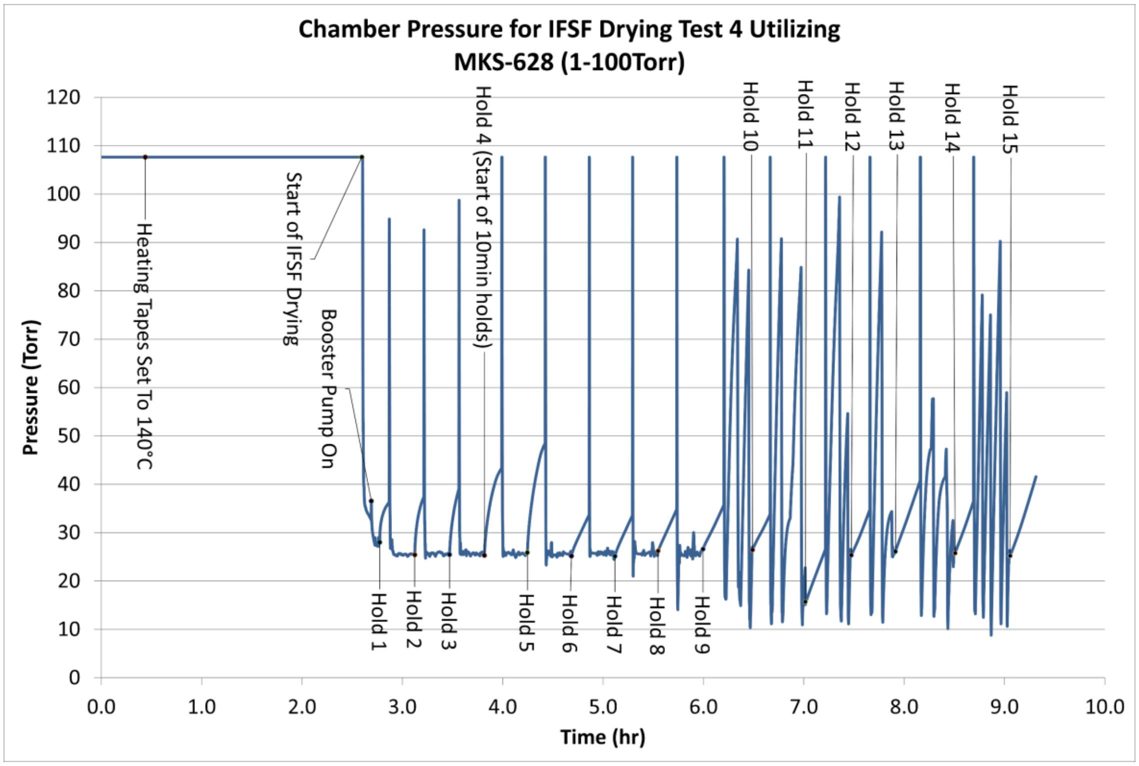

Figure 40. Chamber pressure for IFSF Drying Test 4 demonstrating the cycle of rapid pressure reductions beginning after Hold #9, pressure measured with MKS-628 pressure sensor with a range of 0–100 Torr.

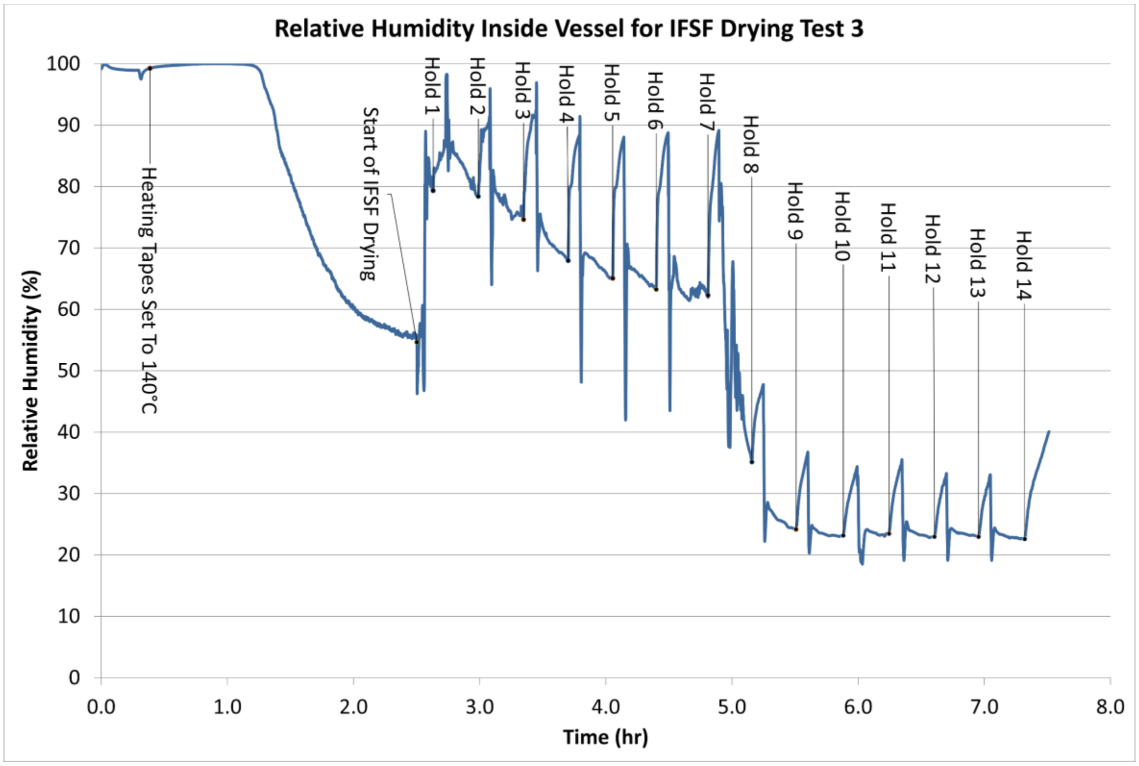

Figure 41. Relative humidity inside the vessel for IFSF Drying Test 3 demonstrating the significant relative humidity rebounds that occurred at the end of all IFSF tests.

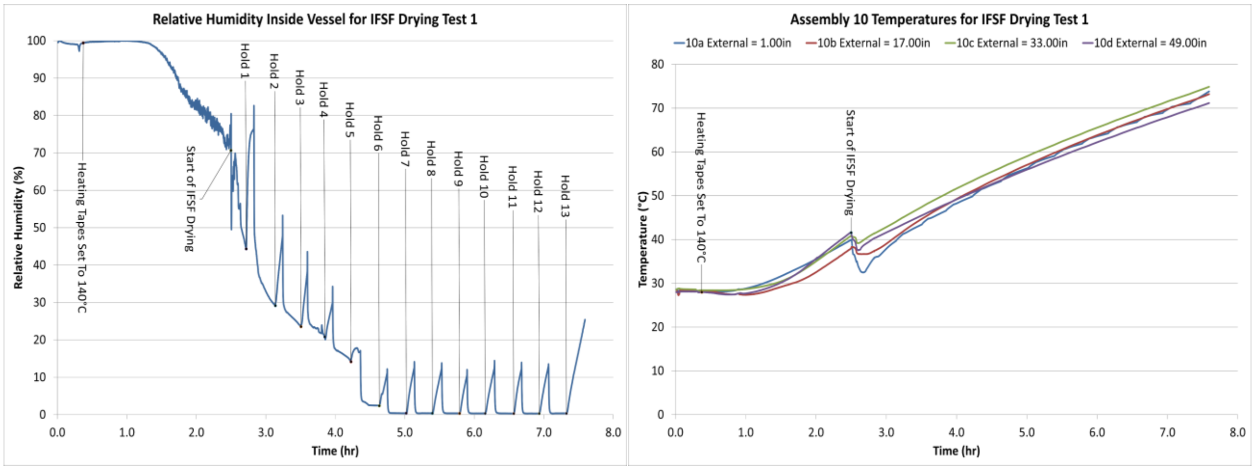

Figure 42. Relative humidity inside the vessel for IFSF Drying Test 1 (left), axial temperatures of Assembly 10 for IFSF Drying Test 1 (right), Assembly 10a's heating rate increases at the 4.25 hour mark.

7. ANALYSIS

7.1 Comparative Mass Loss Behavior

The TGA data provide two means of evaluating sample behavior: overall mass loss (difference in sample weight before and after the TGA run) and rate of mass change with TGA temperature (trend in the TGA curve).

7.1.1 Overall Mass Loss

For each TGA sample, the final value of sample mass loss was divided by the oxide surface area to give the Sample Oxide Mass Loss value in mg/mm^2 (Equation 1). This accounts for the mass loss occurring from the oxide layer, which was only on the surface and not the entire mass of the aluminum sample. Because the samples came from various batches (with potentially differing oxide layer thicknesses), an Average Control Oxide Mass Loss value was calculated for each batch by running TGA tests on several samples from an undried plate and taking the average of all of them (Equation 2). The fractional Oxide Mass Loss Relative to Control was then calculated by dividing the Sample Oxide Mass Loss by the Average Control Oxide Mass Loss for the batch of origin for the sample (Equation 3). The Oxide Mass Loss Relative to Control represents the mass loss that occurs in the oxide layer during TGA. Since the desired value is the mass loss that occurred in the oxide layer during previous drying tests, the Oxide Mass Loss Relative to Control must be subtracted from one to give the fractional Drying Mass Loss Relative to Control (Equation 4:).

Equation 1:

$$Sample\ Oxide\ Mass\ Loss\ \left(\frac{mg}{mm^2}\right) = \frac{Sample\ Mass\ Loss\ (mg)}{Sample\ Surface\ Area\ (mm^2)}$$

Equation 2:

$$Average\ Control\ Oxide\ Mass\ Loss\ \left(\frac{\mathrm{mg}}{\mathrm{mm}^2}\right) = Average\left(\frac{Control\ Oxide\ Mass\ Loss\ (mg)}{Control\ Surface\ Area\ (mm^2)}\right)$$

Equation 3:

$$Oxide\ Mass\ Loss\ Relative\ to\ Control\ = \left(\frac{Sample\ Oxide\ Mass\ Loss}{Average\ Control\ Oxide\ Mass\ Loss}\right)$$

Equation 4:

$$Drying\ Mass\ Loss\ Relative\ to\ Control\ = \left(1 - \frac{Sample\ Oxide\ Mass\ Loss}{Average\ Control\ Oxide\ Mass\ Loss}\right)$$

Scatter plots of all results from TGA can be seen in Figure 43. It displays a clear relationship between mass loss and drying temperature. For improved readability, Figure 44 shows only the FHD TGA results over the higher temperature range, and Figure 45 shows only the vacuum-drying results over the lower temperature range. The drying temperature in the scatter plots represents the maximum temperature achieved during the tests. In Figure 43 and Figure 45, negative fractional mass loss values represent cases where the sample's post-drying TGA mass loss was greater than the average undried control sample, which was attributable to the variation of oxide loading within a batch and negligible dehydroxylation of the corrosion layer during that drying test. These negative values only occurred during vacuum-drying tests, which yielded consistently lower fractional mass losses across all samples, showing that vacuum drying at a low temperature is inadequate to remove chemisorbed water from oxide surfaces of the assembly.

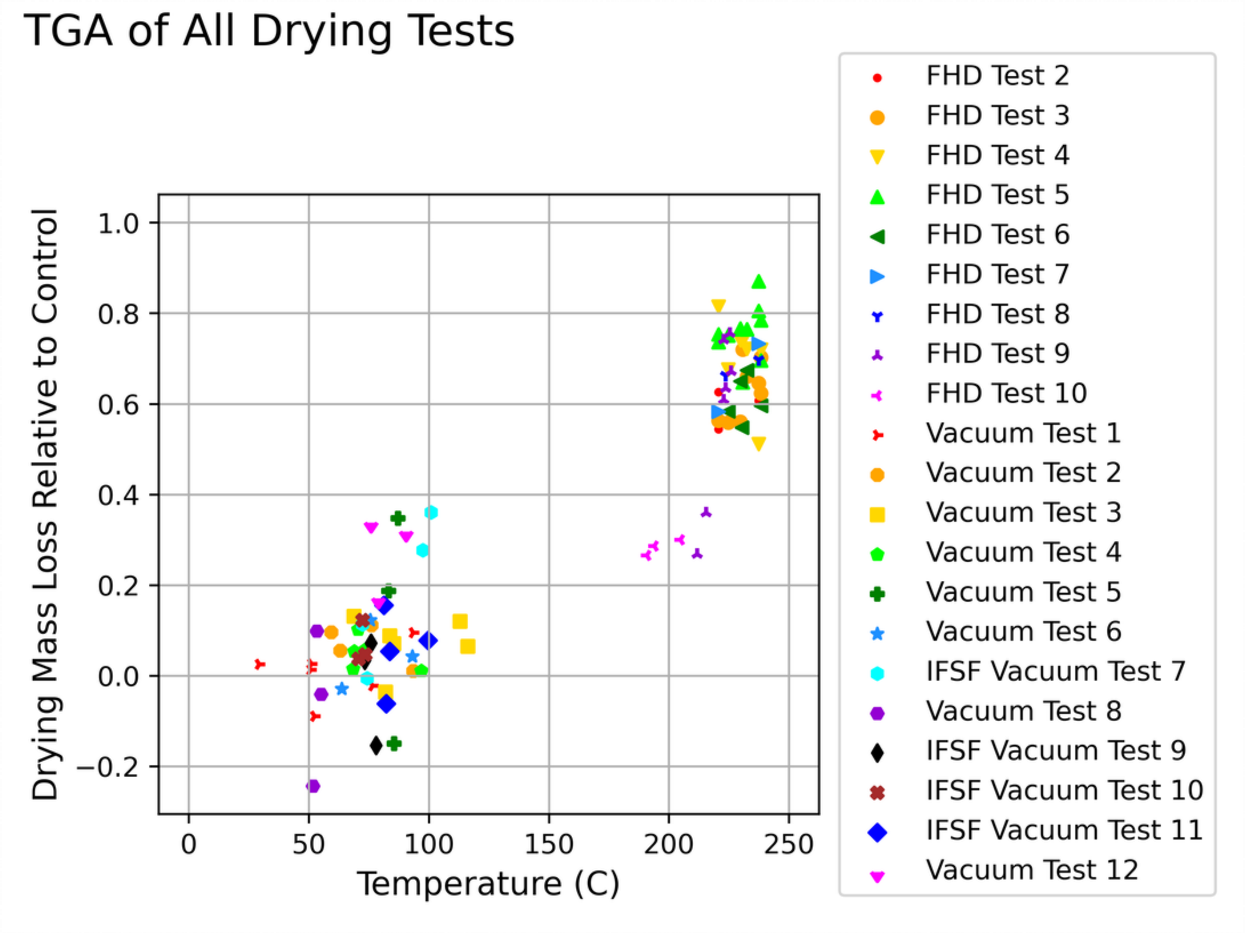

Figure 43. Scatter plot of TGA results versus drying temperature for all drying tests.

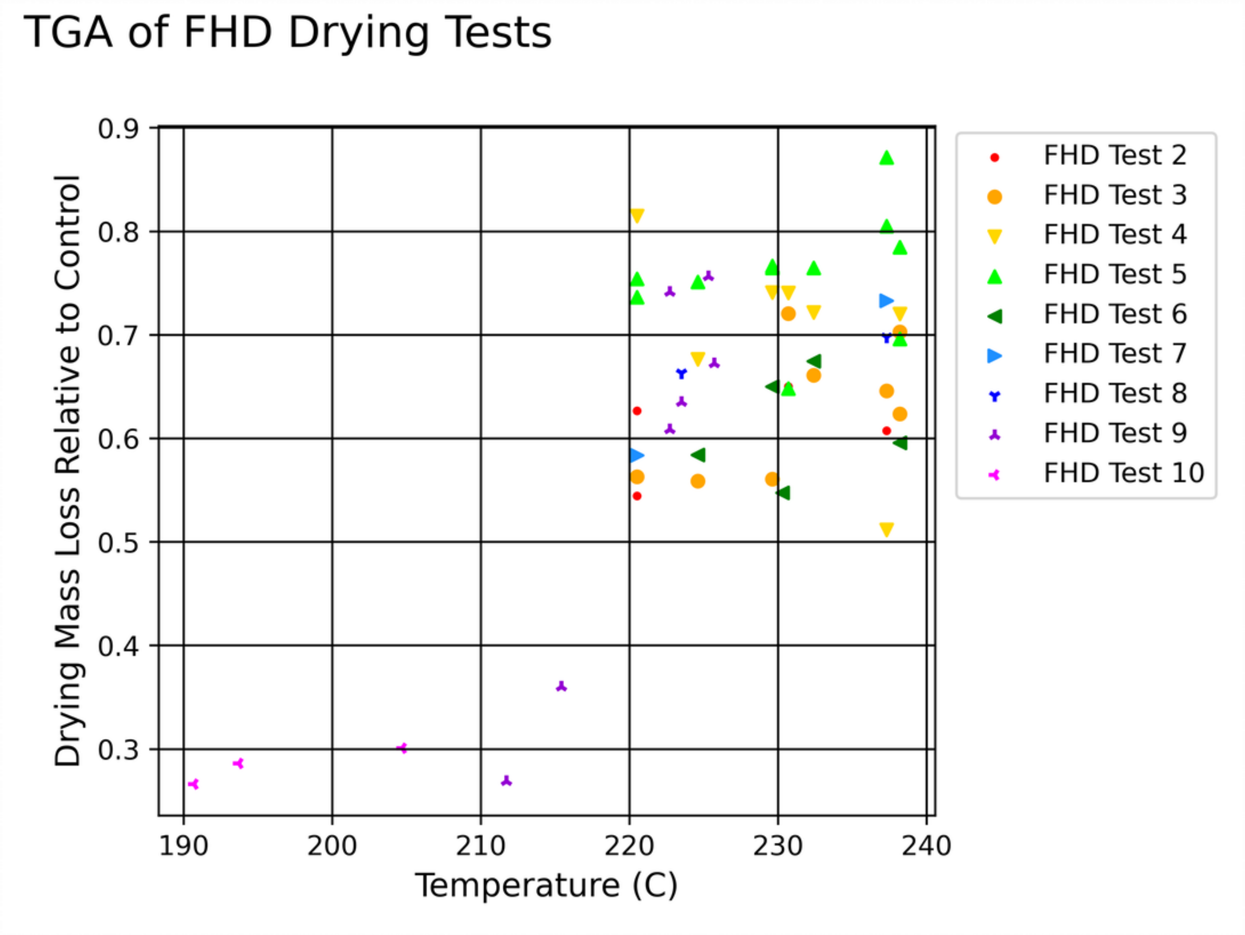

Figure 44. Scatter plot of TGA results with drying temperature FHD tests.

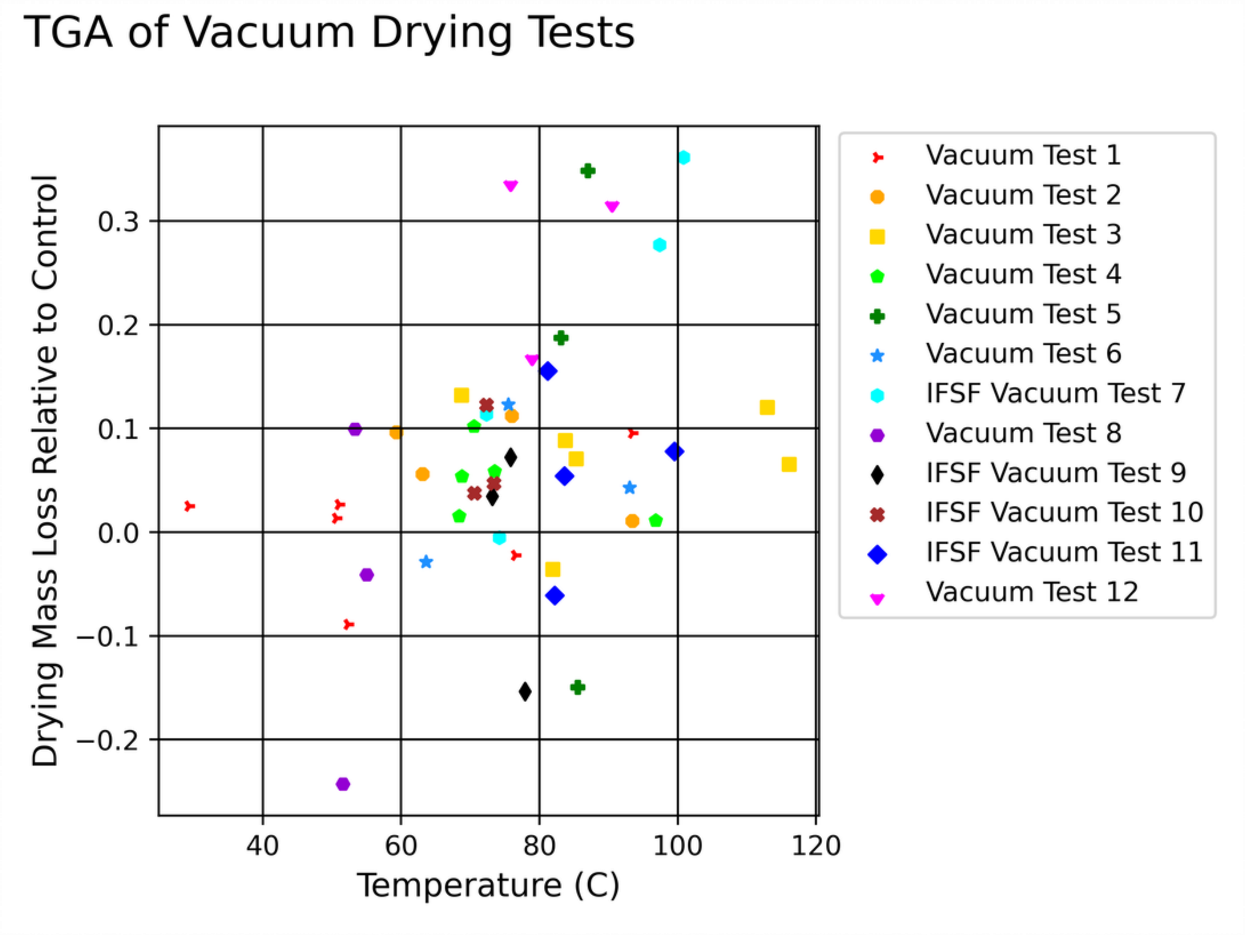

Figure 45. Scatter plot of TGA results with drying temperature vacuum tests.

Figure 46 plots mass loss against test duration rather than temperature and shows the effect time had on the drying process across all tests. While drying time was a factor in mass loss, drying temperature had a far greater effect. Figure 46 appears to show a small correlation between increasing mass loss and increasing test duration for FHD tests but no apparent trend for vacuum-drying tests.

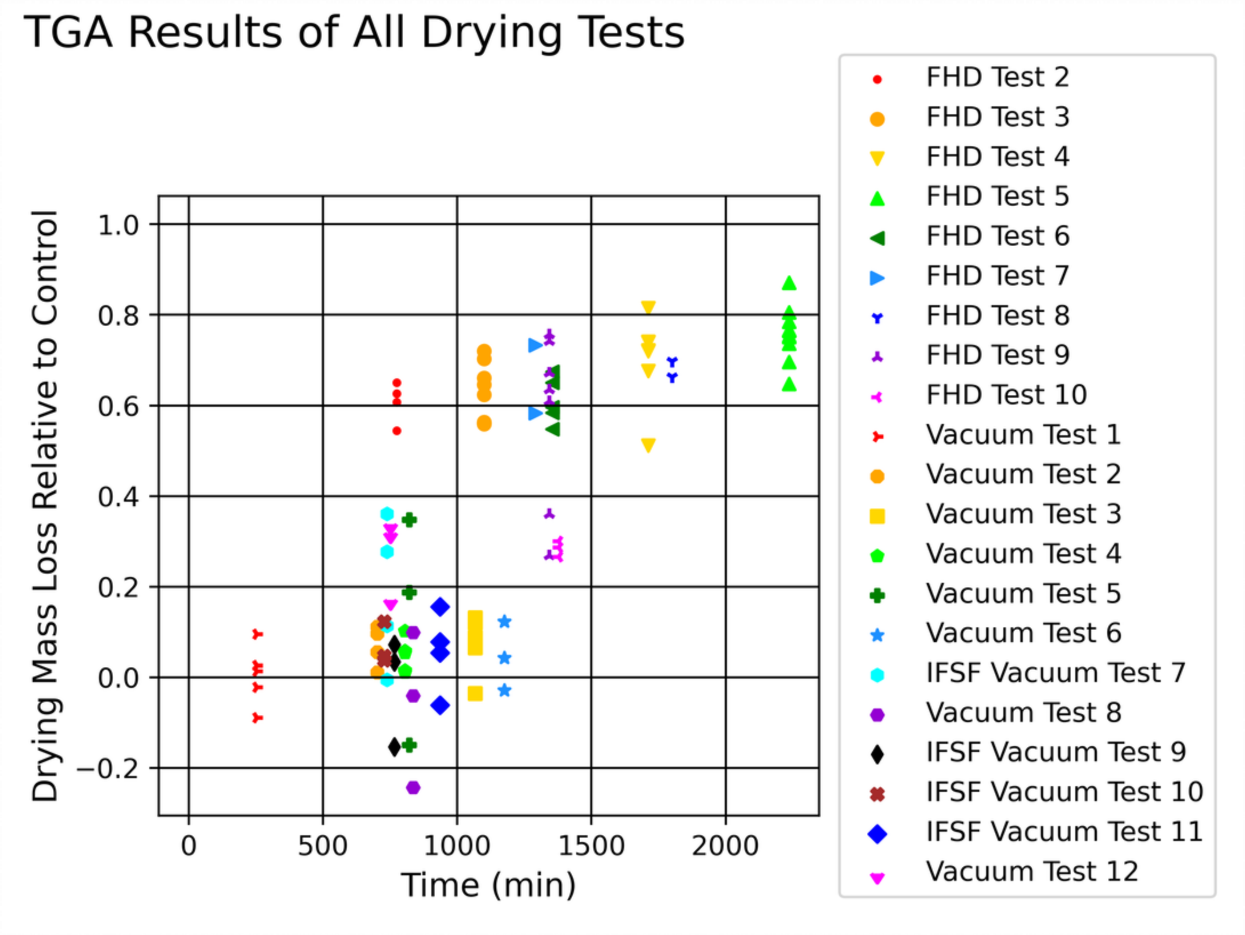

Figure 46. Scatter plot of TGA results versus drying time for all drying tests.

The FHD tests showed another trend, which involved a dramatic increase in mass loss when dried above 220°C. Examination of Figure 46 indicates that FHD Tests 6, 7, 9, and 10 had nearly the same (~1,300 minute) duration, while Figure 44 clearly shows the split in mass loss depending on the temperature reached. This trend can most notably be seen in FHD Test 9 (Figure 47). FHD Test 9 had assemblies dried both above and below 220°C.

Table 5 shows the drying temperatures of the various assemblies in FHD Test 9. Assemblies 1A and 1C were dried below 220°C, producing an observed mass loss of less than 40%, while the remaining assemblies were dried above 220°C, producing an observed mass loss greater than 60%. The relatively small difference in drying temperature, 7°C, enabled a mass loss of an additional 20% over the same FHD drying test run. This dramatic increase in mass loss with a small change in temperature is typically an indication of a phase change that occurs at that temperature and is consistent with the behavior independently reported from the TGA study of an ~8 µm–thick adherent film of bayerite grown on an Al-6061 coupon.[29] Interestingly, as shown in Table 5, the heated assembly, Assembly 4, produces a greater observed mass loss than other assemblies even when those assemblies achieve comparable or higher temperatures. This additional mass loss can be attributed to the fact that the temperatures given represent the maximum temperature achieved during the test. Upon closer inspection, Assembly 10 had a higher maximum temperature, while Assembly 4 held a higher temperature for a longer period throughout the duration of the test.

Another interesting phenomenon that occurred throughout the analysis process was the loss of oxide (spallation of powder off the surface) over time. As seen in Figure 48 the longer the duration of time between TGA tests, the less mass loss that occurs in the control samples. Figure 46 only shows a weak relationship between drying duration and mass loss. Also, the small coupons used for the development of the corrosion growth and sample handling protocols showed no indication of oxide decomposition over a period of six weeks after removal from the corrosion bath, regardless of being stored in a sealed bag, with or without bulk water added, or in open air at INL. Negligible changes in coupon mass were measured before and after this six-week period. (Wet coupons were exposed to ambient laboratory air for a few hours to attain stable weight measurement.) However, the oxide powder on the surface of all test and control plate samples was delicate and seemed to become less adherent, rather than susceptible to decomposition, over time. The outer or upper most oxide layer on the surface of all samples rubbed off with relative ease throughout the handling process. Consequently, oxide powder was observed to accumulate in the sample bags over time. This loss of oxide layer results in greater error for longer times between measurement of control samples and evaluation of dried samples in the TGA. This error was mitigated by evaluating control samples as close to the same time as the dried (tested) samples from that same batch.

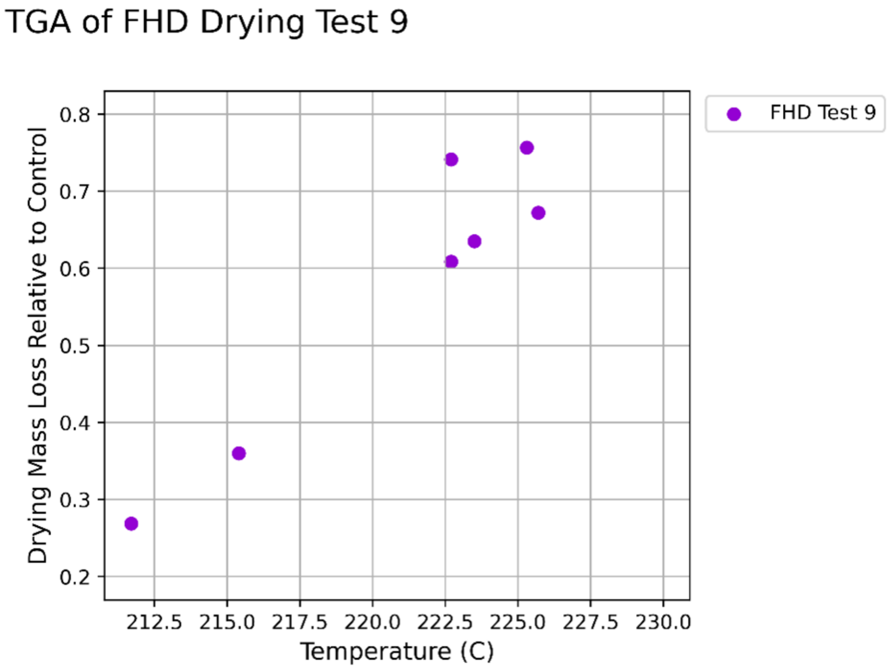

Figure 47. Scatter plot of TGA results with drying temperature for FHD Test 9.

Table 5. FHD Test 9 assembly locations with relative percent mass loss in order of increasing maximum drying temperature.

FHD Test 9		
Assembly	Maximum Drying Temperature (°C)	% Mass Loss
1C	211.70	26.90%
1A	215.40	36.03%
4C	222.70	74.15%
7A	223.50	63.52%

4B	225.30	75.66%
10A	225.70	67.23%

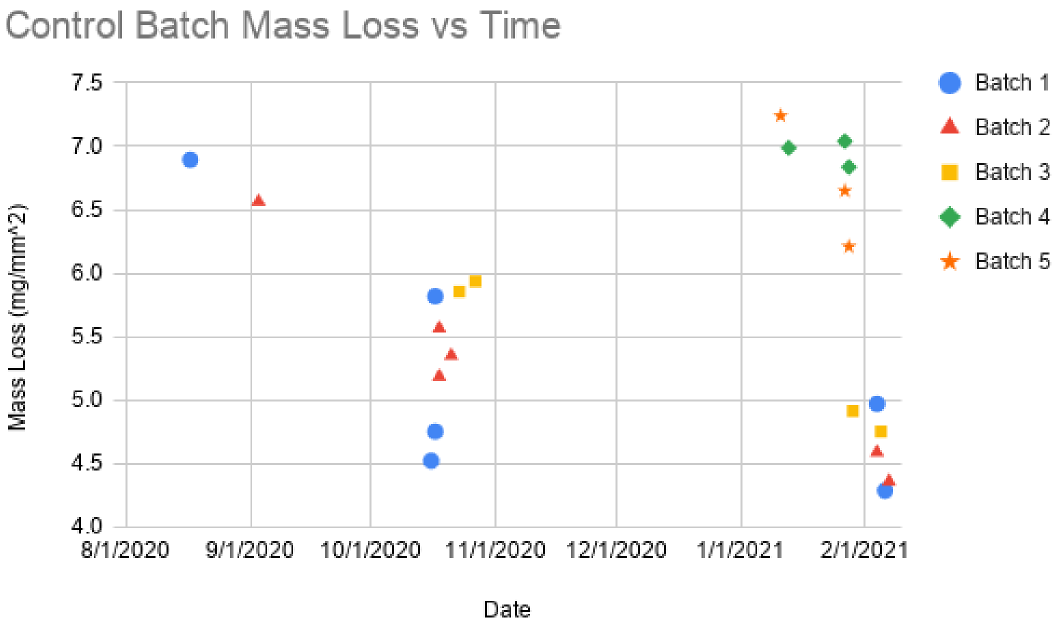

Figure 48. Scatter plot of TGA control samples versus test date.

7.1.2 Rate of Mass Change with TGA Temperature

Figure 49 shows the TGA curve of a Batch 2 control sample with an onset value of 222.8°C. This onset value is indicative of a phase change that occurs just above 220°C. Figure 50 shows the TGA curve for a sample that achieved a maximum temperature of 193.7°C during an FHD test. The FHD sample shows an onset value of 226.7°C, with a similar TGA graph to the control sample. This is because the FHD test never reached a temperature above 220°C at the Assembly 1A sample location, so this phase change occurred during the TGA run not during drying. By comparison, Figure 51 shows the TGA curve from a sample that achieved 225.3°C during an FHD test. This curve does not have an onset value, which indicates that no phase change occurs during TGA, so the phase change must have occurred during the FHD test. Figure 52 and Figure 53 show the TGA curve for vacuum tests, which were all similar to the control because none of the tests had temperatures exceeding 220°C. The only notable difference between the TGA curves in Figure 52 and Figure 53 is the use of a correction file in Figure 53. The correction file has no effect on the onset value but only affects the general trend in the latter half of the curve.

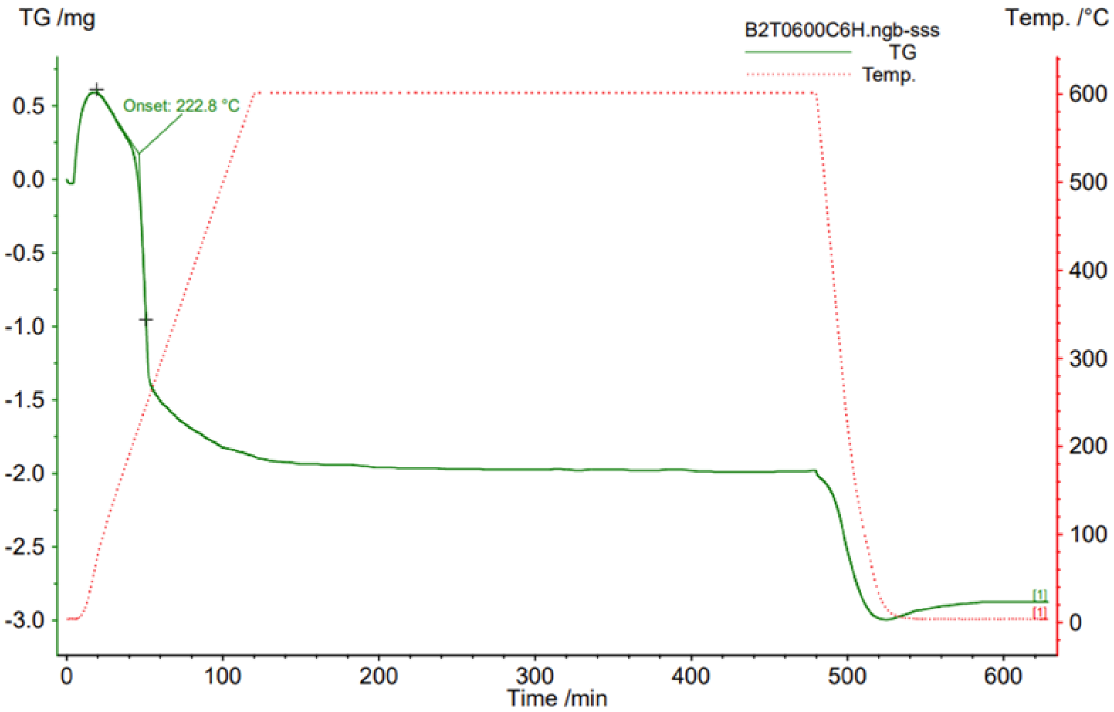

Figure 49. TGA curve of a Batch 2 Control Sample (no correction file).

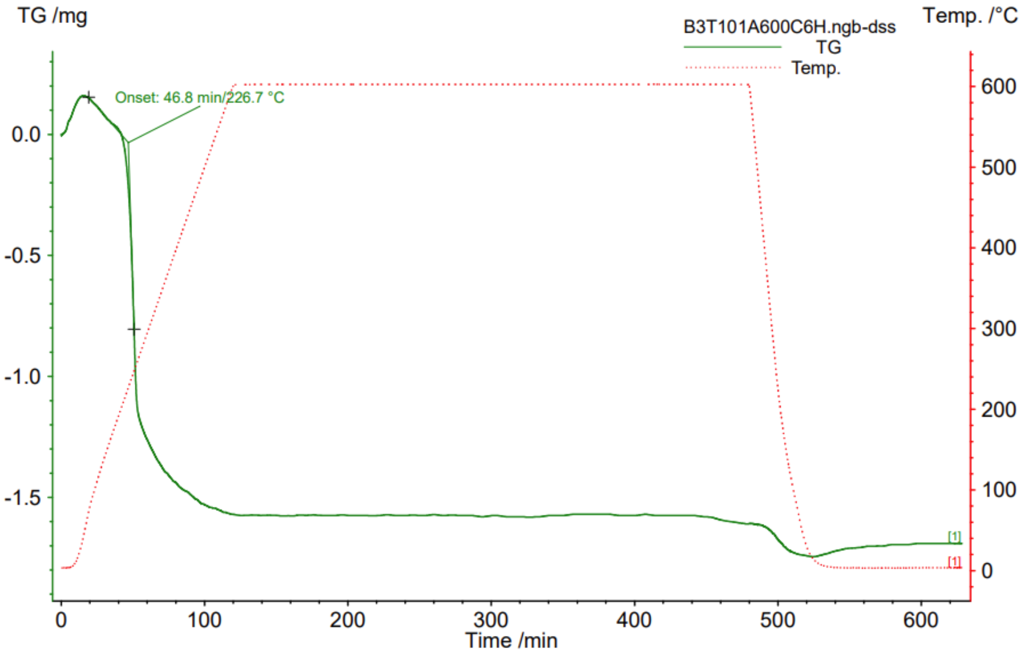

Figure 50. TGA curve of FHD Test 10 1A dried at 193.7°C (correction file.).

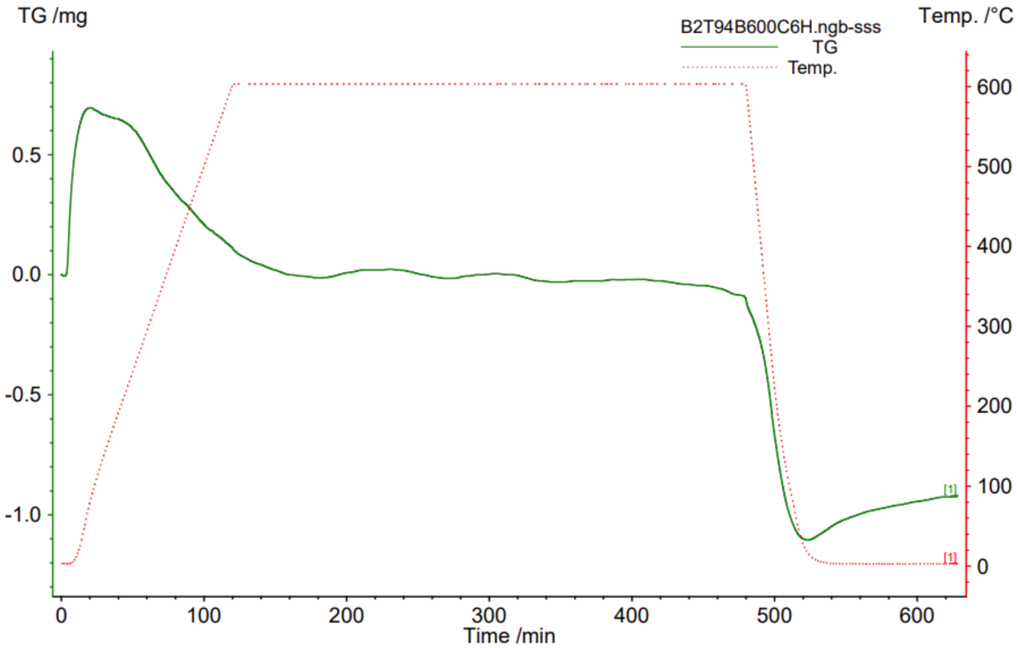

Figure 51. TGA curve of FHD Test 9 4B dried at 225.3°C (no correction file).

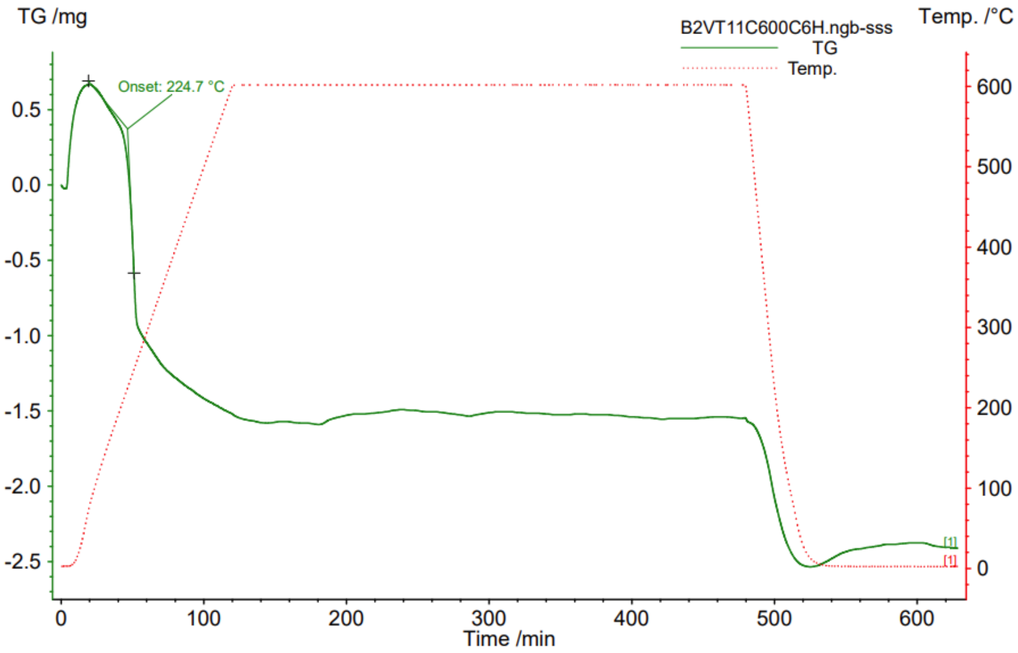

Figure 52. TGA curve of Vacuum Test 9 1B dried at 75.8°C (no correction file).

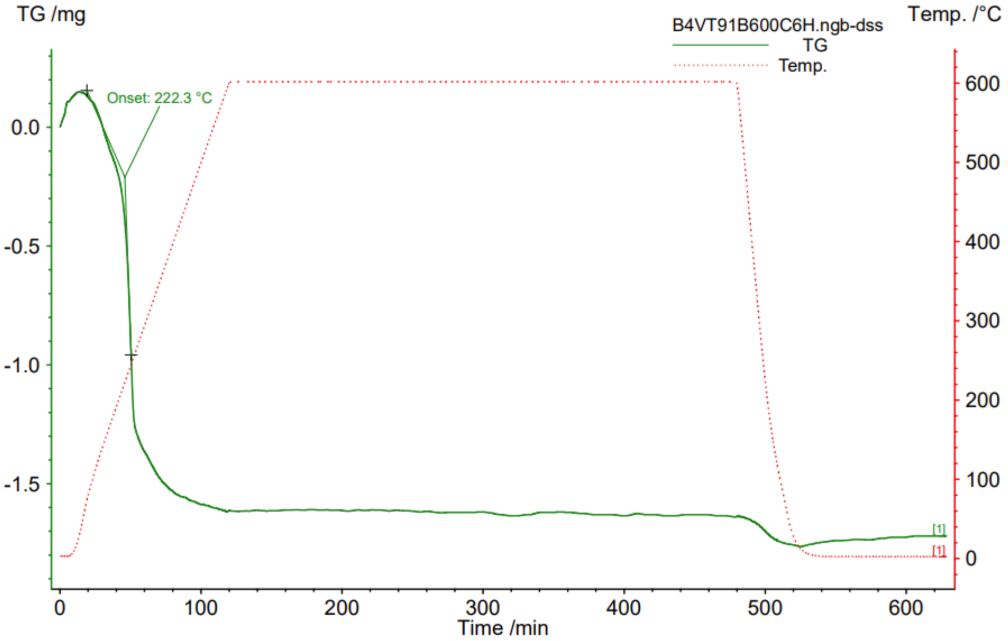

Figure 53. TGA curve of Vacuum Test 11 1C dried at 83.6°C (correction file).

7.2 SEM Images

The top images of Figure 54 show representative surfaces for an undried control sample from corrosion surrogate Batch 2 at 5k× magnification, while the bottom images show corresponding structures from a sample that underwent drying at temperatures below 220°C. The oxide layer's dominant crystal phase was expected to be bayerite, since all samples underwent corrosion in water at temperatures below 100°C (~20°C).[45] The bayerite content was also confirmed for samples of the first corrosion batches by x-ray diffraction at INL. Negligible change in the surface composition and crystal structure was observed for all samples that underwent drying at temperatures lower than 220°C. The images at the left of Figure 54 show typical areas of individual randomly oriented crystal structures, while the images at the right show bayerite somatoid clusters that are common throughout the surface of samples that are undried or dried under 220°C.

Figure 55 shows crystal structures at (5k×) on a sample that was dried at 225.3°C. On samples that were dried at temperatures greater than 220°C, the bayerite somatoid clusters began to fuse together, and individual crystals are no longer distinguishable, rather appearing as white splotches. The change in the crystal clusters is a common visual indication that a phase change has occurred in the material between the drying temperatures. This phase change is consistent with the temperature where partial dehydroxilation of bayerite to boehmite occurs.[40]

Figure 56 shows higher magnification views of the same somatoid structures from the top right of Figure 54 and from Figure 55 to make the change more visible. In the left image of Figure 56Figure 56. Comparison of magnified bayerite somatoid clusters (left) and fused bayerite somatoid clusters (right) depending upon drying temperature., individual crystals are very clear and visible, but in the right, the somatoid cluster is fused together, forming an entirely different crystal structure.

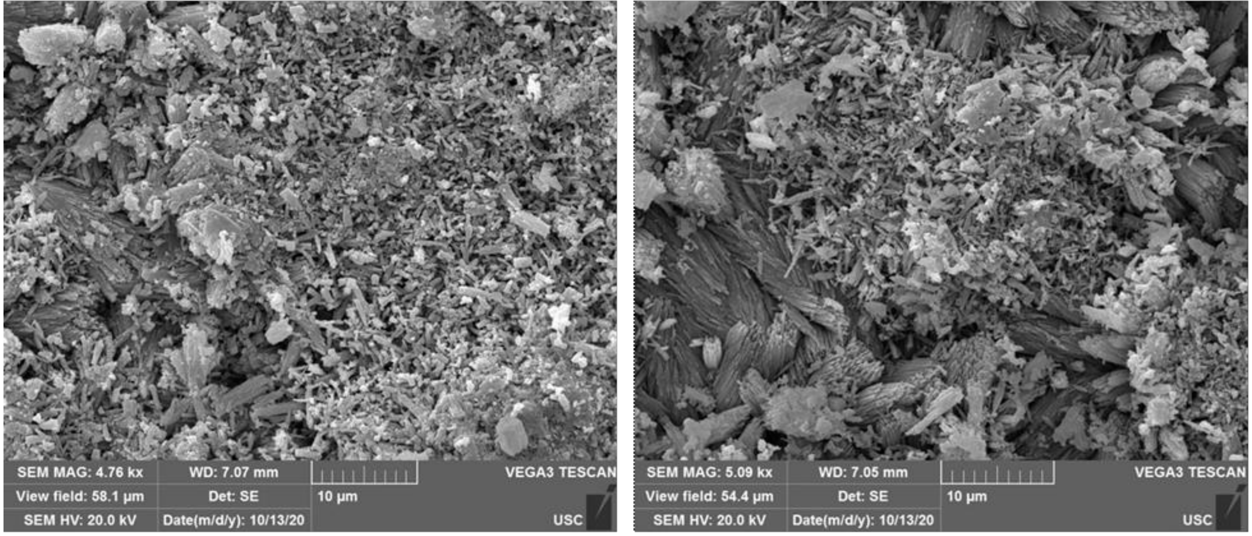

Representative Surface of
Batch 2 Undried Control Sample

Somatoid Cluster on
Batch 2 Undried Control Sample

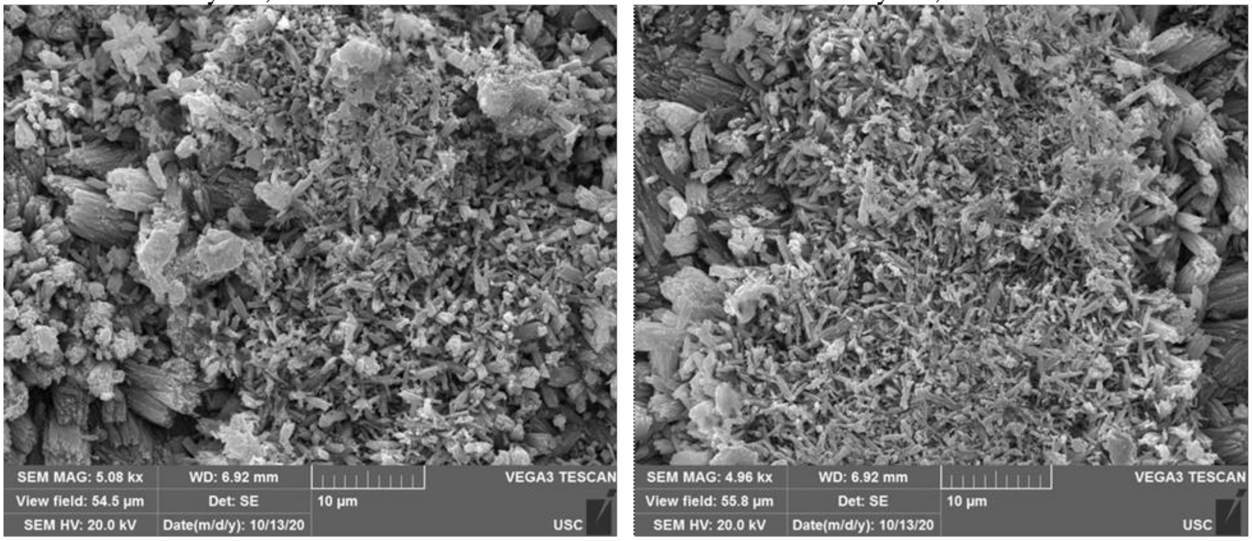

Representative Surface of Batch 2, FHD Test 9,
Assembly 1A, Dried at 215.4°C

Somatoid Cluster on Batch 2, FHD Test 9,
Assembly 1A, Dried at 215.4°C

Figure 54. Representative images of undried control sample and FHD sample dried at 215.4°C.

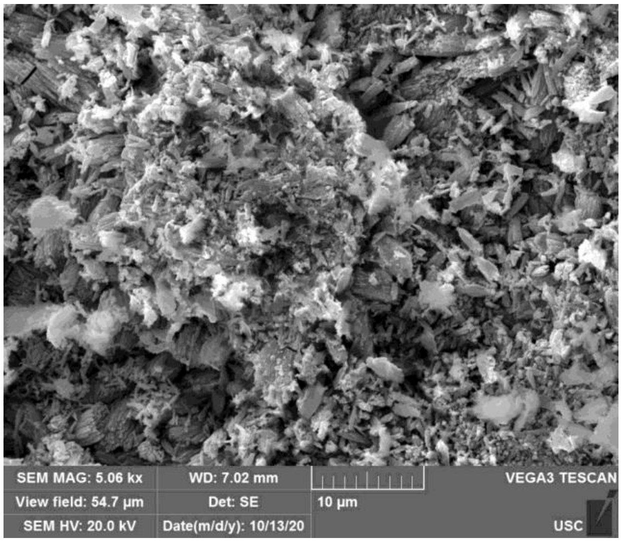

Figure 55. Fused bayerite somatoid cluster on the surface of Batch 2, FHD Test 9, Assembly 4B, dried at 225.3°C.

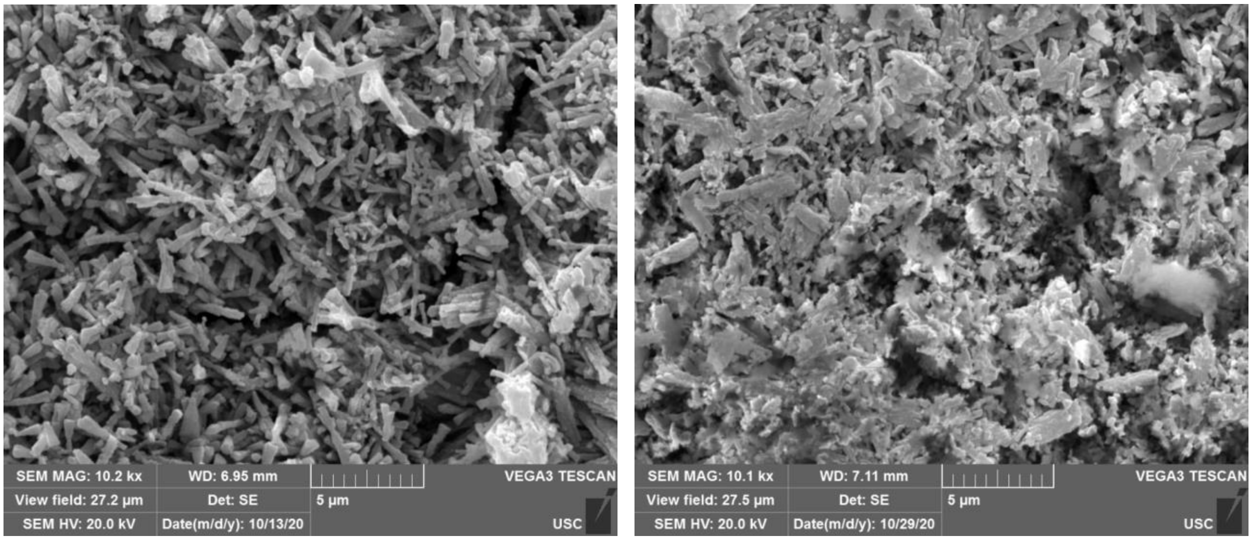
Batch 2, FHD Test 9, Assembly 1A
Dried at 215.4°C

Batch 2, FHD Test 9, Assembly 4B
Dried at 225.3°C

Figure 56. Comparison of magnified bayerite somatoid clusters (left) and fused bayerite somatoid clusters (right) depending upon drying temperature.

8. DRYING PROCESS MODELING [31]

8.1 Drying Process Model Development

8.1.1 The Computational Fluid Dynamics Approach

Since the Reynolds number calculated for the cases ranges from 8,000-60,000 for vacuum drying and from 40,000-68,000 for forced gas dehydration, this lies well within a turbulent flow regime. Rather than fully resolving flows, averaged quantities are used for the turbulence modeling in CFD to represent small scale fluctuations of the flow. A common approach to resolving turbulence in a computational effective way is through the use of Reynolds-Averaged Navier Stokes (RANS) models. These models provide closure relations for the equations for the transport of the main flow quantities. Each solution variable is decomposed into the mean value $\bar{\phi}$, and its fluctuating component ϕ' (Equation 5).

Equation 5:

$$\phi = \bar{\phi} + \phi'$$

For a transient simulation the mean is an ensemble average of flow details occurring at a smaller timescale than that of the CFD time-steps. The modified set of equations utilized for the RANS model are the conservation laws for mass (Equation 6), momentum (Equation 7), and energy (Equation 8). Note, the drying model assumed that λ (the thermal conductivity) and μ (the dynamic viscosity) are constant for the governing equations. For fluids in the model, these equations are as follows [32,33,42]:

Equation 6:

$$\frac{\partial \rho}{\partial t} + \nabla \cdot \rho \bar{\mathbf{v}} = 0$$

Equation 7:

$$\frac{\partial (\rho \bar{\mathbf{v}})}{\partial t} + \nabla \cdot (\rho \bar{\mathbf{v}} \otimes \bar{\mathbf{v}}) = -\nabla \bar{\mathrm{p}} \mathbf{I} + \nabla \cdot (\bar{\mathbf{T}} + \mathbf{T}_{RANS}) + \mathbf{f_b} + \boldsymbol{S}$$

Equation 8:

$$\frac{\partial (\rho \bar{E})}{\partial t} + \nabla \cdot (\rho \bar{\mathrm{E}} \bar{\mathbf{v}}) = -\nabla \cdot \overline{p \mathbf{v}} + \nabla \cdot (\bar{\mathbf{T}} + \mathbf{T}_{RANS}) \bar{\mathbf{v}} - \nabla \cdot \bar{\mathbf{q}} + \mathbf{f_b} \bar{\mathbf{v}} + S_E$$

where the S terms in Equation 7 and Equation 8 represent source terms (i.e., internal generation of momentum or energy), $\bar{E}$ represents the total energy per unit mass, ρ represents the density of the fluid, t represents time, ∇ represents the divergence, $\mathbf{I}$ is the identity tensor, $\bar{p}$ represents the mean static pressure, $\mathrm{f_b}$ is the body force vector – such as due to gravity or centrifugal effects, $\bar{\mathbf{T}}$ represents the mean viscous stress tensor, μ represents the dynamic viscosity, and $\bar{\mathbf{v}}$ represents the flow velocity, $\bar{q}$ is the mean heat flux. In the case of multispecies flows, these equations can be applied to each species individually and summed to find the total within each control volume.

In solid domains, the equations are not solved, and no fluctuations are considered for energy equation. Without a flow regime, the energy equation is simply given by

Equation 9:

$$\rho \frac{\partial E}{\partial t} - \lambda \nabla^2 T + S_E = 0$$

indicating a reliance on conduction to transport energy. In addition to the conservation laws, an equation of state is required to fully describe the system; in this work, the ideal gas law was used for the gaseous phases, and a constant density model was used for solid domains.

The T_{RANS} term in the equation represents the flow fluctuations which are not resolved within RANS turbulence modeling. To solve for this term the Boussinesq approximation used such that

Equation 10:

$$T_{RANS} = 2\mu_t \mathbf{S} - \frac{2}{3}(\mu_t \nabla \cdot \bar{\mathbf{v}})\mathbf{I}$$

Where μ_t is termed the turbulent eddy viscosity, and **S** is the mean strain rate tensor, given by

Equation 11:

$$\mathbf{S} = \frac{1}{2}(\nabla\bar{\mathbf{v}} + \nabla\bar{\mathbf{v}}^T)$$

There are a series of RANS models for estimating the turbulent eddy viscosity developed throughout literature. The realizable k-ϵ turbulence model was used here, as it is empirically fit to boundary layer and channel flow, mixing layer flows with planar and round jets, and backward facing step separated flows over Reynolds numbers of 10,000.[44] This model provides a variety of geometric conditions for which is it valid, which is needed for the complex conditions within the canister geometry. The realizable k-ϵ turbulence model adds two additional transport equations for the turbulent kinetic energy, k, and the turbulent dissipation rate, ϵ. The turbulent kinetic energy is a representation of the kinetic energy associated with eddies in the turbulent flow. The turbulent dissipation rate is the rate at which turbulent kinetic energy is absorbed by breaking larger eddies into smaller eddies. Then, the aforementioned turbulent eddy viscosity as a function of these quantities as

Equation 12:

$$\mu_t = \rho C_\mu f_\mu \frac{k^2}{\epsilon}$$

Where C_μ is a model coefficient equal to 0.09, and f_μ is a dampening function [42]

Equation 13:

$$f_\mu = \frac{1}{C_\mu \left\{4 + \sqrt{6}\cos\left[\frac{1}{3}\cos^{-1}\left(\sqrt{6}\frac{\mathbf{S}^3}{\sqrt{\mathbf{S}:\mathbf{S}}^3}\right)\right] k/\epsilon\sqrt{\mathbf{S}:\mathbf{S}}\right\}}$$

Then the transport equation for the kinetic energy is given by

Equation 14:

$$\frac{\partial}{\partial t}(\rho k) + \nabla \cdot (\rho k \bar{\mathbf{v}}) = \nabla \cdot \left[\left(\mu + \frac{\mu_t}{\sigma_k}\right)\nabla k\right] + P_k - \rho(\epsilon - \epsilon_0)$$

And for the turbulent dissipation rate as

Equation 15:

$$\frac{\partial}{\partial t}(\rho\epsilon) + \nabla\cdot(\rho\epsilon\bar{\mathbf{v}}) = \nabla\cdot\left[\left(\mu+\frac{\mu_t}{\sigma_\epsilon}\right)\nabla\epsilon\right] + \frac{\epsilon}{k}C_{\epsilon1} + P_\epsilon - C_{\epsilon2}\left(\frac{k}{k+\sqrt{\nu\epsilon}}\right)\rho\epsilon^2/k$$

Where, σ_k, σ_ϵ, $C_{\epsilon1}$, $C_{\epsilon2}$ are model coefficients equal to 1.0, 1.3, $max\left(0.43, \frac{\mathbf{S}k/\epsilon}{5+\mathbf{S}k/\epsilon}\right)$, and 1.9, for the realizable k-ϵ model. The production term for the turbulent kinetic energy is given by

Equation 16:

$$P_k = \mu_t S^2 - \frac{2}{3}\rho k\nabla\cdot\bar{\mathbf{v}} - \frac{2}{3}\mu_t(\nabla\cdot\bar{\mathbf{v}})^2 + \frac{\beta\mu_t}{Pr}(\nabla T\cdot\mathbf{g})$$

And the production term for turbulent dissipation is given by

Equation 17:

$$P_\epsilon = \mathbf{S}k + \frac{\beta\mu_t}{Pr}(\nabla T\cdot\mathbf{g})$$

Where Pr is the Prandtl number, and β is the thermal expansion coefficient.

8.1.2 Foundation for Modeling Drying

Traditionally, evaporation and drying have been treated in terms of kinetic theory. Expressions for the molecular flux from one phase to another were accordingly based on a Maxwell-Boltzmann velocity distribution.[34,35] For example, when moving from the liquid phase to the vapor phase, liquid molecules constantly impact the liquid-vapor interface with a velocity consistent with such a distribution, penetrate approximately one mean free path, and absorb into the vapor phase (see Figure 57).[34,35] The expression for this transition to the vapor phase is accordingly:

Equation 18:

$$j^V = P_s(T_I^L)\sqrt{\frac{m}{2\pi k_B T_I^L}}$$

where j^V is the flux going to the vapor phase, T_I^L is the temperature on the liquid side of the interface, m is the molecular mass of the liquid, k_B is the Boltzmann constant, and P_s is the saturation pressure of the vapor (and is a function of the liquid temperature).

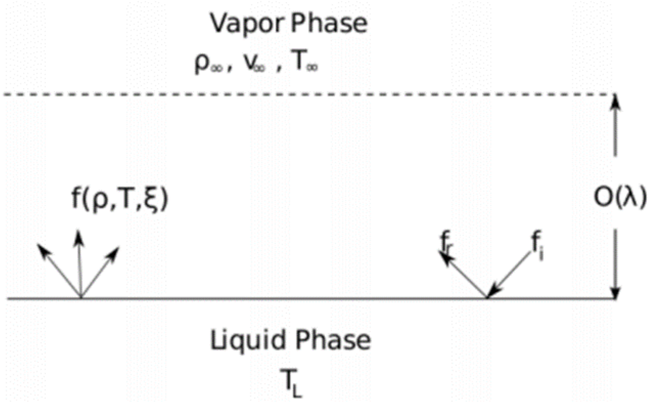

Figure 57. Illustration of molecular kinetics on the liquid side of the interface.[35]

Therefore, evaporation (and condensation) can be considered as the net molecular flux between the liquid and vapor phases, expressed by [34,35]:

Equation 19:

$$j = P_s(T_I^L)\sqrt{\frac{m}{2\pi k_B T_I^L}} - P_V\sqrt{\frac{m}{2\pi k_B T_I^V}}$$

where j is the net flux, T_I^V is the temperature on the vapor side of the interface, P_V is the vapor pressure, m is the mass of a molecule, and k_B is the Boltzmann constant. The first term on the right-hand side corresponds to movement from the liquid phase to the vapor phase, and the second corresponds to movement from the vapor phase to the liquid phase.[34] Accordingly, if j is greater than zero (i.e., net movement from liquid to vapor), evaporation is said to be taking place, and, if j is less than zero, condensation is taking place.

Equation 19 can be further modified by introducing two constants, σ_e and σ_c. These constants represent the fraction of molecules that actually complete the phase change, rather than being reflected back to their original phase, and therefore must have a value between zero and one.[34] The introduction of these gives the classic Hertz-Knudsen relation for evaporation/condensation [34]:

Equation 20:

$$j = \sigma_e P_s(T_I^L)\sqrt{\frac{m}{2\pi k_B T_I^L}} - \sigma_c P_V\sqrt{\frac{m}{2\pi k_B T_I^V}}$$

Two further simplifying assumptions are commonly made when dealing with the Hertz-Knudsen relation. The first is the assumption of thermal equilibrium (that is, $T_I^L = T_I^V$). The second is the equivalence of σ_e and σ_c (that is, $\sigma_e = \sigma_c$).[34] Application of these assumptions gives Equation 21. The determination of the accommodation coefficient σ is a common subject of evaporation studies.

Equation 21:

$$j = \sigma(P_s(T) - P_V)\sqrt{\frac{m}{2\pi k_B T}}$$

Thus, by observation of Equation 21, evaporation (or condensation) at a given temperature is driven by the difference between the saturation pressure (i.e., the maximum vapor the atmosphere can hold) and the actual vapor pressure. If the vapor pressure is greater than the saturation pressure, the system will move toward equilibrium by condensing some of the vapor to the liquid phase. Conversely, if the vapor pressure is less than the saturation pressure, evaporation will take place.

As mentioned previously, an expression for the saturation pressure, typically a polynomial of temperature, is required to complete the Hertz-Knudsen equation. Historically, these relations have had a semi-theoretical basis for any phase transition in the Clausius-Clapeyron equation, when looking at liquid-vapor transitions, the specific form is given by [36]:

Equation 22:

$$\frac{dP_s}{dT} = \frac{\Delta H}{T_K(V_g - V_l)}$$

where ΔH is the heat of vaporization, T is the absolute temperature (in Kelvin), and V_g and V_l are the molecular volume of the gas and liquid phases, respectively. By integrating Equation 22 once and assuming that $V_l \ll V_g$, ΔH is constant, and the vapor is an ideal gas, the following expression is obtained:

Equation 23:

$$\log P_s = A - \frac{B}{T}$$

Note that, while individually these assumptions are highly imperfect, the combination leads to a good approximation because some of the errors cancel out.[36] The most commonly used solution of this form is the Antoine equation which is empirically fit across temperature ranges [36,37]:

Equation 24:

$$\log P_s = A + \frac{B}{T_C + C}$$

where T_C is temperature in degrees Celsius and saturation pressure, P_S is in bar. One suggested set of coefficients for water over a large temperature range is given in Table 6:

Table 6. Antoine equation coefficients for water.[37]

Temperature Range (°C)	A	B	C
0–30	5.40221	1838.675	-31.737
31–60	5.20389	1733.926	-39.485
61–90	5.07680	1659.793	-45.854
71–100	5.08354	1663.125	-45.622
106–200	3.55959	643.748	-198.043

8.1.3 ASNF Drying Models

The geometries described in Section 3 were reproduced in Trelis (Version 16.3.2) and imported into the multiphysics package STAR-CCM+ (Version 13.02.013 & 13.06.012) for use as illustrated in a series of images in Figure 58. They were then subdivided into four domains: an aluminum domain (the surrogate assemblies), a stainless-steel domain (the basket), a boron nitride domain (the heater), and a fluid domain consisting of the remaining volume. The full siphon tube was not meshed, so an interior boundary condition was used in the fluid volume to represent the boundary for the siphon tube.

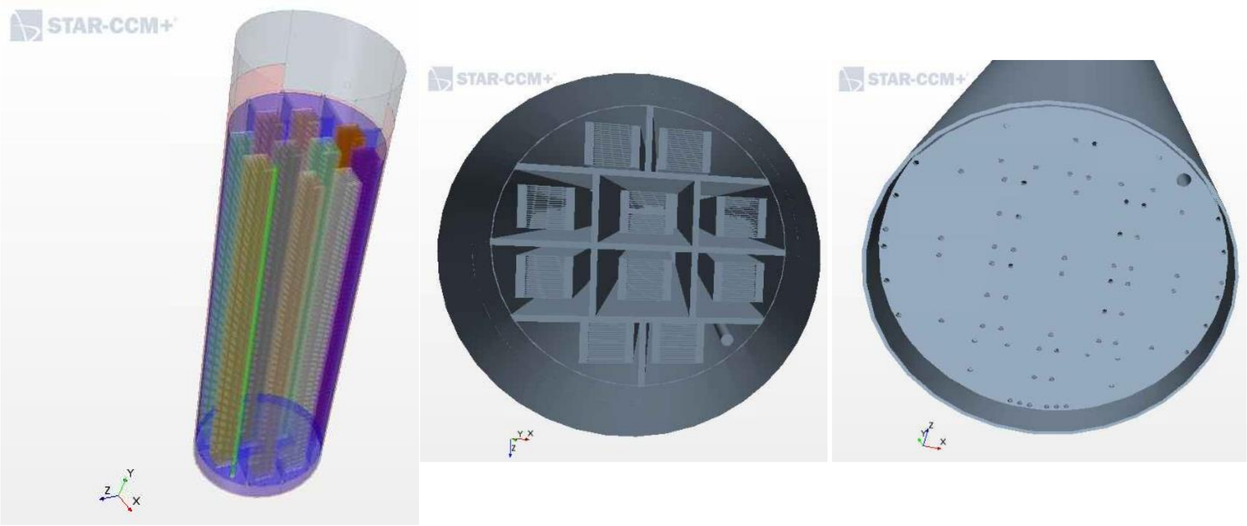

Figure 58. 3D-CAD imported into STAR-CCM+ of the ASNF chamber and assemblies (left), siphon tube and orientation of assemblies inside the basket (middle), and base plate of the basket with the “false-bottom” configuration (right).

The solid domains (aluminum, steel, and boron nitride domains) required only an energy solver and equation of state be specified. The Segregated Solid Energy (see Equation 9) and Constant Density models were chosen. Each domain was assigned the appropriate material properties as given in Appendix C; aluminum and steel were already included in STAR-CCM’s database, while an entry had to be made for boron nitride.

The fluid domain was modeled as a nonreacting, multicomponent gas composed of helium and water vapor. The mass and momentum equations (Equation 6 and Equation 7) were modeled by the Segregated Flow module (this automatically enables the Segregated Species model for the species solutions). The energy equation (Equation 8) was likewise modeled with the Segregated Energy module. The ideal gas law was chosen as the equation of state. An estimate of the Reynolds number found parts of the domain (particularly the false bottom) to occupy the transition region between laminar and turbulent flow. Therefore, a standard k-ε turbulence model (Equation *14* and Equation *15*) was employed for the entire fluid domain in the continua section of STAR-CCM.

8.1.3.1 Inlet and Outlet Boundary Conditions

One of the key parameters for drying via FHD is the recirculation rate. Holtec’s operational experience with their patented FHD process recommended a recirculation rate of at least 50 volume exchanges of the chamber per hour. Given a volume of approximately 177 L and an inlet diameter of ¾ inch (siphon tube), this equates to an inlet velocity of 8.62 m/s (or a mass flow of 3.47 lb He/hr). However, as noted in Section 6, this mass flow rate was increased to approximately 105 lb/hr, equivalent to 260.75 m/s, for the experimental drying tests after observing that lower flow rates could not achieve inlet gas temperatures of 220–260°C. This inlet gas was considered to be pure helium (that is, 0% water vapor) for the entirety of the FHD simulations. Inlet gas temperature data and boron nitride (nichrome wire) heater power output collected from each drying test was directly imported into STAR-CCM as input tables. During vacuum processes, the inlet velocity and gas temperature condition was removed, and the inlet was treated as a solid surface. Lastly, for the $k - \epsilon$ turbulence model, the viscosity ratio, defined as the ratio between the eddy viscosity μ_t of Equation 12 and the general flow viscosity, was left on the default value of 10.

In general, for FHD, the outlet velocity was set to match that of the inlet, −260.75 m/s (with a reversed sign, to signify gases leaving the domain); no specific temperature or species conditions were set. For vacuum drying, a pressure outlet condition was used to drive the evacuation. The original approach called for the specified pressure to be given as a function of time derived by curve-fitting pressure data from vacuum-drying tests performed at UofSC's Used Fuel Drying lab.[38] The original expression derived from this study is discussed in Nate Cooper's thesis.[31] The evacuation expression was eventually abandoned as modifications were made to the model to set the outlet condition to the raw pressure data collected during the vacuum-drying tests discussed in Section 6. This method allowed for complete accuracy in pressure and was viable as system pressure is a known value during commercial fuel drying. Initial vacuum-drying models consisted of only pulling vacuum from the siphon tube. However, a 1-inlet – 2-outlet model was derived, where the inlet was defined as a wall boundary condition adjacent to the vent port to allow a vacuum to be pulled from both the siphon tube and vent port, mimicking the vacuum-drying process utilized during experimental tests. Both outlets (siphon tube and vent port) were defined by the chamber pressure data collected from the experimental drying tests, and the inlet was left as a solid surface.

8.1.3.2 Chamber Wall Boundary Conditions

In addition to the typical no-slip conditions, a convective boundary condition with an assumed ambient temperature of 300 K was applied to the external chamber surfaces that were not in contact with the heating tapes (i.e., the lid, chamber bottom, and upper section of the chamber where the instrumentation and vacuum ports were located). To determine an effective heat transfer coefficient, a heat transfer circuit was set up using the materials previously mentioned in Section 8.1.3.1 (see Appendix C for properties). Thermal radiation is present during vacuum drying and FHD, but it was deemed to have little impact compared to heat transferred by convection; when tested with the surface-to-surface radiation solver in Star-CCM+, this had less than a 1°C impact on the solution, but caused significant increases in computational time.

In the schematic (Figure 59), the thermal resistances, R_i, are given by $R_1 = \frac{1}{h_{amb}}$, $R_2 = \frac{x_1}{k_{ins}}$, $R_3 = \frac{x_2}{k_{st}}$, and $R_4 = \frac{1}{h_{He}}$, where x_1 and x_2 are the thickness of the insulation and the steel, respectively. Thus, the effective heat transfer coefficient h_{eff} is given by:

Equation 25:

$$\frac{1}{h_{eff}} = \frac{1}{h_{amb}} + \frac{x_1}{k_{ins}} + \frac{x_2}{k_{st}} + \frac{1}{h_{He}}$$

Values for k_{st} and k_{ins} were taken to be 15.1 W/m-K and 0.038 W/m-K, respectively.[32] Although helium is part of the fluid domain in the simulation, the helium heat transfer coefficient was included in the thermal resistance because the mesh was too coarse at the wall boundary region to capture the convection near the wall. The constants h_{He} and h_{amb} were each assumed to be 10 W/m^2-K, at the lower end of estimations for heat transfer coefficients for gases, though this assumption may be revisited later.[32] This was assumed to be valid within the container, as the outer basket wall confines most of the flow in the FHD simulations to remain in the basket, and the small gap between the basket and the canister maintains velocities under 1 m/s. The h_{amb} term could be decreased to a value more in line with natural convection heat loss, however, little emphasis on determining the correct gas-to-solid heat transfer coefficient was deemed necessary for tests, because of the low thermal conductivity and thickness of the insulation, Equation 25 is dominated by the second term. The value of h_{eff} is thus found to be 0.453 W/m^2-K.

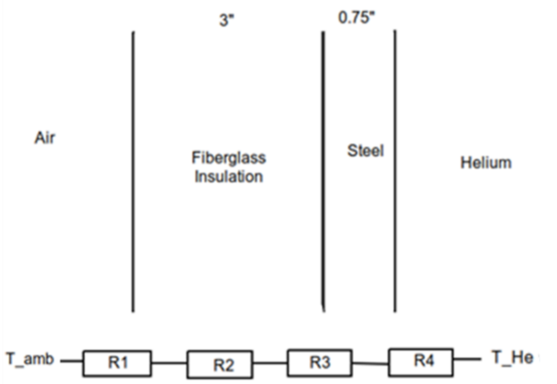

Figure 59. Heat transfer circuit for the experimental drying test chamber walls.

In follow on tests, heating tapes were applied during drying tests to achieve various constant wall temperatures, as previously described in Section 6. Five tapes were applied to the chamber wall with each having a maximum rated output of 627 W at 300°C. For FHD, when their temperature was set to 260°C, each tape had a resulting power output of 543.4 W for a total of 2173.6 W. When distributed over the surface area of the chamber walls (not including the ceiling and floor; these have no tape applied) of 2.335 m^2, a heat flux of 930 W/m^2 is calculated. However, from the model standpoint for the boundary of heated walls, it was found to be more effective to increase the ambient temperature in the model from 300 K to the heating tapes' temperature setpoint, and the heat transfer coefficients for the insulation and air were ignored to derive an effective heat transfer coefficient from the tapes to through the steel to the helium thermal boundary layer. Although the helium term will likely be much greater, the h_{He} was still assumed to be 10 W/m^2-K for simplicity.[31] As a result, the effective heat transfer coefficient was derived to be 9.875 W/m^2-K for the FHD model. Since water vapor was the dominate gas for most of each vacuum-drying test, the helium term was replaced with a water vapor heat transfer coefficient value of 0.399 W/m^2-K derived from thermophysical properties for water vapor at sub-atmospheric pressures.[39] The wall boundary conditions used here to simulate the heating tapes were updated from the previous models discussed in Nate Cooper's thesis.[31]

8.1.3.3 Vaporization Mass Flux

The thermal impact of vaporization was not included in the model as the derived evaporative heat lost in FHD tests were assumed to not affect the overall heat load. It was first assumed that the water evaporation from the corrosion layer of the fuel has the same latent heat of water, $\Delta H_{f,g} = 2260$ kJ/kg. Then a simple heat balance ratio of latent heat against heat provided by the FHD gas and walls was constructed as

Equation 26:

$$\frac{\dot{m}_{evap}\Delta H_{f,g}}{\dot{m}_{He}c_{p,He}\Delta T_{in,out} + Q_{wall}}$$

Using this heat balance ratio, the total heat loss due to evaporation in FHD tests was calculated to be only 0.4%, which should be negligible with regards to the simulations completed. However, when utilizing Equation *26* for the vacuum drying cases, this yielded a ratio of 10.5%. The assumption of ignoring this heat loss for vacuum drying may need to be revisited in future studies.

Although some vacuum-drying tests operated at lower heating tape temperature setpoints, there was a marginal increase in the thermal impact of vaporization. As previously described, the Hertz-Knudsen relation (Equation 21) is a commonly used expression for modeling evaporation (and condensation) mass fluxes. There is no published literature using this relation for the thermal decomposition of an oxyhydroxide. However, repurposing TGA data as a foundation for expressing the thermal decomposition allowed the use of the Hertz-Knudsen relation. This relation is not a perfect representation for decomposition and dehydration of oxyhydroxides from a thin layer, but the relation is a reasonable approximation for the drying models given the complexity in geometry of the vessel, basket, and fuel assemblies. The primary weakness of the relation is the need to supply a value for the accommodation coefficient σ, which is typically fitted to experimental data. In the present case, a study in which a series of TGA tests were conducted to characterize mass loss and phase change in bulk gibbsite samples was repurposed to develop an empirical relation for the mass flux of water from bulk gibbsite during drying as a function of temperature.[40] In each test, the samples were heated at a constant rate of 5ºC/minute to the maximum test temperature and held at that temperature for several hours; a summary of the maximum temperatures and hold times is found in the test matrix of Table 7. A plot of the results of a typical test, corrected for buoyancy effects, is pictured in Figure 60. Note that the term "mass loss" in this case indicates the absolute, total mass loss relative to the initial total mass of each sample.

Table 7. Aluminum coupon TGA test matrix.[40]

Test	Area (cm^2)	Initial Mass (mg)	Final Mass (mg)	Mass Loss (mg)	Max Temperature (ºC)	Time at Max Temp. (hr)
RT0226a	2.28	956.52	954.36	2.16	500	6
RT0226b	2.06	859.22	857.48	1.74	260	4
RT0226c	2.64	1115.50	1104.25	11.25	500	6
RT0226d	2.15	906.00	903.95	2.05	500	6
RT0226e	2.21	918.69	917.56	1.13	200	24
RT0226f	2.06	873.55	872.32	1.23	220	24
RT0226g	1.07	455.16	453.93	0.97	500	4
RT0226h	3.61	1563.58	1560.05	3.53	500	4
RT0226i	0.789	319.85	319.10	0.75	500	6
RT0226j	1.06	451.28	450.32	0.96	500	6

Despite the buoyancy corrections, a small mass growth region was still observed, typically ending at around 55ºC; this was neglected during the curve fitting. To maximize the temperature range of the derived relations, work focused on tests RT0226a, c, d, g, i, and j (maximum temperature of 500ºC). The valid temperature range for the empirical relations is therefore 55ºC to 500ºC. In addition, because very little mass loss was observed during the hold times, only the first two hundred data points of the constant temperature part of the test were considered. Figure 60 shows a plot of this refined data set. There are three clear regions in the mass loss data: Region 1, from 55ºC (start of the data) to 220ºC (onset of bayerite decomposition); Region 2, from 220ºC to 260ºC; and Region 3, from 260ºC to 500ºC (maximum temperature). The data for each test was accordingly split into three different subsets, and each was fit with its own empirical relation.

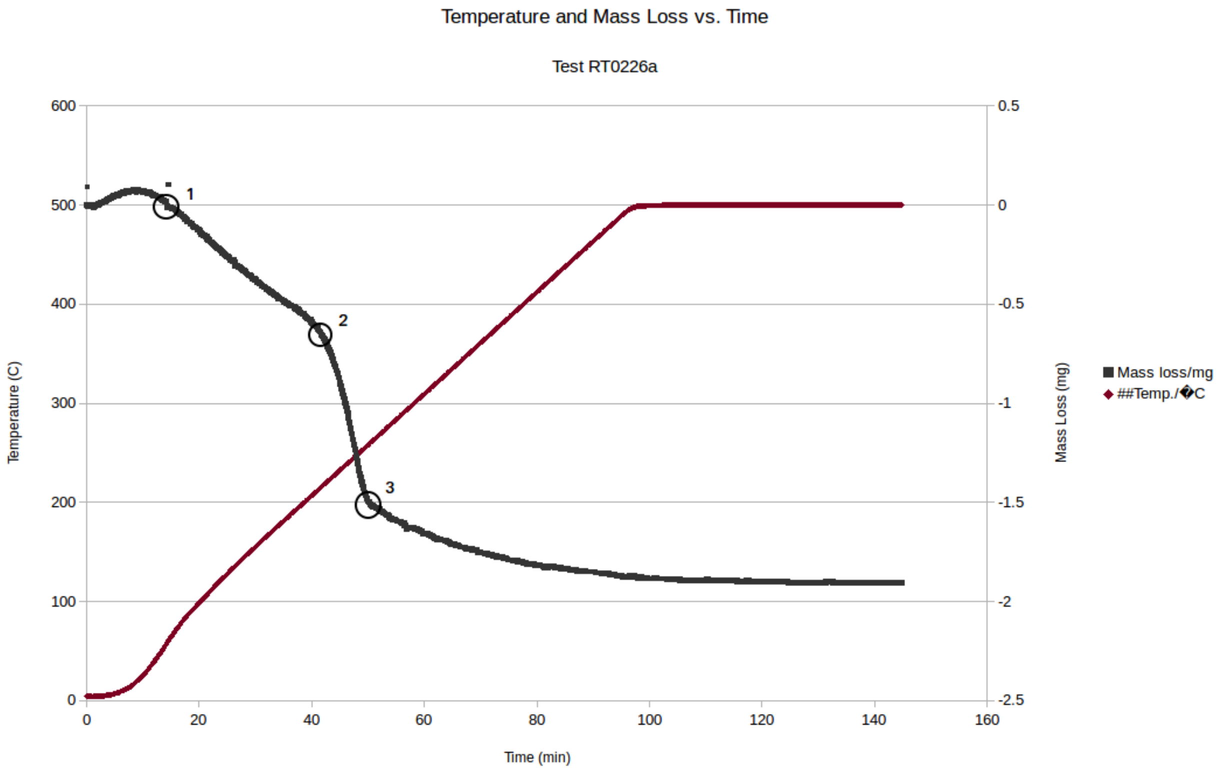

Figure 60. Typical mass loss curve of an aluminum coupon.

In each region, the total remaining water content was modeled as a linear function of temperature (in kelvin):

Equation 27:

$$m = m_0 + \Delta m = aT + b$$

where m is the instantaneous mass, m_0 is the initial water content, Δm is the measured mass loss, and T is the instantaneous temperature. By differentiating Equation 27 with respect to time and dividing by the area of the sample, the instantaneous mass flux is found for each region as:

Equation 28:

$$\dot{m}'' = \frac{a}{A}\frac{dT}{dt}$$

The accommodation coefficient σ in the Hertz-Knudsen relation can be found as a function of temperature and pressure by setting Equation 28 equal to the Hertz-Knudsen relation (Equation 21) and rearranging to give:

Equation 29:

$$\sigma = \frac{a_n}{A(P_s(T) - P_v)}\left(\frac{M}{2\pi RT}\right)^{-\frac{1}{2}}\frac{dT}{dt}$$

where A is the area, $P_s(T)$ is the saturation pressure as a function of temperature, P_v is the vapor pressure, M is the molecular mass, R is the ideal gas constant, and T is the temperature.

Three average accommodation coefficients were obtained for the three temperature regions previously mentioned to prevent a single measurement determining the accommodation coefficient. The curve fitting results for the coefficients in Equation 27 are summarized in Table 8. When plotted, the values for mass flux as computed by Equation 28 (see **Error! Reference source not found.**) cluster together in Regions 1 and 2, implying a constant mass flux consistent with the roughly linear nature of those regions. Across all six tests, the average mass flux in is -0.01793 mg/cm^2 s in Region 1 and is -0.08467 mg/cm^2 s in Region 2. The mass flux in Region 3 has an average of -0.007114 mg/cm^2 s prior to the start of the temperature hold; afterwards, the value approaches zero due to the constant temperature. An average was likewise computed using Equation 29 for each region. The constant had an average value of 1.625 x 10^{-6} in Region 1, 2.368 x 10^{-7} in Region 2, and 2.237 x 10^{-9} in Region 3. Complete results for mass flux are summarized in Table 8.

Table 8. Curve Fitting Results from Aluminum Coupon Mass Loss.

	T < 220ºC			220ºC < T < 260ºC			T < 500ºC		
Test	a	b	σ	a	b	σ	a	b	σ
RT0226a	-4.21x10^{-3}	3.59	2.08x10^{-6}	-2.26x10^{-2}	12.69	3.37x10^{-7}	-1.30x10^{-3}	1.27	1.86x10^{-9}
RT0226c	-4.81x10^{-3}	12.88	1.91x10^{-6}	-2.63x10^{-2}	23.51	3.92x10^{-7}	-1.38x10^{-3}	10.16	7.98x10^{-9}
RT0226d	-4.26x10^{-3}	3.55	1.01x10^{-6}	-2.14x10^{-2}	12.03	2.60x10^{-7}	-9.00x10^{-4}	1.02	1.29x10^{-9}
RT0226g	-1.99x10^{-3}	1.69	3.93x10^{-7}	-9.70x10^{-3}	5.46	1.44x10^{-7}	-5.81x10^{-4}	0.61	8.36x10^{-10}
RT0226i	-1.57x10^{-3}	1.24	2.46x10^{-6}	-7.55x10^{-3}	4.16	1.12x10^{-7}	-1.66x10^{-4}	0.23	2.37x10^{-10}
RT0226j	-2.18x10^{-3}	1.68	1.88x10^{-6}	-1.18x10^{-2}	6.41	1.75x10^{-7}	-8.50x10^{-4}	0.57	1.22x10^{-9}
AVERAGE	**-3.173x10^{-3}**	**4.106**	**1.625x10^{-6}**	**-1.656x10^{-2}**	**10.71**	**2.368x10^{-7}**	**-8.625x10^{-4}**	**2.31**	**2.237x10^{-9}**

relation.

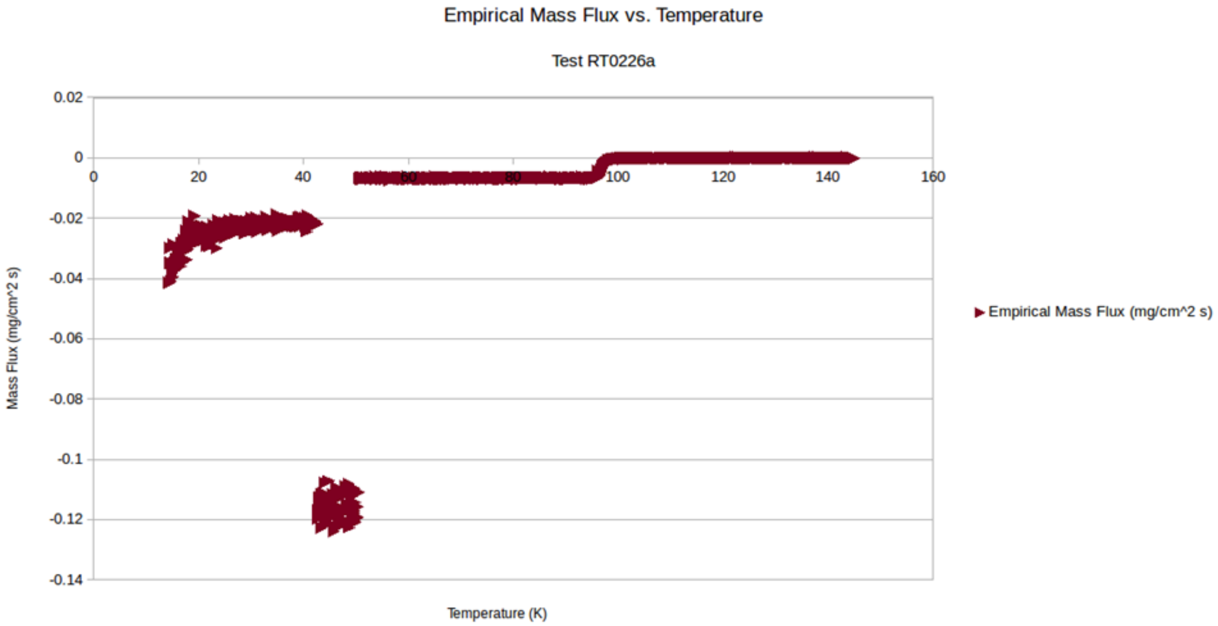

Figure 61. Mass Flux versus Temperature for an aluminum coupon.

One reservation to Nate Cooper's results should be noted: the derived accommodation coefficients were found primarily using samples with only chemisorbed water available; only one, RT0226c, had any free water present.[40] Therefore, the derived accommodation coefficients were considered more representative of the kinetics of decomposing aluminum oxyhydroxides than evaporating water. Note that the FHD and vacuum drying models each had two ranges of accommodation coefficients (total of six) to separately simulate the drying process of bulk liquid water added to the assemblies and chemisorbed water placed on the corroded plates. This was done because the initial bulk and chemisorbed water are inputted into the model separately. However, new accommodation coefficients were not derived for the bulk water in the FHD model as the humidity results from initial simulations compared well to the experimental data. This means that the accommodation coefficients for the bulk and chemisorbed water in the FHD model were both set to the values obtained in Table 3. This was unsurprising as evaporation rates in FHD and decomposition rates in the TGA tests analyzed are both dependent on temperature. For FHD tests, the temperature that controls the drying process is the gas temperature recirculating through the vessel.

Unlike FHD, bulk liquid water is vaporized in vacuum drying by reducing the vapor pressure below the saturation pressure through the reduction in the vessel's pressure. When the accommodation coefficients for the bulk and chemisorbed water in the vacuum drying model were set to values obtained in Table 3, initial results showed that the model was completely incapable of removing the bulk water (105 mL per assembly) on the assemblies. This indicates that new accommodation coefficients are needed to simulate the bulk liquid water drying process. Given that previous accommodation coefficients were obtained from corroded plates, using the same approach with experimental drying tests that contain bulk liquid water should provide more reasonable bulk water accommodation coefficients for the vacuum drying model.

A new accommodation coefficient for the bulk liquid water added to each of the 10 assemblies was derived from relative humidity and temperature data collected during experimental Vacuum-Drying Test 8. To determine the mass flux from the assemblies, the partial pressure of water was first derived from the chamber relative humidity and gas temperature at the relative humidity probe. This partial pressure was then used to generate plots of the mass of water vapor inside the chamber at any given time during the test. Using the generated plots and heating rates from the humidity probe, an average mass flux of 2.186×10^{-10} g/cm^2 was found for the 10 assemblies (398,300 cm^2 total surface area). The derived average mass flux was based on curve fitting results (Equation 27 and Equation 28) of evacuation periods following the 25 Torr hold. All evacuation periods prior to the 25 Torr hold were ignored as the saturation and vapor pressure were equal. Significant drying is occurring before 25 Torr, but data prior to 25 Torr poorly fitted regression lines during curve fitting, resulting in great uncertainty in the derived accommodation coefficient for those pressures. Therefore, an accommodation coefficient was calculated for each pulled data point beginning from the 25 Torr hold, resulting in an average σ of 5.083×10^{-7}. Although this σ was derived solely for Vacuum-Drying Test 8, this serves as a better baseline for all vacuum-drying test models.

8.1.3.4 Initial Conditions

While the exact initial conditions for each test varied, some generalizations were made. FHD tests were operated at an average pressure of 70 psi gauge and, accordingly, have this initial pressure. Vacuum-drying test simulations began slightly above one atm absolute with the initial pressure dependent on the inputted pressure table. For both FHD and vacuum drying, the initial temperature was dependent on the respective test's average temperature across all assemblies (typically 23°C for FHD, 33°C for vacuum). Both models had an initial composition of 1% by mole water vapor (or 95% relative humidity). While the initial relative humidity may seem high, it is purely a function of the elevated initial pressure; the water content remains low, and operational experience in both past drying tests and current efforts confirm this is normal.[38] The default values were left in place for the purposes of turbulence modeling; that is, a viscosity ratio of 10 (see Equation 12) and a velocity scale of 1 m/s.

The only remaining condition yet to be determined is the initial water content placed on the assemblies. Assuming a 10-µm-thick layer of pure gibbsite/bayerite (density 2.43 g/cm^3)[41] is grown on the corroded plates with a surface area of 487.74 cm^2, there will be a total of 1.185 g of gibbsite/bayerite present on each plate. Given that bayerite is 34.64% water by mass, it follows that there will be 0.411 g of chemisorbed water present per plate.[41] Thus, with 12 corroded plates, there will be a total of 4.93 g of chemisorbed water present at the start of any given test. This is applied to the appropriate corroded plate surfaces in STAR-CCM as an areal density of 0.841 mg/cm^3. Furthermore, because this calculation assumes 0% porosity in the oxide layer and because any boehmite present is guaranteed to have a smaller water content than bayerite,[41] this estimate may be viewed as the absolute upper limit of the chemisorbed content.

For the bulk water, estimates were made based on limited data available from Shalloo.[40] In the coupon drying tests in his work, drip-dried samples were found to have a substantially larger water content than those with only chemisorbed water present (4.26 mg/cm^2 vs. 0.94 mg/cm^2). This would seem to imply a ratio of 3.53 mg bulk water for each mg of chemisorbed water, assuming a uniform porosity for the oxyhydroxide layer. Similar to the chemisorbed water calculation, this assumption of uniform porosity may view the 3.53 mg ratio as the uppermost limit. Scaling this to the size of a full assembly, 105 g of bulk water can be expected per assembly, for a grand total of 1,050 grams in the test chamber. For practical purposes, this is applied as an initial condition of 2.84 mg/cm^2 of bulk water to the surface of each assembly. Chemisorbed, and physisorbed water were assumed to undergo the same vaporization rate in the model.

8.1.3.5 Mesh Refinement

Mesh refinement is a process used to optimize a mesh for performance and accuracy. First, the solution for a base case with a given mesh size is obtained. The base mesh is then refined by, for instance, doubling the number of cells, and a new solution to the problem is obtained. If the solution has only small changes between meshes, then the base mesh returns the actual numerical solution. This process can be repeated as many times as required to find the coarsest possible mesh that will also return a solution with minimal numerical error. The process can also be done in reverse by iteratively coarsening each successive mesh.

In this work, the initial, base case mesh was built using STAR-CCM's "Auto Mesh" feature, using a cell base size of 0.05 m in both the fluid and solid domains. The "Thin Mesher" option is also used; this creates a minimum of two cells across any high aspect ratio geometrical thickness. This minimum allows for the cells for the surrogate fuel plates and the air between them to be sufficiently refined without forcing an unreasonable number of computational cells. In the fluid domain, specific refinement of the surface mesh around the surrogate fuel plates was changed to be 0.002 m. The resulting mesh contained 2,264,092 fluid domain cells and 2,258,681 solid domain cells (including the aluminum surrogates and the steel basket), for a total of 4,522,773 cells. Subsequent meshes were developed by either increasing (i.e., coarsening; Rev3b) or decreasing (i.e., refining; Rev3c, 3d, and 3e) the cell base size in the fluid domain of the base case (Rev3a). A summary of the mesh data is found in Table 9.

Each simulation was given initial and boundary conditions for forced recirculation as described in Sections 8.1.3.1 and 8.1.3.4. The flow field was established by obtaining a stable steady-state solution after 2,000 iterations, with the species and energy equations frozen in their initial state. The transient solver was then activated, and the species and energy equations were unfrozen. To simulate drying, the Hertz-Knudsen relation (Equation 21) was applied using the accommodation coefficients previously derived (Table 9). This relation was applied to the entire solid surface of Assembly #4. After an acceptable mesh was achieved, the settings used for the region around Assembly #4 were applied to all geometric surfaces in the model. Assembly #4 was chosen to refine the mesh as it was the assembly that had the maximum thermal gradient. The final solution for use in comparison between meshes was obtained after five hours of physical time.

To compare each solution, a total of 20 temperature and vapor pressure probes were placed on four different assemblies. The five probes were located every 12.375 in in the axial direction of Assemblies 1, 4, 7, and 10. Because the flow tends to stagnate in the narrow gaps between plates, the probes were placed on the outermost plate of each assembly. An effort was made to make the placement of these probes roughly approximate to the center line of the basket cross section. Although these thermocouples were not the actual locations of the thermocouples used during experimental drying tests as mesh refinement was conducted prior to testing, the 20 probe locations allowed for a range of temperature conditions to be compared.

Results of the initial study are summarized in Table 10 and Table 11 (for temperature) and Table 12 and Table 13 (for water content, in mole fraction). The numerical solution for the mesh was considered sufficiently refined if the relative change in solution at each probe was less than 10%. Accordingly, the solution for temperature was accepted after one refinement (Rev3c), with an average change of 2.75% and a maximum change of 7.61%. However, the species solution for H_2O continued to be highly variable; even after a further two refinements (Rev3d and 3e), the average difference failed to fall below 16.85% (with a maximum change of 42.34% observed). Due to the computational costs of continued refinement, an unstructured mesh was used with a base cell size of 0.04 m for the majority of the domain, while a selectively refined, structured mesh was utilized in the regions expected to see drying.

To this end, a second set of meshes (Rev4) was developed with an emphasis on refining the region surrounding Assembly 4, achieved by manipulating the target size of cells located on the surface of the assembly. Details of each iteration of the selective meshes can be found in Table 9. Additionally, the number of mole fraction probes on the assembly was increased from five to 20 to aid in the evaluation of the mesh. Unfortunately, even after multiple refinements, a converged solution was not reached (see Table 12 and Table 13 for full results). At no point did the average change drop below the desired 10%, and the maximum change observed between solutions was regularly upwards of 40%. However, the solution was highly stable in the middle four-fifths of the assembly (an average percent difference of 7.91% between Rev4d and 4b). The measurements taken at the extreme end of the assembly tended to return wildly varying results between iterations even with a highly refined mesh (29.26% difference between Rev4d and 4b). This was attributed to poorly resolved cross flows altering the solution in these regions.

A final set of meshes was created by adding a boundary layer (via the “Prism Layer” option in STAR-CCM+) to better resolve and stabilize the velocity field near the surface of the assembly (see Table 9 for mesh details and Table 12 and Table 13 for results). This new series of meshes (Rev5) refined the mesh, either by incrementing the level of selective refinement around Assembly 4 (in the fashion of Rev4) or by incrementing number of cells in each prism layer. After some experimentation, an acceptable mesh was found in the fourth iteration (Rev5d), at which point all probes measured a change of less than 10% (maximum 7.13%, average 3.42%). Thus, the mesh utilized in this study consisted of 12,218,978 fluid cells and 2,261,931 solid (aluminum assembly, steel basket, and boron nitride) cells, for a total of 14,480,909 cells.

Table 9. Parameters and specifications for mesh refinement.

Sim Name	Fluid Volume Cell Base Size	Total Fluid Cells	Al Cell Base Size	Total Al Cells	Steel Cell Base Size	Total Steel Cells	Total Cells	Assembly 4 Target Size		Prism Layer?	Prism Layer Thickness (% of base cell size)		
Rev3b	0.075 m	1,013,664	0.05 m	1,831,554	0.05 m	427,127	3,272,345	10.00%	0.00750	No			
Rev3a	0.05 m	2,264,092	0.05 m	1,831,554	0.05 m	427,127	4,522,773	10.00%	0.00500	No			
Rev3c	0.04 m	3,595,760	0.05 m	1,831,554	0.05 m	427,127	5,854,441	10.00%	0.00400	No			
Rev3d	0.0375 m	4,262,153	0.05 m	1,831,554	0.05 m	427,127	6,520,834	10.00%	0.00375	No			
Rev3e	0.035 m	4,940,234	0.05 m	1,831,554	0.05 m	427,127	7,198,915	10.00%	0.00350	No			
Rev4a	0.04 m	4,333,451	0.05 m	1,831,554	0.05 m	427,127	6,592,132	5.00%	0.00200	No			
Rev4c	0.04 m	4,909,563	0.05 m	1,831,554	0.05 m	427,127	7,168,244	4.00%	0.00160	No			
Rev4e	0.04 m	5,367,963	0.05 m	1,831,554	0.05 m	427,127	7,626,644	3.50%	0.00140	No			
Rev4d	0.04 m	6,098,911	0.05 m	1,831,554	0.05 m	427,127	8,357,592	3.00%	0.00120	No			
Rev4b	0.04 m	7,225,213	0.05 m	1,831,554	0.05 m	427,127	9,483,894	2.50%	0.00100	No			
Rev5a	0.04 m	4,906,658	0.05 m	1,831,554	0.05 m	427,127	7,165,339	5.00%	0.00200	Yes	33.33%	0.01333	2 Cells
Rev5b	0.04 m	5,499,805	0.05 m	1,831,554	0.05 m	427,127	7,758,486	4.00%	0.00160	Yes	33.33%	0.01333	2 Cells
Rev5c	0.04 m	5,965,489	0.05 m	1,831,554	0.05 m	427,127	8,224,170	3.50%	0.00140	Yes	33.33%	0.01333	2 Cells
Rev5d	0.04 m	6,003,277	0.05 m	1,831,554	0.05 m	427,127	8,261,958	4.00%	0.00160	Yes	33.33%	0.01333	3 Cells
Rev5e	0.04 m	5,952,685	0.05 m	1,831,554	0.05 m	427,127	8,211,366	5.00%	0.00200	Yes	33.33%	0.01333	4 Cells

Table 10. Mesh refinement temperature results (h = 49.5 inches).

Sim Name	Assembly 1 (% h)					Assembly 4 (% h)					Assembly 7 (% h)					Assembly 10 (% h)				
	0.00	0.25	0.50	0.75	1.00	0.00	0.25	0.50	0.75	1.00	0.00	0.25	0.50	0.75	1.00	0.00	0.25	0.50	0.75	1.00
Rev3a	495.56	420.19	384.97	367.48	354.64	446.87	411.41	391.91	377.28	359.57	458.12	419.38	384.07	367.10	356.69	501.13	419.21	378.87	360.44	348.03
Rev3b	457.84	408.87	379.32	360.23	352.91	433.26	404.42	387.62	370.45	360.35	443.74	406.21	372.44	357.81	349.69	469.07	400.95	364.68	338.49	348.47
Rev3c	494.53	410.46	376.64	360.63	360.63	436.13	403.04	377.35	364.72	357.89	455.30	411.96	377.82	362.02	352.52	508.59	420.08	378.33	358.91	346.86
Rev3d	497.21	413.01	379.11	360.99	350.81	437.01	402.94	380.10	363.96	359.40	456.65	413.91	380.31	364.01	354.44	499.43	420.28	379.84	360.53	347.76
Rev3e	486.90	409.35	375.53	359.53	351.14	445.68	407.44	381.64	365.89	354.20	456.33	414.83	381.90	365.42	355.90	510.71	422.26	380.86	361.48	349.16
Rev4a	490.55	412.21	376.99	359.68	349.20	431.56	396.39	370.34	357.95	351.36	454.89	411.51	377.42	360.92	352.12	503.07	420.01	377.73	358.61	346.39
Rev4b	481.49	413.09	380.03	364.88	355.05	445.92	404.63	377.71	365.16	356.09	458.83	416.78	383.26	367.22	357.41	505.40	423.42	382.46	362.99	350.46
Rev4c	490.90	415.66	380.69	363.83	363.83	443.75	405.73	380.54	368.02	354.21	458.81	416.59	384.14	367.46	357.66	501.47	424.03	382.49	363.10	350.28
Rev4d	496.09	414.68	379.50	363.85	355.31	445.23	402.95	378.64	368.21	336.31	458.12	416.58	382.43	366.77	357.25	506.42	423.22	381.55	362.56	349.95
Rev4e	493.39	412.45	376.13	359.59	350.30	438.55	394.79	367.53	354.19	346.05	448.02	411.58	377.39	361.82	351.97	511.43	420.47	378.79	359.17	347.09
Rev5a	472.78	399.17	366.38	349.93	341.30	422.74	390.85	360.38	346.88	338.83	427.74	397.84	365.33	349.97	341.02	489.07	408.04	368.47	350.16	339.52
Rev5b	465.25	399.12	366.59	350.06	340.98	425.85	389.14	358.71	346.16	308.73	427.43	397.00	365.33	350.00	340.89	502.35	407.66	367.87	349.71	339.11
Rev5c	477.49	398.92	366.32	349.83	341.13	423.31	384.47	355.66	341.71	334.68	426.73	396.06	364.39	348.45	340.48	495.17	407.68	368.15	349.87	339.26
Rev5d	460.16	395.23	363.69	347.77	339.54	424.50	384.19	355.93	342.88	335.97	440.50	397.01	364.87	349.58	340.91	484.63	409.12	368.79	350.30	339.49
Rev5e	496.67	409.12	375.84	359.16	350.44	435.03	396.53	369.16	356.44	349.17	438.70	404.48	373.25	358.22	349.81	476.98	411.77	374.38	356.76	347.02

Table 11. Change in temperature results relative to the next finest mesh (h = 49.5 inches).

Meshes % Diff	Assembly 1 (% h)					Assembly 4 (% h)					Assembly 7 (% h)					Assembly 10 (% h)					Max. % Diff	Avg. % Diff
	0.00	0.25	0.50	0.75	1.00	0.00	0.25	0.50	0.75	1.00	0.00	0.25	0.50	0.75	1.00	0.00	0.25	0.50	0.75	1.00		
3b/3a	7.61	2.69	1.47	1.97	0.49	3.05	1.70	1.09	1.81	0.22	3.14	3.14	3.03	2.53	1.96	6.40	4.36	3.75	6.09	0.13	7.61	2.75
3a/3c	0.21	2.37	2.21	1.90	1.66	2.46	2.08	3.86	3.44	0.47	0.62	1.80	1.65	1.40	1.18	1.47	0.21	0.14	0.43	0.34	3.86	1.45
3c/3d	0.54	0.62	0.65	0.10	2.80	0.20	0.02	0.72	0.21	0.42	0.30	0.47	0.65	0.55	0.54	1.83	0.05	0.40	0.45	0.26	2.80	0.58
3d/3e	2.12	0.89	0.95	0.41	0.09	1.95	1.10	0.40	0.53	1.47	0.07	0.22	0.42	0.39	0.41	2.21	0.47	0.27	0.26	0.40	2.21	0.72
3c/4a	0.81	0.42	0.09	0.26	3.27	1.06	1.68	1.89	1.89	1.86	0.09	0.11	0.11	0.30	0.11	1.10	0.02	0.16	0.08	0.14	3.27	0.76
4a/4c	0.07	0.83	0.97	1.14	4.02	2.75	2.30	2.68	2.74	0.80	0.85	1.22	1.75	1.78	1.55	0.32	0.95	1.24	1.24	1.11	4.02	1.51
4c/4e	0.50	0.78	1.21	1.18	3.86	1.19	2.77	3.54	3.90	2.36	2.41	1.22	1.79	1.56	1.62	1.95	0.85	0.98	1.09	0.92	3.90	1.76
4e/4d	0.54	0.54	0.89	1.17	1.41	1.50	2.03	2.93	3.81	2.90	2.20	1.20	1.32	1.35	1.48	0.99	0.65	0.72	0.94	0.82	7.80	1.77
4d/4b	3.03	0.38	0.14	0.28	0.07	0.15	0.42	0.25	0.84	5.55	0.15	0.05	0.22	0.12	0.04	0.20	0.05	0.24	0.12	0.15	7.33	0.94
4a/5a	3.76	3.27	2.90	2.79	2.31	2.09	1.42	2.76	3.19	3.70	6.35	3.44	3.31	3.13	3.25	2.86	2.93	2.51	2.41	2.02	6.35	2.98
5a/5b	1.62	0.01	0.06	0.04	0.09	0.73	0.44	0.47	0.21	9.75	0.07	0.21	0.00	0.01	0.04	2.64	0.09	0.16	0.13	0.12	9.75	0.80
5b/5c	2.56	0.05	0.07	0.07	0.04	0.60	1.21	0.86	1.30	7.75	0.16	0.24	0.26	0.44	0.12	1.45	0.00	0.08	0.05	0.04	7.75	0.85
5c/5d	3.77	0.93	0.72	0.59	0.47	0.28	0.07	0.08	0.34	0.38	3.13	0.24	0.13	0.32	0.13	2.17	0.35	0.17	0.12	0.07	3.77	0.71
5d/5e	7.35	3.40	3.23	3.17	3.11	2.42	3.11	3.58	3.80	3.78	0.41	1.85	2.25	2.41	2.54	1.60	0.64	1.49	1.81	2.17	7.35	2.68

Table 12. Mesh refinement mole fraction results (h = 49.5 inches).

Sim Name	Assembly 4																				
	0.00	0.05	0.10	0.15	0.20	0.25	0.30	0.35	0.40	0.45	0.50	0.55	0.60	0.65	0.70	0.75	0.80	0.85	0.90	0.95	1.00
Rev3a	0.1282	0.0851	0.1409	0.1350	0.1520	0.1422	0.1479	0.1850	0.1517	0.1867	0.1721	0.1818	0.1773	0.2065	0.2026	0.2041	0.2167	0.1935	0.2420	0.2183	0.3407
Rev3b	0.0752	0.0912	0.0922	0.0984	0.1709	0.1804	0.1957	0.1993	0.1868	0.1799	0.2060	0.2111	0.1904	0.1945	0.2107	0.2070	0.2011	0.2222	0.2288	0.2127	0.2201
Rev3c	0.1703	0.0731	0.1413	0.1123	0.1212	0.1623	0.1548	0.1997	0.1739	0.1744	0.1748	0.1556	0.1984	0.2656	0.1986	0.2205	0.2229	0.2034	0.2228	0.2403	0.3329
Rev3d	0.1165	0.0834	0.1025	0.1800	0.1166	0.1443	0.1786	0.1388	0.1473	0.1746	0.1833	0.2197	0.2117	0.2196	0.2179	0.2047	0.1899	0.2404	0.2542	0.1985	0.2228
Rev3e	0.1658	0.0743	0.1447	0.1233	0.1283	0.1428	0.1420	0.1715	0.1769	0.1630	0.1560	0.1707	0.1706	0.2267	0.2144	0.1816	0.1964	0.2068	0.2215	0.2672	0.2531
Rev4a	0.1358	0.0847	0.1059	0.1190	0.1238	0.1331	0.1375	0.1421	0.1517	0.1584	0.1649	0.1722	0.1785	0.1859	0.1928	0.2012	0.2086	0.2149	0.2234	0.2303	0.2684
Rev4b	0.1668	0.0907	0.1202	0.1404	0.1859	0.1665	0.1480	0.1522	0.1662	0.1776	0.1852	0.1905	0.1957	0.2009	0.2065	0.2125	0.2185	0.2230	0.2296	0.2349	0.3535
Rev4c	0.1504	0.0994	0.1271	0.1979	0.1844	0.1662	0.1524	0.1582	0.1774	0.1995	0.2090	0.2057	0.2008	0.2027	0.2095	0.2188	0.2268	0.2302	0.2349	0.2389	0.4080
Rev4d	0.1864	0.1209	0.1654	0.1741	0.1559	0.1627	0.1620	0.1670	0.1754	0.1842	0.1926	0.1984	0.2024	0.2063	0.2101	0.2134	0.2158	0.2220	0.2449	0.3426	0.1566
Rev4e	0.1417	0.0794	0.1112	0.1273	0.1341	0.1437	0.1525	0.1619	0.1698	0.1781	0.1853	0.1938	0.2008	0.2094	0.2157	0.2253	0.2301	0.2371	0.2449	0.2520	0.2878
Rev5a	0.2096	0.1141	0.1388	0.2044	0.2185	0.2308	0.2374	0.2438	0.2479	0.2500	0.2534	0.2589	0.2644	0.2694	0.2748	0.2818	0.2885	0.2950	0.3009	0.3063	0.3203
Rev5b	0.1930	0.1127	0.1517	0.2216	0.2297	0.2300	0.2369	0.2372	0.2386	0.2399	0.2398	0.2424	0.2469	0.2516	0.2567	0.2679	0.2788	0.2842	0.2858	0.2889	0.3928
Rev5c	0.1844	0.1099	0.1241	0.1500	0.1784	0.1762	0.1876	0.2039	0.2218	0.2371	0.2470	0.2537	0.2588	0.2640	0.2698	0.2703	0.2732	0.2847	0.2953	0.2965	0.3193
Rev5d	0.1916	0.1084	0.1299	0.1591	0.1755	0.1870	0.1968	0.2061	0.2143	0.2222	0.2305	0.2388	0.2466	0.2539	0.2608	0.2678	0.2746	0.2813	0.2879	0.2947	0.3240
Rev5e	0.1655	0.0943	0.1235	0.1447	0.1749	0.1856	0.1980	0.2085	0.2179	0.2266	0.2354	0.2431	0.2504	0.2574	0.2639	0.2706	0.2768	0.2833	0.2896	0.2964	0.3238

Table 13. Change in mole fraction result relative to the next finest mesh (h = 49.5 inches).

Meshes % Diff	Assembly 4																					Max. % Diff	Avg. % Diff
	0.00	0.05	0.10	0.15	0.20	0.25	0.30	0.35	0.40	0.45	0.50	0.55	0.60	0.65	0.70	0.75	0.80	0.85	0.90	0.95	1.00		
3b/3a	41.35	7.14	34.59	27.06	12.42	26.83	32.32	7.70	23.10	3.65	19.70	16.11	7.42	5.78	4.02	1.42	7.22	14.84	5.43	2.55	35.41	41.35	16.25
3a/3c	24.71	16.45	0.32	20.21	25.42	12.34	4.43	7.34	12.75	7.07	1.54	16.82	10.63	22.27	2.01	7.44	2.76	4.88	8.63	9.16	2.34	25.42	10.63
3c/3d	31.63	14.03	27.45	60.29	3.80	11.07	15.42	30.48	15.27	0.15	4.91	41.17	6.73	17.31	9.72	7.14	14.78	18.19	14.12	17.38	33.08	60.29	18.02
3d/3e	42.34	10.85	41.14	31.48	10.06	1.05	20.53	23.59	20.06	6.63	14.94	22.32	19.41	3.23	1.61	11.31	3.43	13.97	12.87	34.58	13.62	42.34	16.85
3c/4a	25.47	13.71	33.49	5.67	2.08	21.92	12.53	40.54	14.65	10.06	5.97	9.60	11.13	42.87	3.00	9.56	6.83	5.34	0.28	4.33	24.03	42.87	13.96
4a/4c	9.73	14.74	16.71	39.84	32.88	19.90	9.77	10.20	14.48	20.61	21.10	16.30	11.12	8.28	7.97	8.04	8.01	6.66	4.91	3.60	34.21	39.84	14.84
4c/4e	6.12	25.10	14.33	55.46	37.58	15.61	0.07	2.26	4.48	12.05	12.79	6.12	0.02	3.18	2.87	2.86	1.43	2.91	4.08	5.19	41.77	55.46	12.11
4e/4d	23.96	34.27	32.79	26.91	14.00	11.68	5.82	3.08	3.24	3.31	3.80	2.30	0.77	1.51	2.65	5.58	6.61	6.81	0.02	26.44	83.76	83.76	14.36
4d/4b	11.73	33.26	37.64	24.04	16.14	2.23	9.44	9.73	5.58	3.70	4.01	4.14	3.40	2.65	1.76	0.40	1.21	0.46	6.65	45.83	55.70	55.70	13.73
4a/5a	35.23	25.72	23.73	41.77	43.35	42.33	42.05	41.73	38.82	36.64	34.93	33.50	32.50	30.99	29.86	28.58	27.68	27.15	25.77	24.81	16.20	43.35	31.10
5a/5b	8.58	1.25	8.50	7.76	4.88	0.34	0.20	2.79	3.91	4.23	5.68	6.81	7.10	7.10	7.08	5.15	3.48	3.80	5.28	6.03	18.47	18.47	6.16
5b/5c	4.70	2.53	22.21	47.75	28.81	30.56	26.30	16.36	7.57	1.16	2.90	4.45	4.60	4.70	4.87	0.89	2.04	0.19	3.22	2.55	23.04	47.75	11.78
5b/5d	3.79	1.36	4.46	5.71	1.63	5.81	4.70	1.09	3.50	6.74	7.13	6.22	4.96	3.97	3.44	0.94	0.52	1.19	2.60	0.62	1.44	12.53	3.83
5d/5e	15.82	15.00	5.24	9.97	0.36	0.77	0.62	1.14	1.65	1.96	2.06	1.78	1.51	1.37	1.16	1.03	0.79	0.70	0.62	0.60	0.05	20.28	3.84

8.2 Process Model Simulations and Validation

The two drying models discussed in Section 8.1 were validated for one FHD test and one vacuum-drying test (FHD Test 7, Vacuum-Drying Test 8) based on thermocouple measurements. Results shown in this section employ accommodation coefficients derived from (not entirely independent of) the experimental data. Due to time constraints, the models were not validated against more drying tests. During the validation process, for the vacuum-drying model to run, steady-state initialization needed to be skipped, and the simulation needed to begin with the transient solver activated and the flow, species, and energy equations unfrozen. In addition, to prevent divergence during the vacuum-drying simulations (as there are very large changes occurring in an unsteady problem), a field function was used to gradually ramp up the time steps. All thermocouples and the relative humidity probe used during the experiments were implemented into both models.

The FHD model operated with a velocity of 260.75 m/s (105 lb/hr) and an inlet temperature that was represented by the inlet gas temperature data collected during FHD Test 7. The nichrome wire (in Assembly 4) power was also defined by the power data collected during the experimental test. Seven corroded plates were implemented into the model (matching the experiment) with three on Assembly 1 (A, B, C), two on Assembly 4 (B, C), one on Assembly 7 (A), and one on Assembly 10 (A). No additional check was done regarding the accuracy of the results through mesh refinement as there was no need. Assembly 4 was chosen in the previous section to refine the mesh as it was the assembly that had the maximum thermal gradient. The wall boundary condition matched the 260°C heating tapes utilized during the experiment.

The vacuum-drying model operated based on the chamber pressure data collected during Vacuum-Drying Test 8. The nichrome wire power was also represented by the power data collected during the experiment. The same seven corroded plates were utilized in Vacuum-Drying Test 8 and were implemented into the model accordingly. The experiment operated the heating tapes at 100°C, and this was represented through the wall boundary condition.

8.2.1 FHD Modeling Results

8.2.1.1 FHD Thermal Results

There are two primary benchmarks in judging the thermal results for the FHD model: assembly average temperature and bottom-to-top temperature lag. Each were computed through the same process discussed in Section 6.1. The experimental data and model results for the average temperature of each assembly are shown in Figure 62. The figure immediately reveals that too much heat is being applied to the wall in the model, as Assemblies 1 and 10 (measured assemblies closest to the chamber wall) have temperatures 10–20°C higher than their experimental data by the 2-hour mark. Up until the 3.5-hour mark, the model shows Assembly 4 and 7 plates to be up to 20°C less than the experimental data. Although it seems there was more heat being generated in the model, the simulation did a good job in achieving steady-state temperatures at nearly the same time the experimental test did (6-hour mark). Although not believed to be the main contributor, an overall increase in the assemblies' temperature could be associated with the model assuming a constant internal pressure of 70 psig, neglecting that the ideal gas law implies that a decrease in pressure generally results in a decrease in temperature. Visual observations of temperature data during tests showed assembly temperatures increasing and decreasing each time the system pressure increased and decreased (from venting and purging helium) to maintain a 70 psig inlet pressure.

The maximum temperatures observed in the model came to within a 3–13% error of the experimental data as shown in Table 14. The table also highlights that, experimentally, the heating tapes resulted in an asymmetric heating profile with the top of the assemblies being the hottest location, whereas the model depicted uniform temperatures along each assembly due to the even thermal boundary on the chamber wall. Most of the error in the readings were found at the bottom of the assemblies which could be due again to too much heat being applied to the lower portion of the chamber wall. Although the model did not accurately represent the axial maximum temperature profile for each assembly, Figure 63 illustrates that the model did accurately depict the temperature distribution along Assembly 1 during the heat-up phase to the assembly's maximum temperature. The model represented similar temperature distributions for all other assemblies.

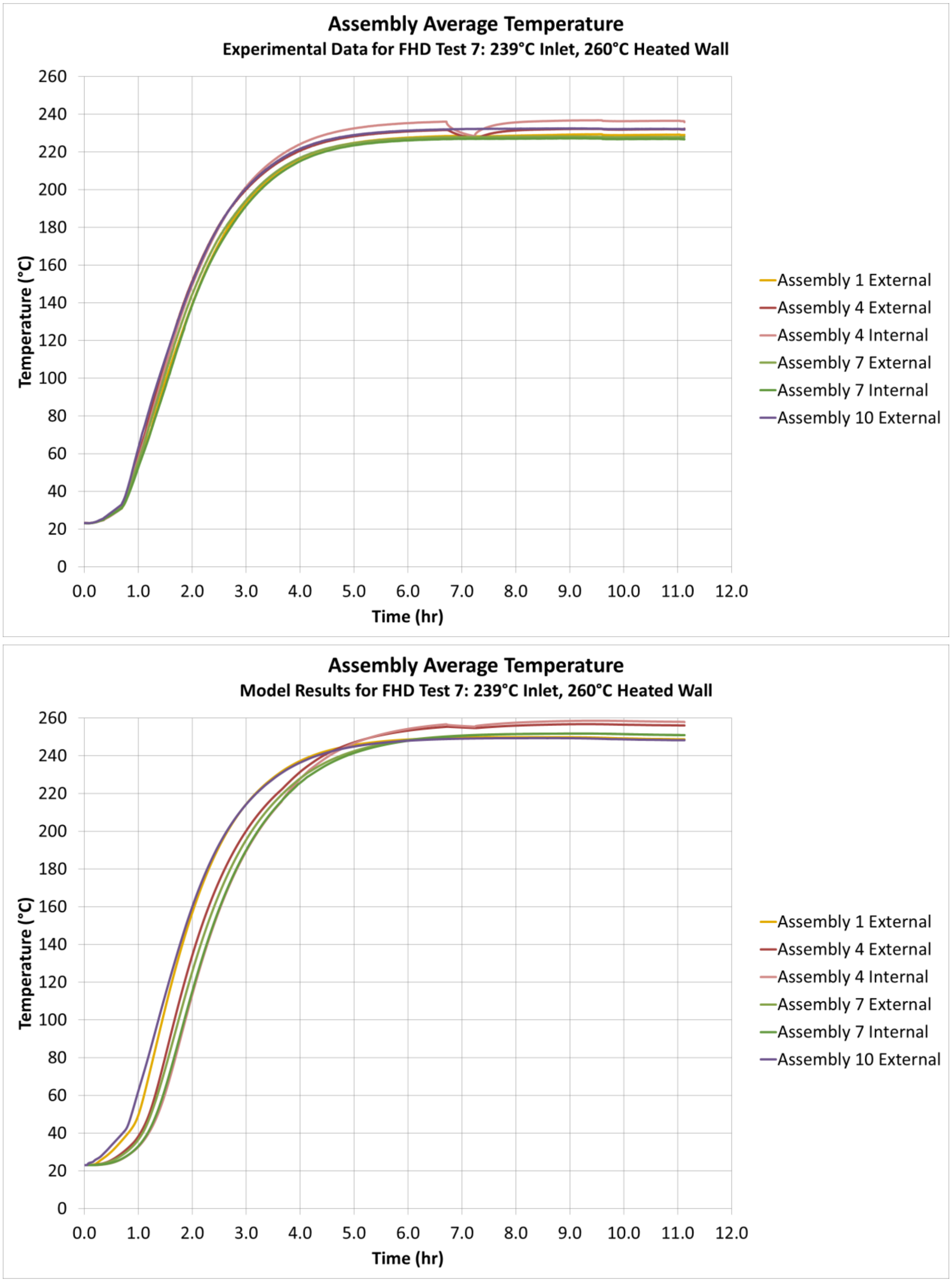

Figure 62. FHD Test 7 average temperatures of select assemblies for their external or internal plate from experimental data (top) and from outputted results of the model (bottom).

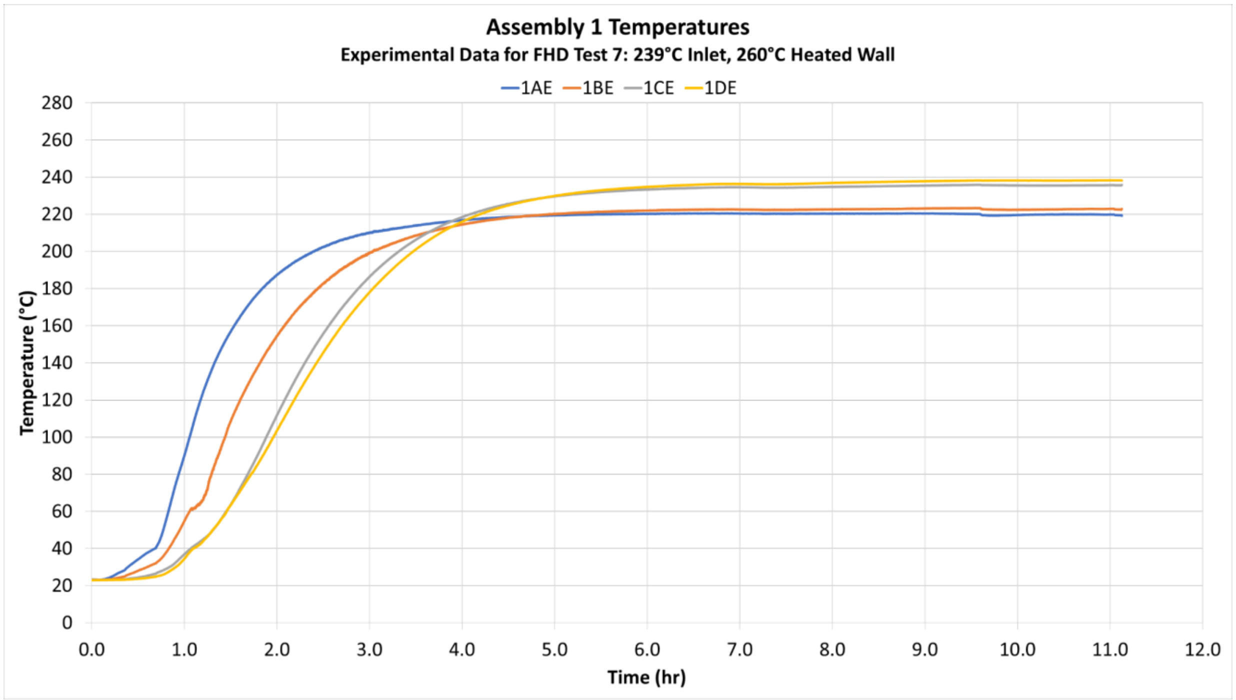

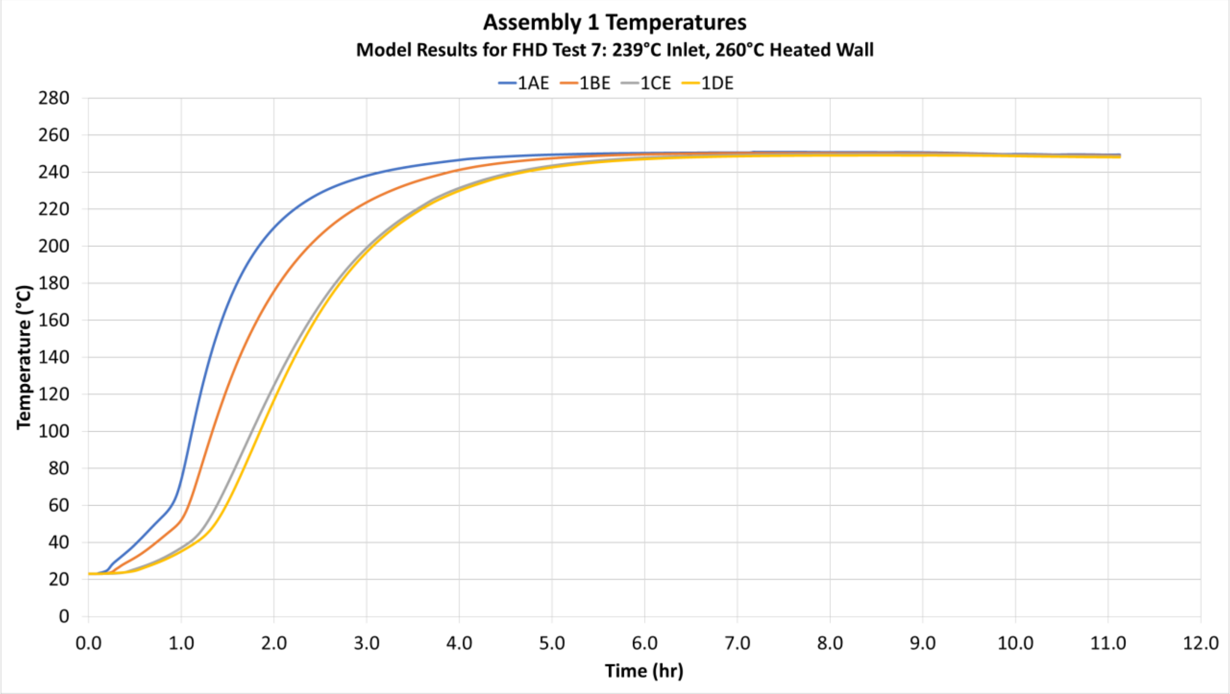

Figure 63. FHD Test 7 axial temperature profile of Assembly 1 from the experimental drying test (top) and from the model (bottom).

Table 14. Comparison of maximum temperature achieved at each assembly thermocouple location for the experimental drying test and outputted results from the model; FHD Test 7.

Assembly Thermocouple Location	Data Max Temperature (°C)	Model Max Temperature (°C)	Error (%)	Average Error (%)
1a External	220.534	250.826	13.74	9.02
1b External	223.372	250.251	12.03	
1c External	235.876	249.597	5.82	
1d External	238.299	248.972	4.48	
4a External	227.824	253.914	11.45	10.45
4b External	231.846	258.330	11.42	
4c External	233.050	258.440	10.89	
4d External	237.352	256.435	8.04	
4a Internal	234.416	257.337	9.78	8.33
4b Internal	233.327	260.416	11.61	
4c Internal	240.399	260.162	8.22	
4d Internal	247.286	256.443	3.70	
7a External	224.614	251.748	12.08	10.30
7b External	228.146	251.689	10.32	
7c External	235.552	251.737	6.87	
7d External	225.068	251.882	11.91	
7a Internal	223.909	251.654	12.39	10.75
7b Internal	224.502	251.645	12.09	
7c Internal	230.459	251.754	9.24	
7d Internal	230.584	251.990	9.28	
10a External	230.333	249.522	8.33	7.22
10b External	229.838	249.363	8.49	
10c External	239.467	249.272	4.09	
10d External	230.931	249.314	7.96	

Bottom-to-top temperature lag plots of Assemblies 1, 4, 7, and 10 in Figure 64 show that the assemblies in the simulation achieved their peak temperature lag at nearly the same time stamp that the assemblies did during the experiment. Assemblies 1 and 10 had higher peak temperature lags during the simulation due to the heat flux boundary (from heating tapes) heating the bottom of their assemblies at a much faster rate. Assemblies 4 and 7 saw a significant drop (30–45°C) in their peak temperature lag during the simulation. Although a reconfiguration of the assemblies inside the model would be necessary to confirm, the significant drop in the peak temperature lag may be attributed to a difference in the orientation of the assemblies inside the basket. The model assumes the assemblies are completely symmetrical and standing straight up. However, during the experimental tests, the four assemblies (1, 4, 7, and 10) are often angled or leaning against their basket slot wall, possibly as a result of the chamber sitting on slightly uneven insulation. This difference could have led to uneven heat gas distribution along each assembly.

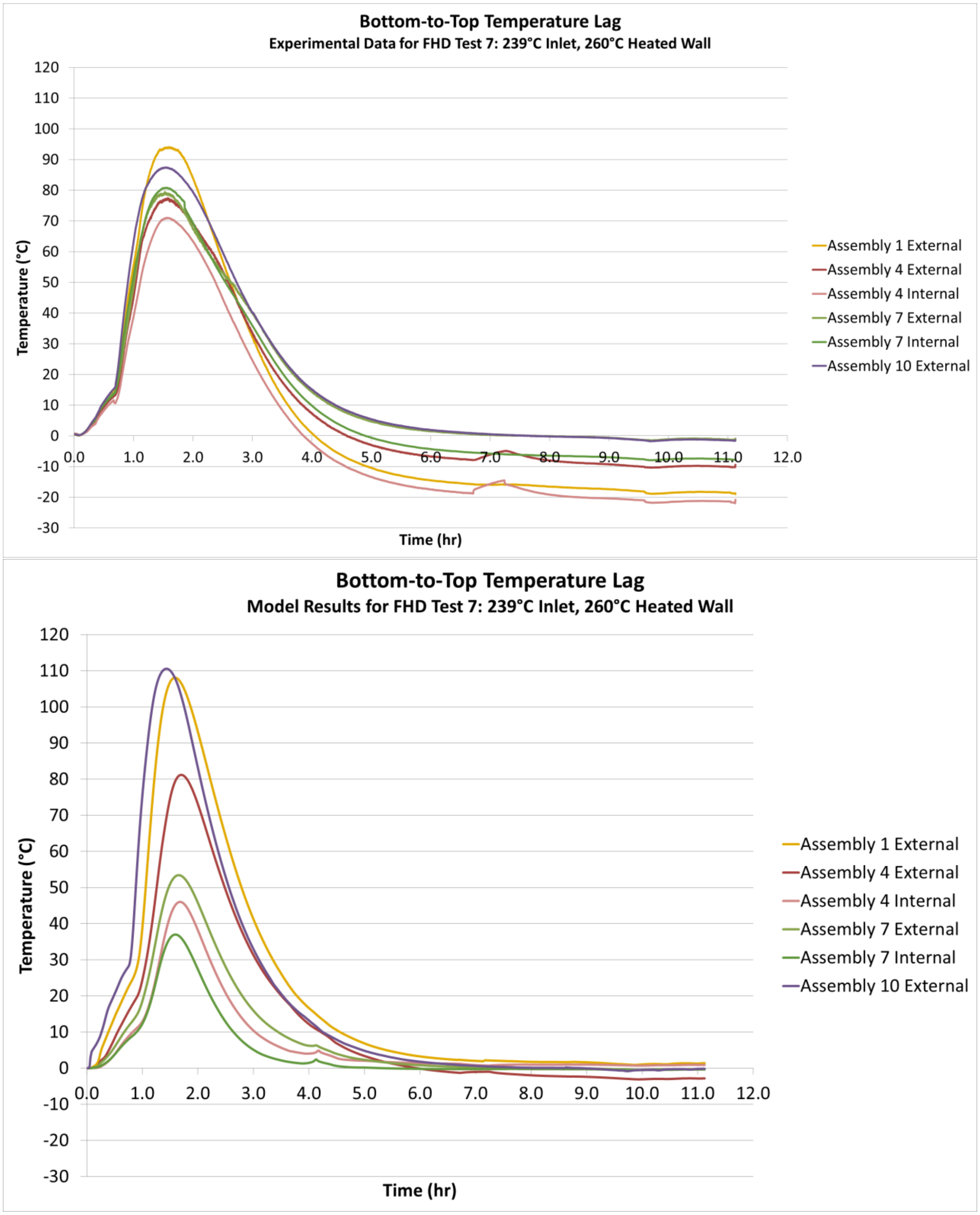

Figure 64. FHD Test 7 bottom-to-top temperature lag of select assemblies for their external or internal plate from experimental data (top), and from outputted results of the model (bottom.)

8.2.1.2 FHD Residual Moisture Results

As described in Section 6.1, the initial water content, representing both bulk and chemisorbed water, was applied to the surface of each assembly as an average areal density and steadily reduced by the application of the Hertz-Knudsen equation (Equation 21) as a boundary condition. The remaining content was monitored at any time from within STAR-CCM+ by taking the area integral of the current areal density of water.

Chamber relative humidity data collected during the experimental drying test was used to compare the residual water (both bulk and chemisorbed water) results obtained by the model, as shown in Figure 65. The figure indicates that majority of the residual water was removed by the 4-hour mark and that all water was removed just after the 7-hour mark. The simulation modeled the drying process as well as the relative humidity data, and dew point readings indicated that all bulk water was removed within 4 hours after turning on the FHD blower. Also, the model mimicked the experimental relative humidity where the majority of the water was removed between the 1.5-hour mark and 4-hour mark. The model was further supported by Figure 66, indicating the majority of the assemblies were fully dried of bulk water approximately 3.75 hours after turning on the blower. The lone exception was Assembly 2, which completely dried 30 minutes later at the 4.25-hour mark. Also, for FHD Test 7, the 220°C temperature criterion for the assemblies were achieved at approximately the 3-hour mark. Therefore, the residual chemisorbed water plots from the simulation show that after 7.25 hours no further decomposition occurs. This matches the TGA results that indicated FHD tests that operated for 6 hours at 220°C had similar TGA results of FHD tests that operated for 12 hours at 220°C. However, the model did show all chemisorbed water was removed during FHD, which is not in agreeance with the TGA data. This may be due to the model not having a fully detailed and accurate description of the decomposition of the aluminum oxyhydroxides. Note that the assemblies in the bottom plot of Figure 66 begin with different amounts of chemisorbed water, representing the different amounts of corroded plates added to each assembly. As previously shown in Table 2, the experimental FHD test 7 had three corroded plates in assembly 1, two corroded plates in assembly 4, and one corroded plate in assembly 7 and 10.

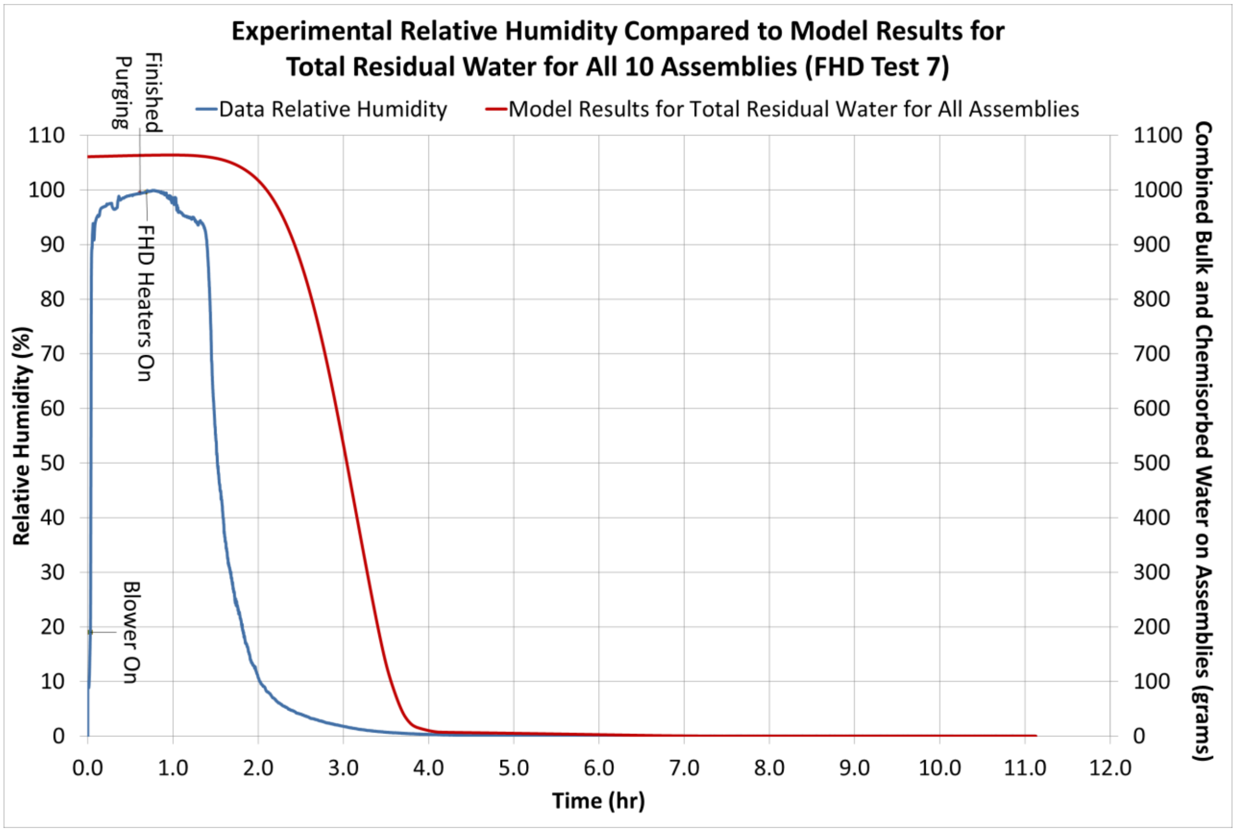

Figure 65. Comparison between FHD Test 7 experimental relative humidity measured inside the vessel and the model's reading of total residual water (both bulk and chemisorbed) for all 10 assemblies.

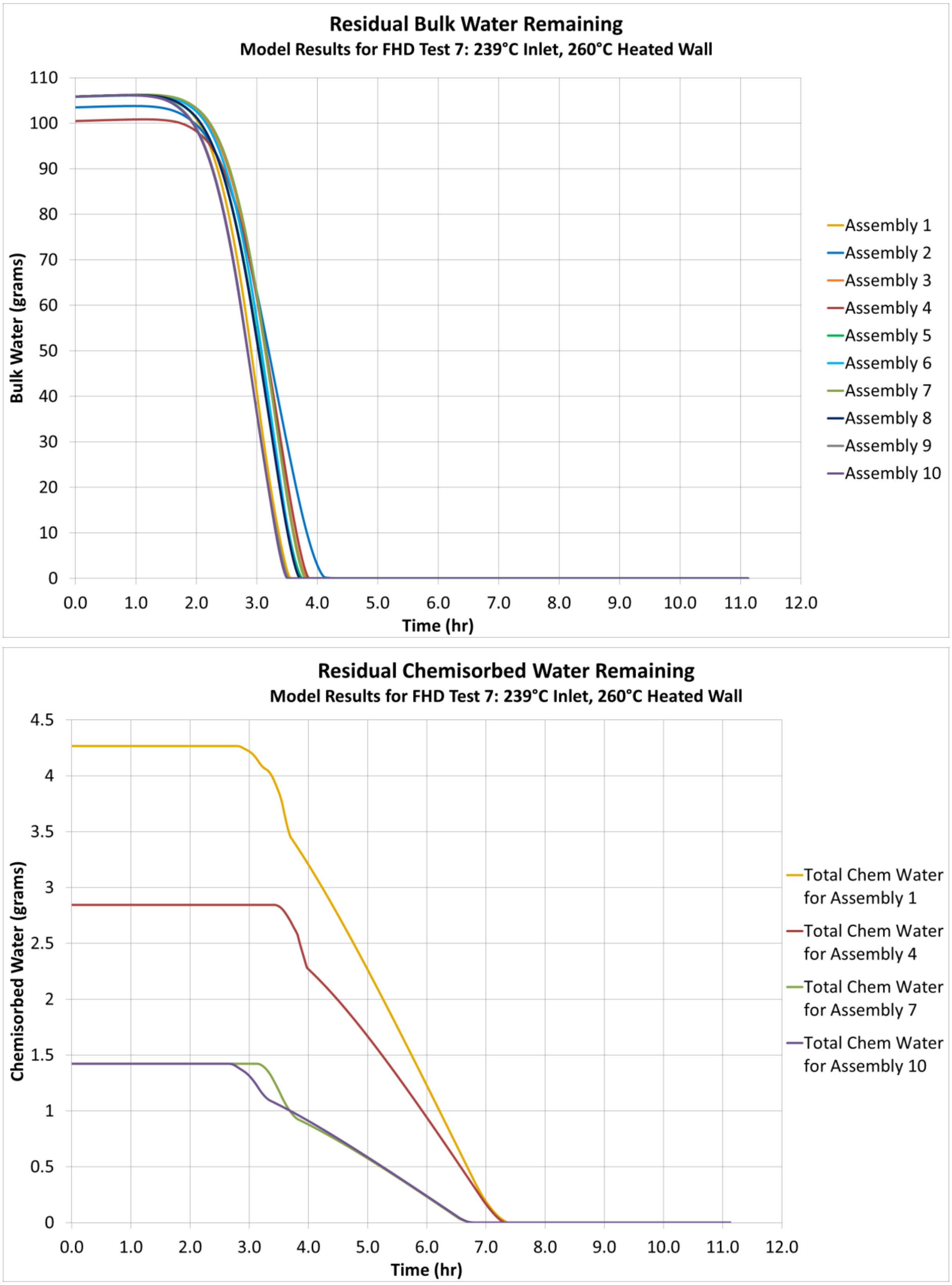

Figure 66. FHD Test 7 model results for residual bulk added to each assembly (top) and total residual chemisorbed water that was present in Assembly 1, 4, 7, and 10 (bottom).

8.2.2 Vacuum-Drying Modeling Results

8.2.2.1 Vacuum-Drying Thermal Results

Thermal results from the vacuum model were judged based on the assembly average temperature and the heating rate at each assembly thermocouple location. The experimental data and model results for the average temperature of each assembly are shown in Figure 67 (next page). The disparity is believed to be due to the model assuming an even coating of 105 mL of water on each assembly. Visual observations have confirmed that majority of the water drips to the bottom of the assemblies prior to beginning experimental vacuum drying. As a result, experimental data shows significant decrease in temperatures at the bottom of the assemblies during experimental tests due to the thermal impact of vaporization. However, altering the distribution of water in the model would not impact the average temperature of the assemblies given that at this time the model does not account for the impact vaporization has on temperature. The experimental data shows a temperature differential of 25–31°C between the internal and external plate of Assembly 4. However, the model only indicates a temperature differential of 3.5–5.5°C. Given that the assemblies were tighten until snugged for each experimental test to match the snugged fit that the model depicts of the assemblies, it is not believed that this temperature difference is due to the model not matching the thermal resistances due to possible air gaps between parts of the assemblies. Therefore, this temperature difference could again be associated with the model assuming a symmetrical loading of the assemblies inside the basket. Since Assembly 4 was leaning against the basket slot wall during the experimental test, this positioning could have resulted in the heat generated from the nichrome wire displacing to the basket rather than the external plate of Assembly 4. This difference in the surrogate assembly locations is seen when comparing the experimental image in Figure 9 to the computer-aided design (CAD) of the simulation that is shown in Figure 58.

The difference in orientation may have also contributed to Assembly 10 having lower temperatures during the simulation. Assembly 10 was also leaning against the basket wall during the experiment. Thus, when the model assumed it was not touching the wall, less heat (from chamber wall heating tapes) was transferred to Assembly 10, resulting in an overall lower temperature. However, as shown in Figure 68, the biggest thermal difference between the experimental data and simulation results was the model's inability to predict the temperature drops that occur during evacuation. One potential source for this error is the lack of heat loss from evaporation of water from the fuel surface. Unless this inability is due to the water distribution on the surface area of each assembly, this thermal difference raises concerns of whether the model can predict if freezing occurs.

Overall, the maximum temperatures observed in the model came to within a 2–48% error of the experimental data, as shown in Table 15. However, the error range is reduced to 2–20% if the temperatures from Assembly 4's external plate is ignored. Like the FHD model, Table 15 highlights that the model was not able to predict the asymmetric heating profile for each assembly. However, after observing Assembly 1 and 10's temperatures, it may have been the inaccurate axial distribution of heat on the chamber wall that was causing the error in their readings. Only Assembly 7's temperatures gave an indication that there was slightly too much heat transfer from the heating tapes on the chamber wall.

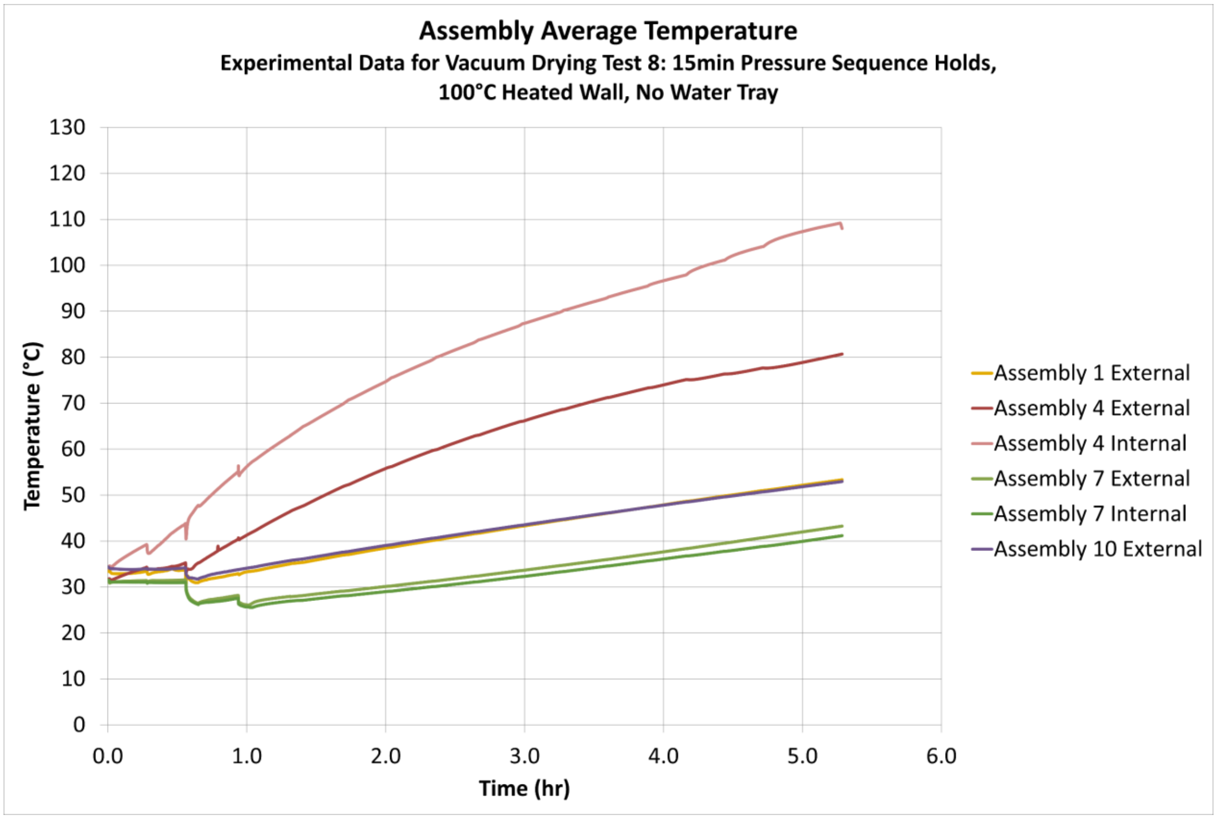

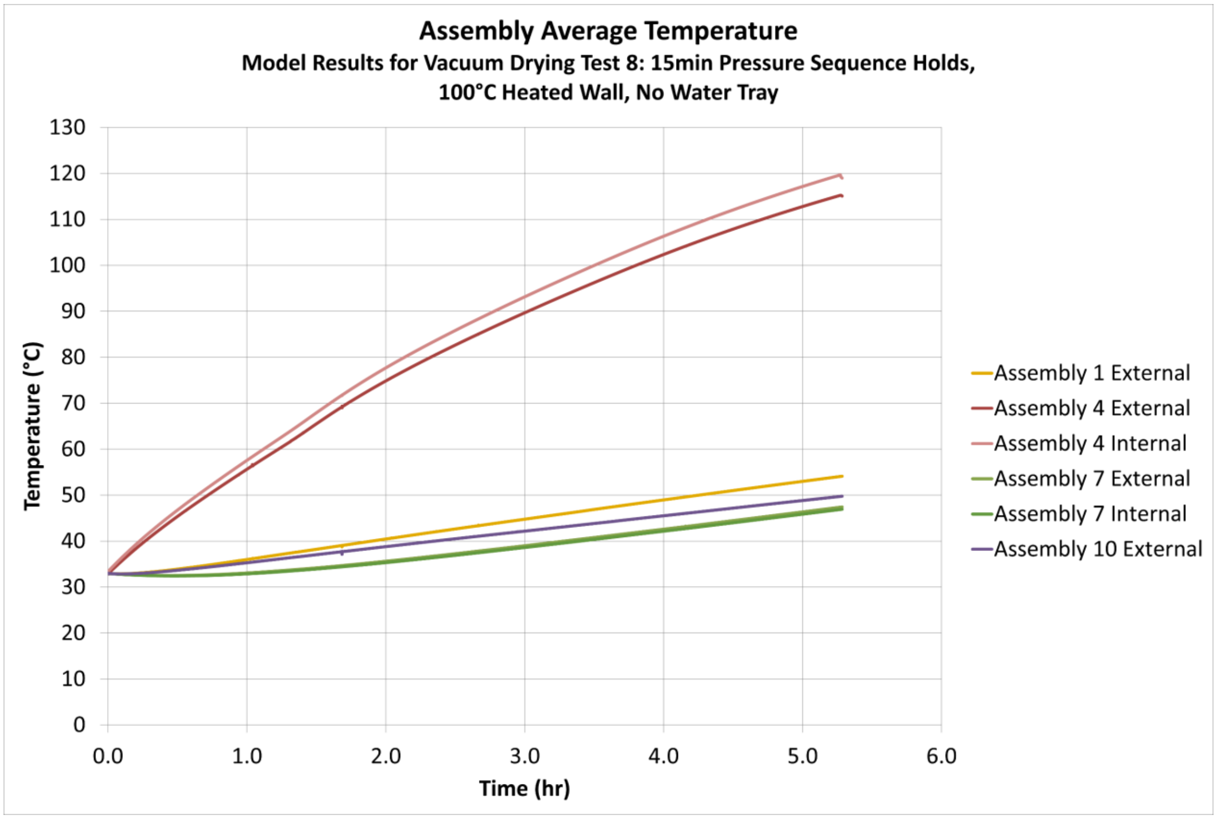

Figure 67. Vacuum-Drying Test 8 average temperatures of select assemblies for their external or internal plate from experimental data (top) and from outputted results of the model (bottom).

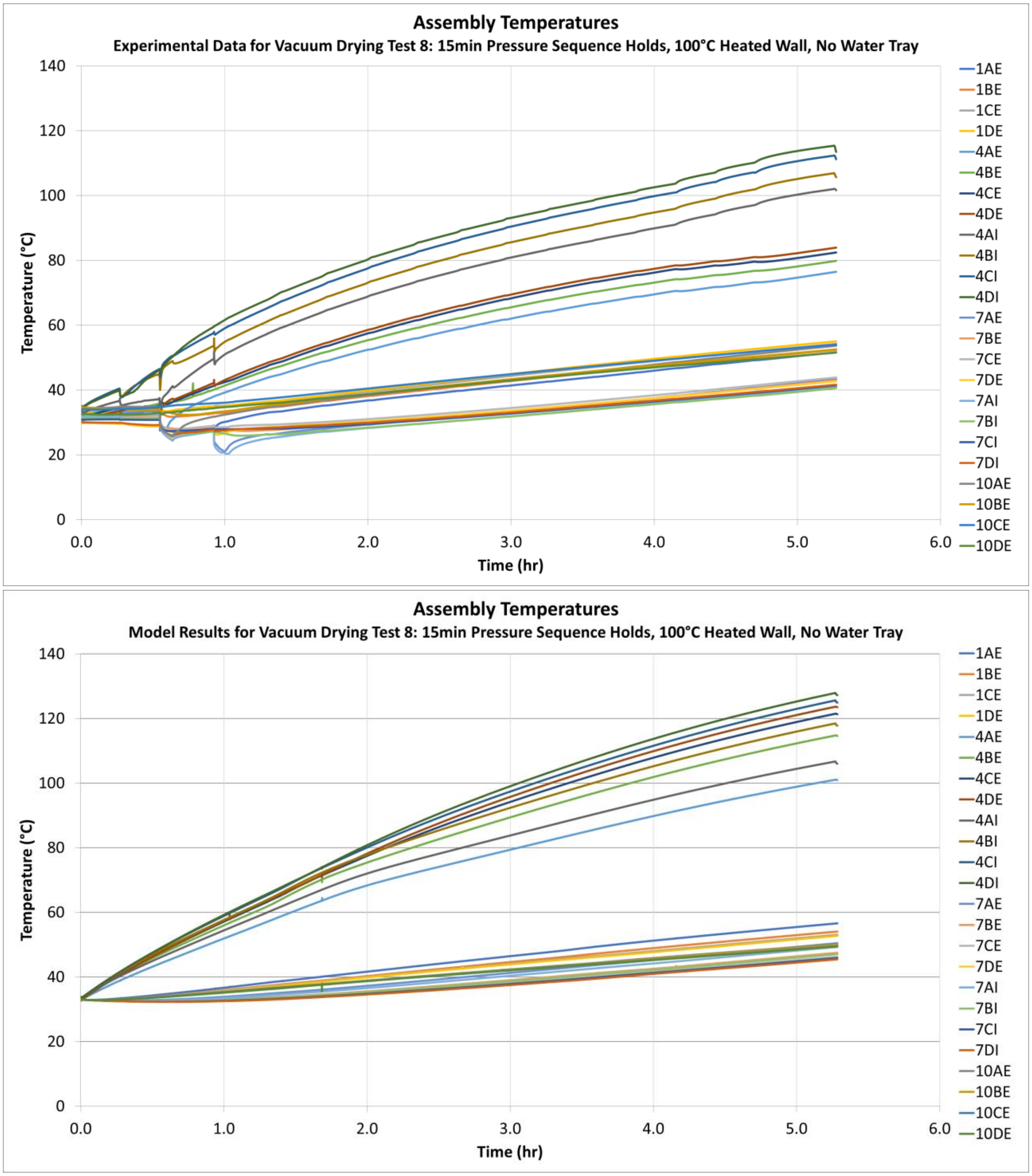

Figure 68. Vacuum-Drying Test 8 temperature readings at each thermocouple location from experimental data (top) and from outputted results of the model (bottom).

Table 15. Comparison of maximum temperature achieved at each assembly thermocouple location for the experimental drying test and outputted results from the model; Vacuum-Drying Test 8.

Assembly Thermocouple Location	Data Max Temperature (°C)	Model Max Temperature (°C)	Percent Error (%)	Avg. Percent Error (%)
1a External (°C)	51.678	56.592	9.51%	4.72%
1b External (°C)	52.458	54.042	3.02%	
1c External (°C)	54.258	53.073	2.18%	
1d External (°C)	55.031	52.732	4.18%	
4a External (°C)	76.486	101.051	32.12%	42.62%
4b External (°C)	79.864	114.764	43.70%	
4c External (°C)	82.454	121.486	47.34%	
4d External (°C)	83.934	123.653	47.32%	
4a Internal (°C)	102.045	106.687	4.55%	9.50%
4b Internal (°C)	106.916	118.468	10.81%	
4c Internal (°C)	112.347	125.598	11.79%	
4d Internal (°C)	115.379	127.905	10.86%	
7a External (°C)	43.386	50.457	16.30%	9.65%
7b External (°C)	43.026	47.470	10.33%	
7c External (°C)	43.877	46.278	5.47%	
7d External (°C)	42.712	45.494	6.51%	
7a Internal (°C)	40.965	49.287	20.31%	13.99%
7b Internal (°C)	40.628	47.074	15.87%	
7c Internal (°C)	41.455	45.869	10.65%	
7d Internal (°C)	41.651	45.461	9.15%	
10a External (°C)	53.672	50.168	6.53%	6.03%
10b External (°C)	52.578	49.899	5.09%	
10c External (°C)	54.030	49.519	8.35%	
10d External (°C)	51.582	49.433	4.17%	

8.2.2.2 Vacuum-Drying Residual Moisture Results

The residual moisture results from the model were again compared to the chamber relative humidity data collected during the drying test. However, since little to no chemisorbed water would be removed during vacuum drying, only the total bulk water content for all assemblies was plotted in Figure 69 against the experimental relative humidity. Simulation results showed that all bulk water was removed just after the 4-hour mark. The 4.25-hour mark was also when the canister was evacuated to the 5-Torr pressure hold at which relatively small rebounds were seen in the relative humidity for the remainder of the experimental drying tests. The low relative humidity rebounds give an indication that little to no moisture was present in the experimental vacuum tests following the evacuation to 5 Torr. Figure 70 further illustrates that the model predicted that Assembly 7 was the last assembly to be dried of bulk water and that this occurred when evacuating to the 5-Torr hold. This was in line with the initial thought that, given Assembly 7's location from the chamber wall (heat source), it would be the last assembly to be dried. Also, the model's chemisorbed water plots comply with TGA results where little to no chemically bound water was removed during vacuum drying. Note that the assemblies in the bottom graph of

Figure 70 begin with different amounts of chemisorbed water, representing the different number of corroded plates added to each assembly. As previously shown in Table 3, the experimental vacuum drying test 8 had three corroded plates in assembly 1, two corroded plates in assembly 4, and one corroded plate in assembly 7 and 10.

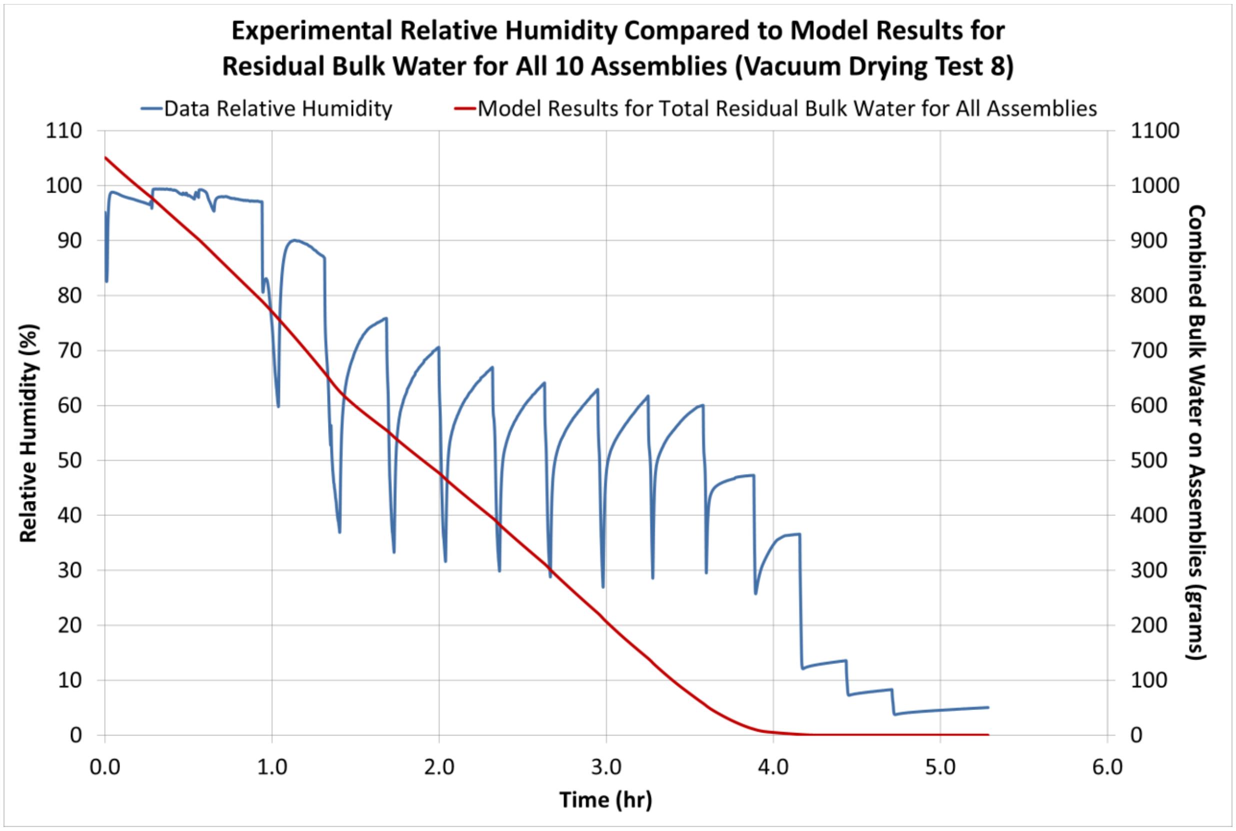

Figure 69. Comparison between Vacuum-Drying Test 8 experimental relative humidity measured inside the vessel and the model’s reading of the total bulk residual water for all 10 assemblies.

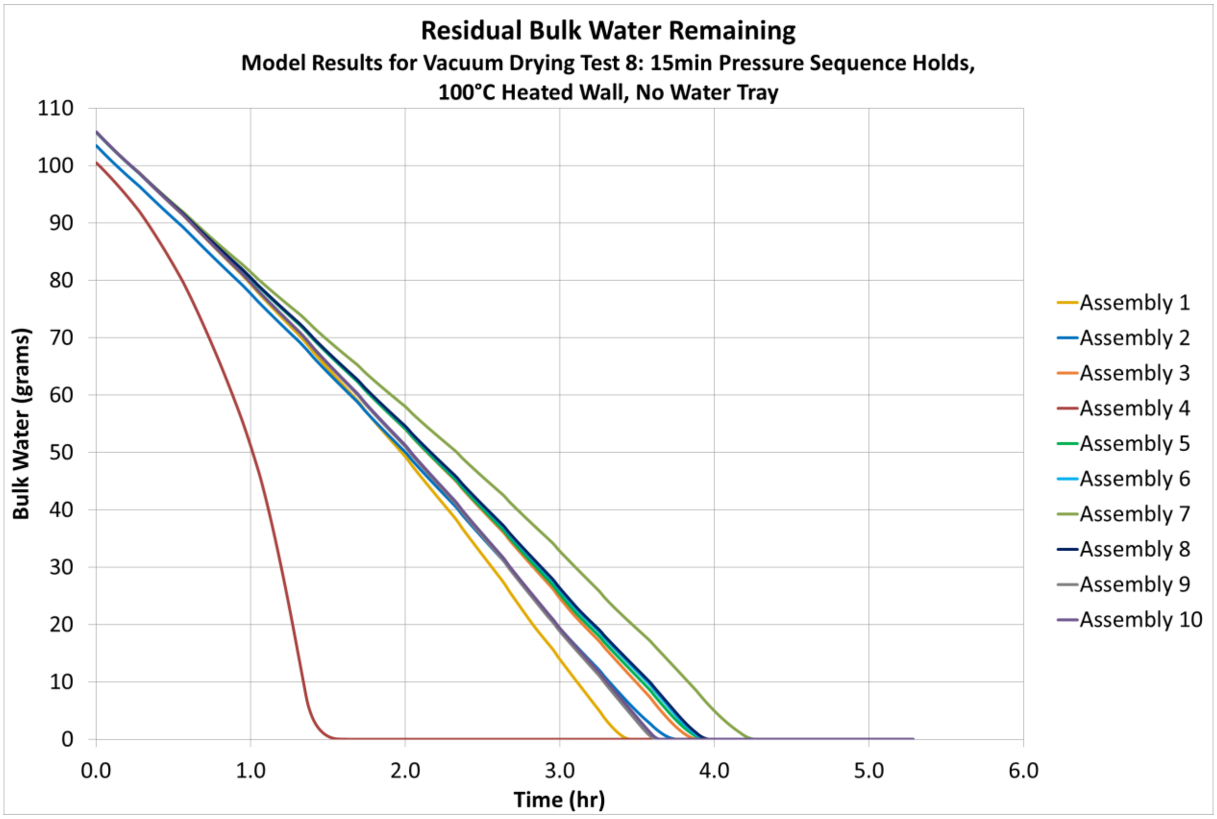

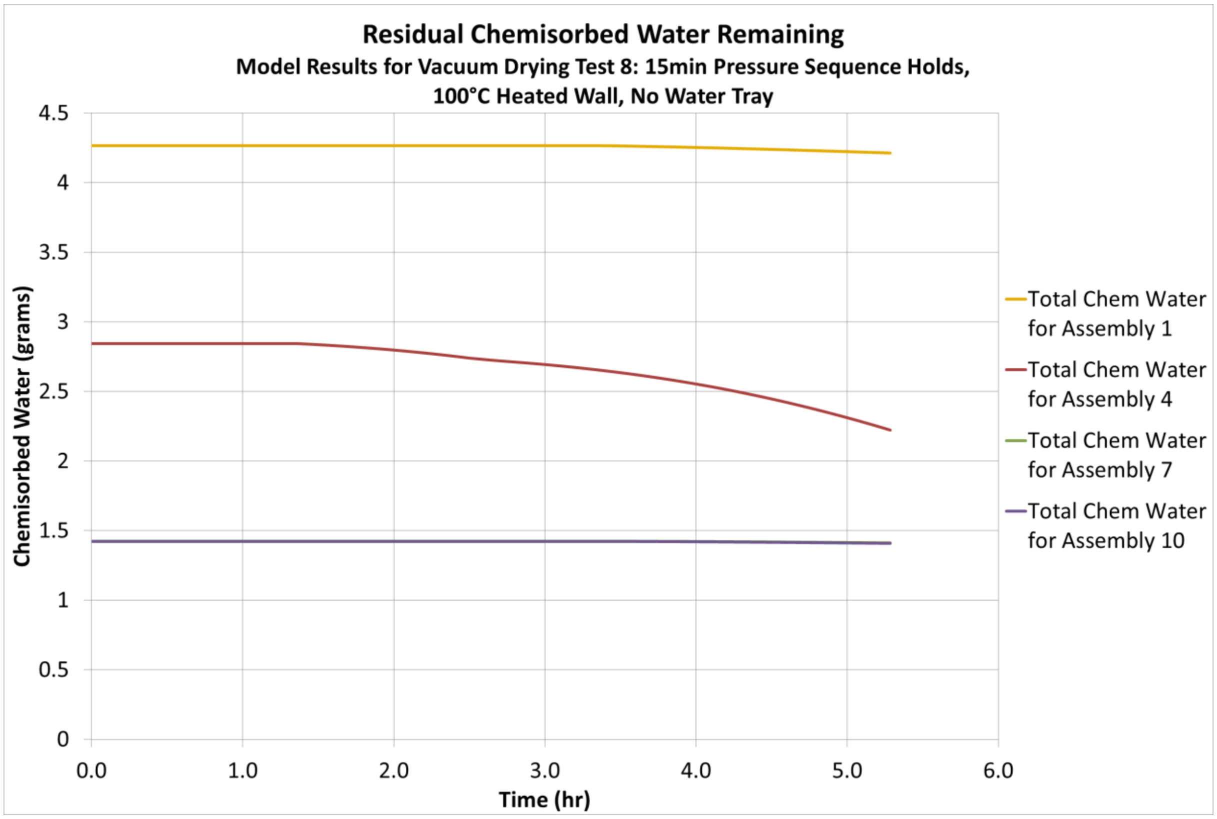

Figure 70. Vacuum-Drying Test 8 model results for residual bulk added to each assembly (top) and total residual chemisorbed water that was present in Assembly 1, 4, 7, and 10 (bottom).

9. FUTURE WORK

A total of seven recommendations for future work are given below, three suggestions for additional experimental testing and four avenues for improvement to drying process modeling. The vessel, basket, simulated ASNF assemblies, and experiment peripherals have been transferred from the Holtec facility in Camden, New Jersey to one of the labs at UofSC, in Columbia, South Carolina. Also, as shown in Table 1, INL has 51 corroded surrogate test plates still immersed in water and available for use to support additional testing: 30 Batch 5–Part 2 plates and 21 Batch 6 plates. So, equipment and surrogate material are available for an interim, pending decisions regarding additional testing.

First, as mentioned in Section 3, the siphon tube had to be positioned on the vent-port side of the drying chamber, atypical for commercial fuel drying. However, acceptable drying rates for a Type 1a basket were still achieved, as drying tests (the results in Section 6.1 and Section 6.2) showed that a majority of the bulk water was removed 3 hours into FHD and 4 hours into vacuum drying. Therefore, repeating all three drying processes (FHD, vacuum drying, and IFSF vacuum drying) with the siphon tube oriented correctly inside the drying chamber should further enhance the thermal and moisture removal performance. Such an effort would take a minimum of 6 months. The reorientation would require a shorter custom hose to connect the siphon tube to the siphon port.

Second, Section 6.2 highlights the difficulty of completely drying the 0.822 inches of bulk water (simulating three ASNF canisters) using the IFSF drying procedures. If there is interest in drying three ASNF baskets at the same time with this approach, additional IFSF vacuum-drying tests would be beneficial. Limited knowledge regarding the IFSF drying process hampered testing, and at least 3 months of additional work would allow for process optimization and validation of improved performance. Changes in wall temperature (IFSF insert temperature) or drying criteria could greatly impact whether complete water removal can be achieved.

Third, operating FHD tests with a chiller to remove water vapor from the recirculated helium (Phase 2 drying) would provide a better measure of FHD performance capacity. This effort would take a minimum of 5 months. The FHD process for commercial fuel consists of two discrete phases where the first phase vaporizes all bulk water inside the canister and the second phase removes the water vapor (via chiller) until a target vapor pressure of 3 torr or lower is achieved. The FHD tests in the current work consisted of only the first phase of drying because sustaining a target assembly plate temperature for a predetermined amount of time was the desired test criterion. Conducting FHD tests with the two-phase operation may show a similar effectiveness (in removal of both bulk and chemisorbed water) in less time than the 6–12 hours shown in the current work.

Fourth, the development of a more accurate representation for the heat applied to chamber wall via heating tapes is advisable (nominally a one-month effort). Although Section 8.2 highlights that both models came to within a 15% percent error of the experimental data for almost all assembly thermocouples, the model was unable to successfully demonstrate the top of the assemblies becoming the hottest location as well as Assembly 7 being the coldest assembly due to its proximity to the chamber wall. Correcting the heat distribution applied to the wall will ultimately improve the drying results as it will improve the accuracy of the heat transferred inside the chamber. The current model uses constant fluid properties. In future vacuum modeling work, replacing this constant fluid property assumption with temperature and pressure dependent functions can be assessed for the effect on the resulting temperature profiles. The outer most steel canister wall and insulation layers could also be meshed and included in the model to alleviate the heat transfer through this boundary, such that the only included heat transfer coefficient is the h_{amb} term from insulation to the exterior air via natural convection.

Fifth, the simulated spacer disc and bulk water trays should be integrated into the 3D-CAD and STAR-CCM (approximately two months of work). In addition to allowing validation of the remaining drying tests in the current work, integrating the simulated spacer disc and bulk water trays into the model will provide insight as to why the IFSF drying procedure was unsuccessful in drying the 0.822 inches of bulk water.

Sixth, each assembly's orientation in the 3D-CAD should be modified to accurately represent their asymmetrical loading observed during the experimental tests (about a one-month effort). Higher Assembly 4 external plate temperatures (nichrome wire assembly), observed by the model in Section 8.2, may have contributed to the assembly absorbing all the nichrome wire heat load. Angling Assembly 4 against the basket slot wall, which happens during the experimental tests, should allow the applied heat from the nichrome wire to displace along the wall, reducing Assembly 4's overall external plate temperature. This alteration is anticipated to significantly impact Assembly 4's heat-up rate and, as a result, effect Assembly 4's drying time in the model. Another addition to the specific assembly work could be to model the heat loss due to vaporization. While it was shown the heat loss in negligible in FHD cases, for vacuum cases, the 10.5% attributed to this could also be a potential heat source that may contribute to overestimates for temperatures.

Lastly, validation is advised for the remaining FHD and vacuum-drying tests conducted in the current work (at least a three-month effort). Validating the models against more drying tests will improve confidence and better accommodate adaptation of the drying models to other commercial or research reactor fuel types.

10. CONCLUSIONS

The TGA results for the FHD drying test directly correlate with the SEM results of the FHD drying tests. TGA results indicated that a phase change was occurring around 220°C, and the SEM results found a visual indication of the phase change that occurred. This phase change is an indication of the extent to which the chemically adsorbed water has been removed from the samples at or above 220°C. FHD provides drying capabilities beyond the ability to remove bulk water and physisorbed moisture, specifically including decomposition of some chemisorbed water. Vacuum drying is capable of removing the bulk water but was ineffective at removal of chemisorbed water in this test series, because the necessary temperatures were not achieved.

11. REFERENCES

[1] Snow, S. D. 2008. “Design Considerations for the Standardized DOE SNF Canister Internals, National Spent Nuclear Fuel Program.” DOE/SNF/DSN-019, Rev.1, Department of Energy.

[2] Smith, R. E. 2019 “Aluminum Clad Spent Nuclear Fuel Task 5: Oxide Layer Response to Drying Experiment Test Plan.” INL/EXT-19-54019, Rev. 1, Idaho National Laboratory. https://doi.org/10.2172/1558451.

[3] Abboud, Alexander, and Hai Huang. 2018. “Transient Coupled Chemical-Thermal-Fluid Field Simulation for Sealed Aluminum-Clad Spent Nuclear Fuel Storage Canister.” INL/EXT-18-51683, Rev. 0, Idaho National Laboratory.

[4] Abboud, Alexander, and Hai Huang. 2018. “Development of Transient Coupled Chemical-Thermal-Fluid Multiphysics Simulation for Unsealed, Vented Aluminum-Clad Spent Nuclear Fuel Storage Canister.” INL/EXT-18-51681, Rev. 0, Idaho National Laboratory.

[5] Connolly, M. J. 2017. “Aluminum Clad Spent Nuclear Fuel Long Term Dry Storage Technical Issues Action Plan – Technical and Engineering Activities.” INL/EXT-17-43908, Idaho National Laboratory. https://doi.org/10.2172/1466830.

[6] DOE SNFWG. 2017. “Aluminum-Clad Spent Nuclear Fuel: Technical Consideration and Challenges for Extended (>50 Years) Dry Storage.” DOE/ID RPT-1575, Department of Energy Spent Nuclear Fuel Working Group, Aluminum-Clad SNF Sub-Working Group.

[7] U.S. NWTRB. 2017. “Management and Disposal of U.S. Department of Energy Spent Nuclear Fuel.” A report to the United States Congress and the Secretary of Energy, United States Nuclear Waste Technical Review Board (J. M. Bahr, chair).

[8] Lister, T., and C. Orme. 2020. “Vapor Phase Corrosion of Pretreated Aluminum Alloys: Final Report.” INL/EXT-19-56497, Rev. 1, Idaho National Laboratory.

[9] Glazoff, M. V., and T. E. Lister. 2020. “Transition of Spent Nuclear Fuel to Dry Storage: Modeling Activities Concerning Aluminum Spent Nuclear Fuel Cladding Integrity.” INL/EXT-18-51694, Rev. 1, Idaho National Laboratory. https://doi.org/10.2172/1492831.

[10] Metzger, K. E., R. E. Fuentes, A. L. d'Entremont, L. C. Olson, and R. L. Sindelar. 2018. “Preparation of Aluminum Oxide Films Under Water Exposure – Preliminary Report on 1100 Series Alloys.” SRNL-STI-2018-00427, Savannah River National Laboratory. https://doi.org/10.2172/1471999.

[11] d’Entremont, A. L., R. E. Fuentes, L. C. Olson, and R. L. Sindelar. 2018. “Preparation of Aluminum Oxide Films Under Water Exposure – Preliminary Report on 6061 Series Alloys.” SRNL-STI-2018-00449, Savannah River National Laboratory. https://doi.org/10.2172/1472000.

[12] d’Entremont, A. L., R. E. Fuentes, L. C. Olson, and R. L. Sindelar. 2018. “Preparation of Aluminum Oxide Films Under Water Exposure – Preliminary Report on 5052 Series Alloys.” SRNL-STI-2018-00646, Savannah River National Laboratory. https://doi.org/10.2172/1485265.

[13] Fuentes, R. E., A. L. d'Entremont, C. G. Verst, C. Crawford, B. L. Garcia-Diaz, and R. L. Sindelar. 2019. “Oxyhydroxides on Aluminum Spent Nuclear Fuel: Formation Studies and Removal Practices to Prevent Radiolytic Gas Production.” SRNL-STI-2019-00594, LDRD-2018-00032, LDRD External Report Summary, Savannah National Laboratory. https://doi.org/10.2172/1568793.

[14] Winston, P. 2018. “Aluminum Spent Fuel Performance in Dry Storage: Initial Characterization of ATR End Box Samples,” INL/EXT-18-51230, Idaho National Laboratory.

[15] Winston, P. 2018. “Aluminum Spent Fuel Performance in Dry Storage: Aluminum Oxide Sampling of ATR Dry-Stored Fuel,” INL/EXT-20-58404, Idaho National Laboratory. https://doi.org/10.2172/1642905.

[16] Olson, L., R. Fuentes, A. d'Entremont, and R. Sindelar. 2018. “Characterization of Oxyhydroxides on a Dry-Stored Fuel Plate from L-Basin.” SRNL-STI-2018-00428, Savannah River National Laboratory. https://doi.org/10.2172/1480833.

[17] Olson, L., C. Verst, A. L. d'Entremont, R. E. Fuentes, and R. L. Sindelar. 2019. “Characterization of Oxide Films on Aluminum Materials Following Reactor Exposure and Wet Storage in the SRS L-Basin.” SRNL-STI-2019-00058, Savannah River National Laboratory. https://doi.org/10.2172/1501352.

[18] Parker-Quaife, E. H., and G. P. Horne. 2020. “Milestone 2.8: Preliminary Radiolytic Gas Generation Measurements from Helium-Backfilled Samples.” INL/EXT-21-61404, Idaho National Laboratory. https://doi.org/10.2172/1768757.

[19] Verst, C., et al., to J. Jarrell and R.Sindelar. 2020. “Instrumented Lid – Initiation Irradiation and Measurement of As-is Hydrated Oxide Specimens (Large Coupons).” SRNL-L6000-2020-00038, Savannah River National Laboratory.

[20] Verst, C., et al., to J. Jarrell and R.Sindelar. 2020. “Instrumented Lid – Initiation Irradiation and Measurement of Dried Hydrated Oxide Specimens (Large Coupons).” SRNL-L6000-2020-00046, Savannah River National Laboratory.

[21] Verst, C., et al., to J. Jarrell and R.Sindelar. 2021. “Interim Irradiation and Measurement of As-Dried vs As-Corroded Hydrated Oxide Specimens (Large Coupons).” SRNL-L6000-2021060038, Savannah River National Laboratory.

[22] McNamara, J. D., et. al., to J. Jarrell and R.Sindelar. 2019. “Instrumented Lid – Fabrication of Basket.” SRNL-L2240-2019-00006, Savannah River National Laboratory.

[23] Sindelar, R. L., and D. T. Herman. 2020. “Technology Development for Aluminum-clad Spent Nuclear Fuel for Extended Dry Storage – Status Report.” SRNL-STI-2020-00172, Savannah River National Laboratory. https://doi.org/10.2172/1701703.

[24] Perry, Robert H., and Don Green, Eds. 1984. Perry’s Chemical Engineers’ Handbook, 6th Edition, McGraw-Hill, Inc.

[25] Knight, T., N. Cooper, M. Shalloo, T. Farouk, Y. Wang, J. Khan, and R. E. Smith. 2019. “Aluminum-clad Spent Nuclear Fuel Engineering Scale Drying Experiment Design.” INL/EXT-19-56017, Rev. 0, Idaho National Laboratory. https://doi.org/10.2172/1572393.

[26] Smith, R. E. 2020. “ASNF Engineering Scale Drying Experiment Acceptance Criteria for Fabricated Items.” INL/MIS-20-58551, Rev. 1, Idaho National Laboratory.

[27] Smith, R. E., et al. 2020. “ASNF Engineering Scale Drying Experiment System Operability Functional Requirements.” INL/MIS-20-58841, Rev. 1, Idaho National Laboratory.

[28] Christensen, A. B. 2017. “Intact ATR Plate Fuel Drying Characteristics and Requirements.” EDF-5063, Rev. 3.

[29] d’Entremont, A. L., R. Fuentes, M. Shalloo, T. Knight, and R. Sindelar. 2020. “Thermal Dehydration of Aluminum (Oxy)hydroxides on Fuel Cladding Material.” 20200, Waste Management, WM2020 Conference, March 8–12, 2020, Phoenix, Arizona, USA.

[30] Patel, S. M, T. Doen, and M. J. Pikal. 2009. “Determination of End Point of Primary Drying in Freeze-Drying Process Control.” AAPS PharmSciTech 11(1): 73–84. https://doi.org/10.1208/s12249-009-9362-7.

[31] Cooper. N. 2020. “Development of a CFD Model for the Drying of Aluminum-Clad Spent Nuclear Fuel.” Master’s Thesis, University of South Carolina.

[32] Incropera, Frank P., David P. Dewitte, Theodore L. Bergman, Adriennes S. Lavine. 2003. Principles of Heat and Mass Transfer, 7th Edition. John Wiley & Sons.

[33] Versteeg, H. K., and W. Malalasekera. 2007. An Introduction to Computational Fluid Dynamics, 2nd Edition. Pearson.

[34] Persad, Aaran H., and Charles A. Ward. 2016. “Expressions for the Evaporation and Condensation Coefficients in the Hertz-Knudsen Relation.” Chem. Rev. 116(14): 7727–7767. https://doi.org/10.1021/acs.chemrev.5b00511.

[35] Ytrehus, T., and S. Ostmo. 1996. “Kinetic Theory Approach to Interphase Processes.” Int. J. Multiphase Flow, 22(1): 133–155. https://doi.org/10.1016/0301-9322(95)00056-9.

[36] Thomson, George W. M. 1946. “The Antoine Equation for Vapor-Pressure Data.” Chemical Review Vol. 38, 1–39. https://doi.org/10.1021/cr60119a001.

[37] 2018. “Water.” NIST Chemistry WebBook. National Institute of Standards and Technology, https://webbook.nist.gov/cgi/inchi/InChI%3D1S/H2O/h1H2.

[38] Perry, J. 2021. “Experimental Evaluation of Drying Spent Nuclear Fuel for Dry Cask Storage through Vacuum Drying and Forced Helium Dehydration.” Master’s Thesis, University of South Carolina, (unpublished).

[39] Lienhard, John H, IV and John H. Lienhard V. 2008. A Heat Transfer Textbook. Cambridge, Mass: Phlogiston Press. https://www.emetechnologies.com/Download/Mechanical/Heat%20Transfer.pdf.

[40] Shalloo, M. 2019. “Characterization and Drying of Oxyhydroxides on Aluminum Clad Spent Nuclear Fuel.” Master’s Thesis, University of South Carolina. 2019.

[41] Wefers, K., and Misra, C. 1997. “Oxides and Hydroxides of Aluminum.” Alcoa Laboratories. Technical Paper No. 19. http://epsc511.wustl.edu/Aluminum_Oxides_Alcoa1987.pdf.

[42] 2018. STAR-CCM+ 13.02 User Guide.

[43] 2017. “Boron Nitride Solids Product Data Sheet.” Saint-Gobain. https://www.bn.saint-gobain.com/sites/imdf.bn.com.

[44] Shih, T.-H., Liou, W.W., Shabbir, A., Yang, Z. and Zhu, J. 1994. “A New k-ε Eddy Viscosity Model for High Reynolds Number Turbulent Flows -- Model Development and Validation”, NASA TM 106721.

[45] Alwitt, Robert S. “The Growth of Hydrous Oxide Films on Aluminum.” Journal of The Electrochemical Society, vol. 121, no. 10, Oct. 1974, p. 1322. https://iopscience.iop.org/article/10.1149/1.2401679.

Page intentionally left blank

Appendix A
Equipment List

The model numbers of the PXI chassis, cards, and equipment are listed in Table 16 below.

Table 16. National Instrument data acquisition system equipment list for Test PXI.

Model	Description	Quantity
NI PXIe-8840 Quad-Core No Express Card	PXIe-8840 Quad Core, Windows 10 64-bit (Multi-Language)	1
RAM 8 GB	8 GB RAM for PXIe-8840, PXI-8840, and PXIe-8821	1
NI PXIe-6341	PXIe-6341, X Series DAQ (16 AI, 24 DIO, 2 AO)	1
SCB-68A	SCB-68A Noise Rejecting, Shielded I/O Connector Block	1
SHC68-68-EPM Cable (2m)	SHC68-68-EPM Shielded Cable, 68-D-Type to 68 VHDCI Offset, 2 m	1
NI PXIe-4302	NI PXIe-4302 +/-10V, 32-Ch, 24-bit, 5kS/s/ Voltage Input Module	1
TB-4302	TB-4302, Front mount terminal block for PXIe-4302/3	1
NI PXIe-4322	NI PXIe-4322 Isolated Analog Output Module	1
TB-4322	NI TB-4322 Terminal Block Accessory for PXIe-4322	1
NI PXIe-4353	PXIe-4353 32-Ch Thermocouple Input	2
TB-4353	NI TB-4353 Isothermal Terminal Block for PXIe-4353	2
NI PXIe-1082	PXIe-1082, 8-Slot 3U PXI Express Chassis	1

Page intentionally left blank

Appendix B
Drying Test Schematics

The final version of the drying schematics for FHD tests, normal vacuum-drying tests, and IFSF drying tests are shown in Figure 71, Figure 72, and Figure 73, respectively, below.

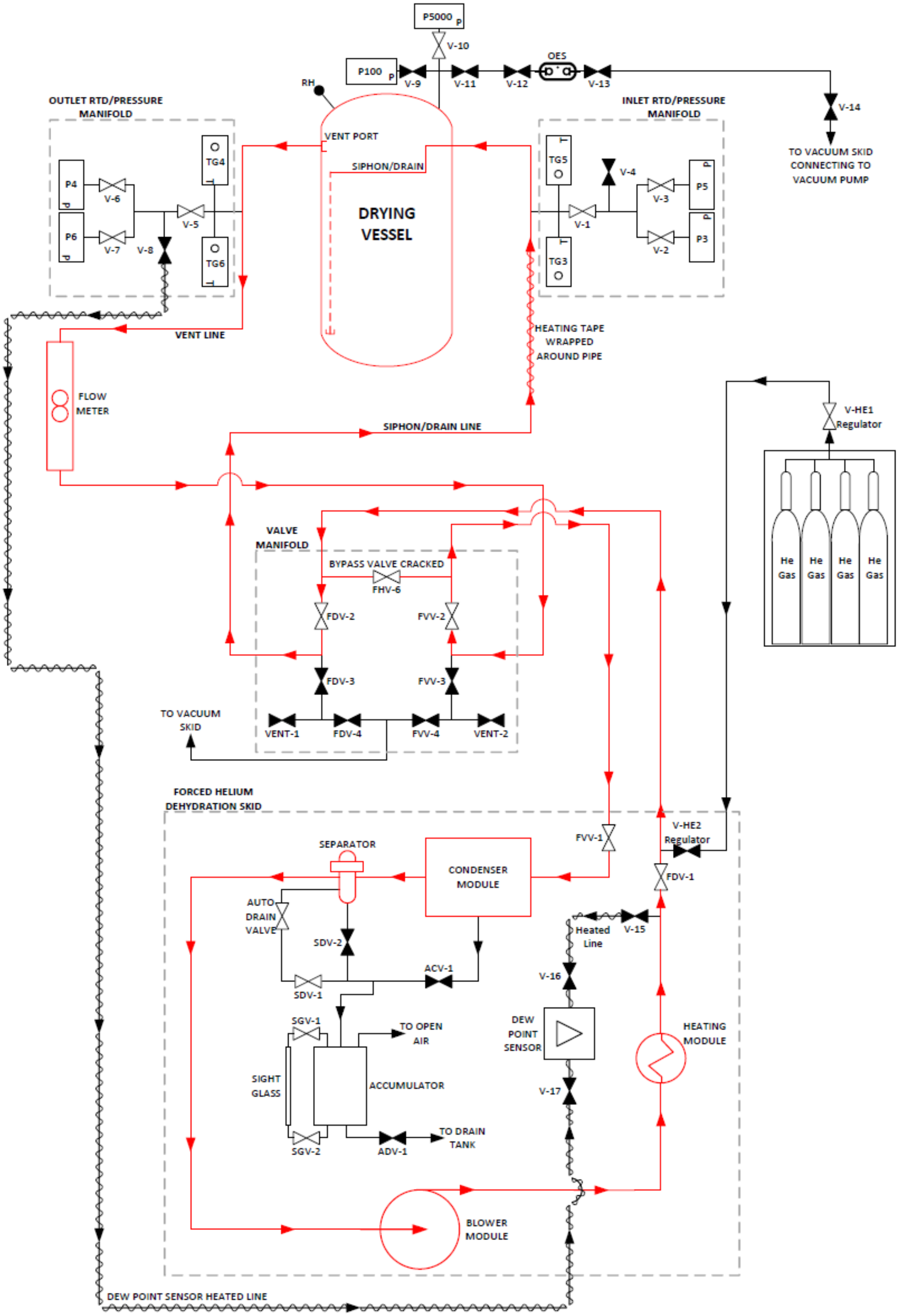

Figure 71. Drying schematic for FHD tests.

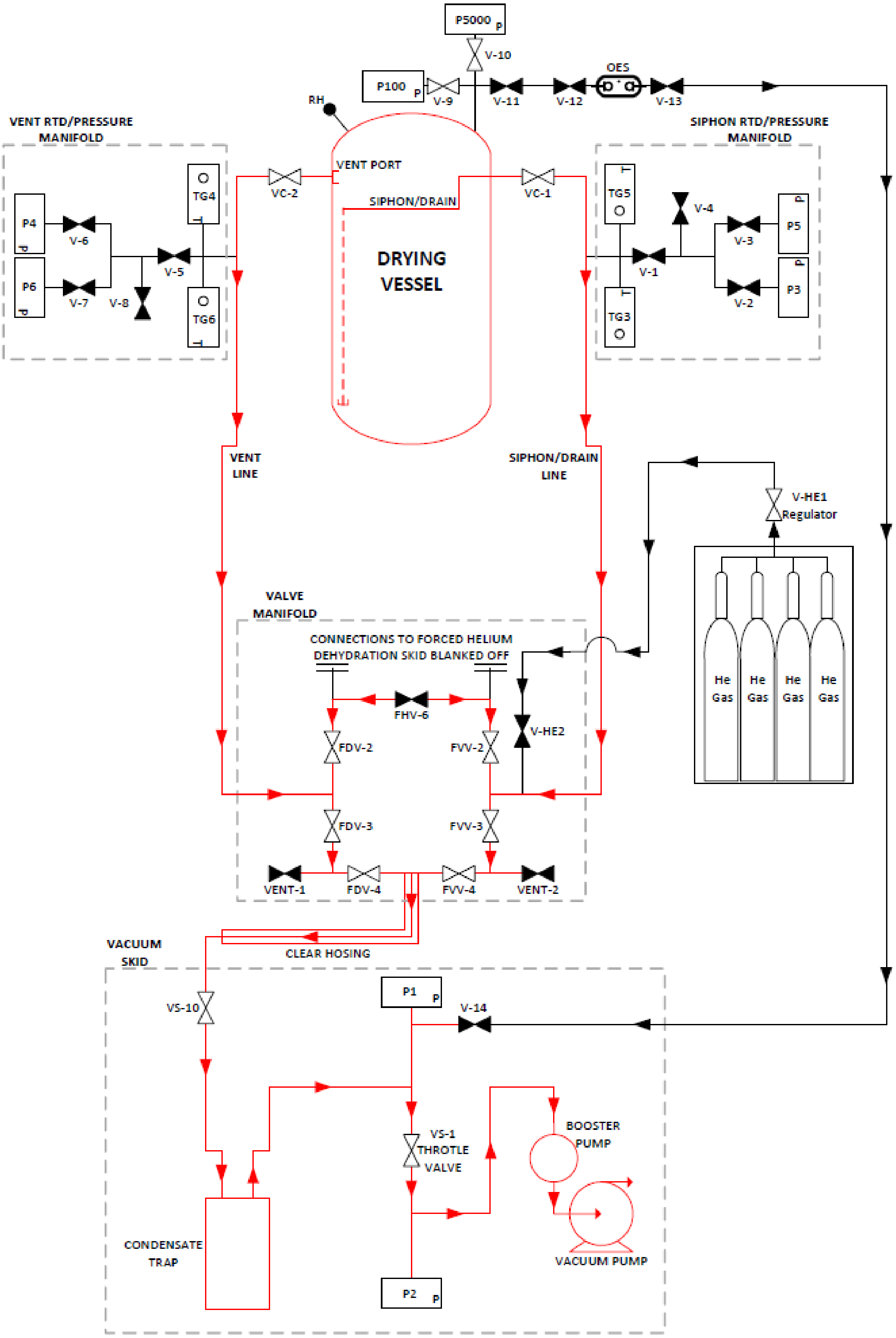

Figure 72. Drying schematic for normal vacuum-drying tests.

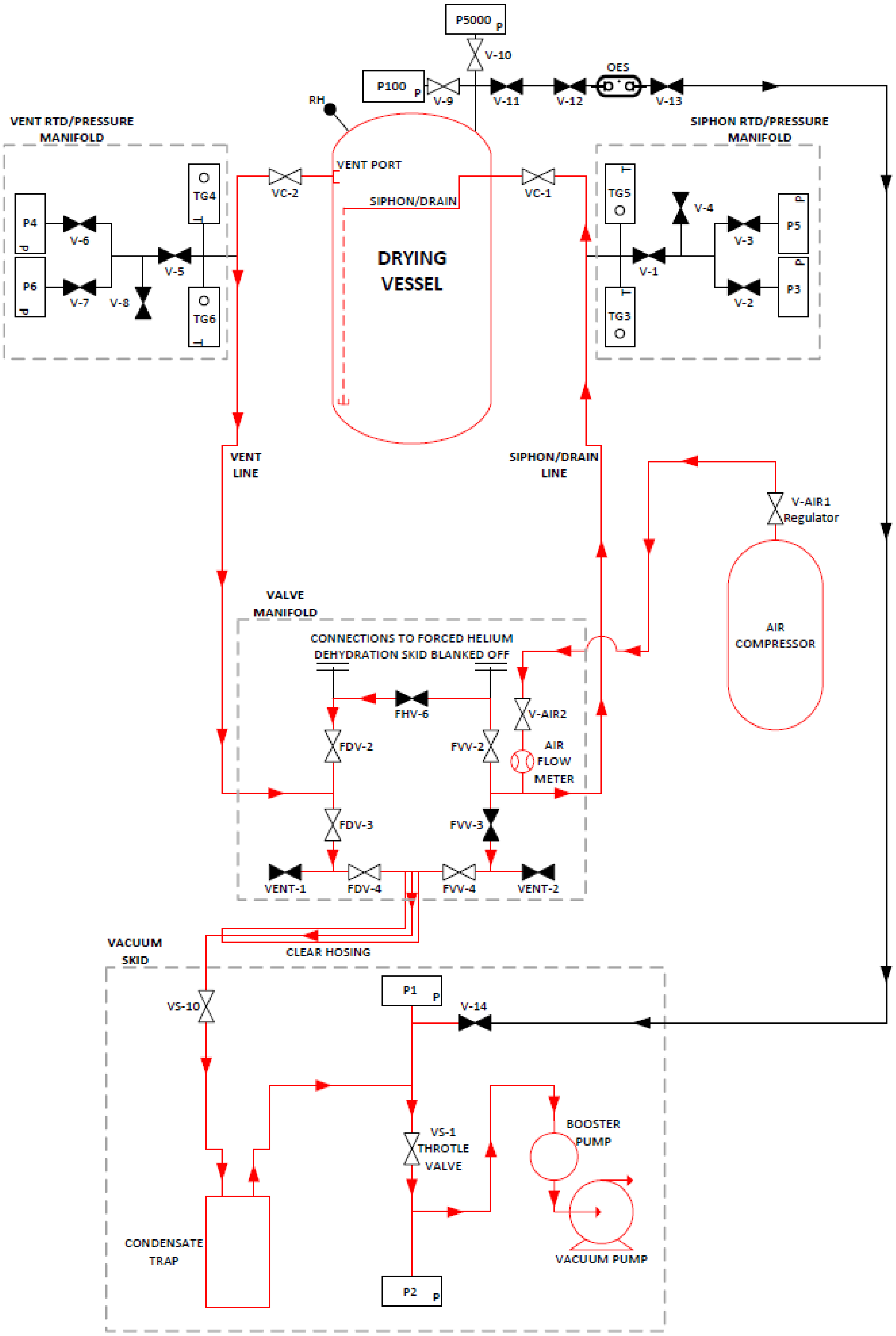

Figure 73. Drying schematic for IFSF vacuum-drying tests.

Page intentionally left blank

Appendix C
Select Material Properties

The physical properties of solids employed and modeled for the engineering-scale drying experiment are given in Table 17.[32,42,43]

Table 17. Select properties of solids at 25°C.

Aluminum	
Density	2.70 g/cm^3
Thermal Conductivity	237.0 W/m-K
Boron Nitride	
Density	1.90 g/cm^3
Thermal Conductivity	78 W/m-K
Steel	
Density	8.01 g/cm^3
Thermal Conductivity	15.1 W/m-K
Fiberglass Insulation	
Thermal Conductivity	0.038 W/m-K

The physical properties of gases employed and modeled for the engineering-scale drying experiment are given in Table 18.[42]

Table 18. Selected properties of gases at 25°C.

Air	
Molar Mass	28.97 g/mol
Density	$1.18\text{x}10^{-3}$ g/cm^3
Dynamic Viscosity	$1.86\text{x}10^{-5}$ Pa-s
Thermal Conductivity	0.026 W/m-K
Helium	
Molar Mass	4.00 g/mol
Density	$1.64\text{x}10^{-4}$ g/cm^3
Dynamic Viscosity	$1.99\text{x}10^{-5}$ Pa-s
Thermal Conductivity	0.155 W/m-K
Water Vapor	
Molar Mass	18.02 g/mol
Density	$5.95\text{x}10^{-4}$ g/cm^3
Dynamic Viscosity	$1.27\text{x}10^{-5}$ Pa-s
Thermal Conductivity	0.025 W/m-K